8-8-2023

Exploring bistatic scattering modeling for land surface applications using radio spectrum recycling in the Signal of Opportunity Coherent Bistatic Simulator

Dylan R. Boyd
Mississippi State University, db1950@msstate.edu

Exploring bistatic scattering modeling for land surface applications using radio spectrum recycling in the Signal of Opportunity Coherent Bistatic Simulator

By

Dylan R. Boyd

Approved by:

Mehmet Kurum (Major Professor)
John E. Ball
J. Patrick Donohoe
Ali Cafer Gurbuz
Qian (Jenny) Du (Graduate Coordinator)
Jason M. Keith (Dean, Bagley College of Engineering)

A Dissertation
Submitted to the Faculty of
Mississippi State University
in Partial Fulfillment of the Requirements
for the Degree of Doctor of Philosophy
in Electrical and Computer Engineering
in the Department of Electrical and Computer Engineering

Mississippi State, Mississippi

August 2023

Name: Dylan R. Boyd

Date of Degree: August 8, 2023

Institution: Mississippi State University

Major Field: Electrical and Computer Engineering

Major Professor: Mehmet Kurum

Title of Study: Exploring bistatic scattering modeling for land surface applications using radio spectrum recycling in the Signal of Opportunity Coherent Bistatic Simulator

Pages of Study: 184

Candidate for Degree of Doctor of Philosophy

The potential for high spatio-temporal resolution microwave measurements has urged the adoption of the signals of opportunity (SoOp) passive radar technique for use in remote sensing. Recent trends in particular target highly complex remote sensing problems such as root-zone soil moisture and snow water equivalent. This dissertation explores the continued open-sourcing of the SoOp coherent bistatic scattering model (SCoBi) and its use in soil moisture sensing applications. Starting from ground-based applications, the feasibility of root-zone soil moisture remote sensing is assessed using available SoOp resources below L-band. A modularized, spaceborne model is then developed to simulate land-surface scattering and delay-Doppler maps over the available spectrum of SoOp resources. The simulation tools are intended to provide insights for future spaceborne modeling pursuits.

Key words: bistatic scattering, SNOOPI, TDS-1, HydroGNSS, CYGNSS, GNSS-Reflectometry, multilayer, topography, SCoBi, Signals of Opportunity, soil moisture, end-to-end, geospatial, land information, Kirchhoff approximation, physical optics, geometrical optics, surface scattering, scattering coefficient

DEDICATION

To Jiji.

ACKNOWLEDGEMENTS

This work was supported in part by the National Aeronautics and Space Administration (NASA) Future Investigators in NASA Earth and Space Science and Technology (FINESST) grant 80NSSC21K1586 as well as partial funding from the United States Department of Defense by means of the SimBRS II TO-002 project.

I am thankful to every person that has pushed or enabled me to explore this exciting world of research.

I thank Dr. Kurum in equal parts for his friendship and mentorship. I cannot imagine a more supportive soul.

I thank Dr. Ali Gurbuz as a professor, advisor, and for our many discussions exploring machine learning through this subject.

I am grateful to Dr. Batuhan Osmanoglu, Dr. Quenton Bonds, and Dr. Rafael Rincon for the opportunity to learn with them and their invaluable mentorship during my internships at NASA Goddard Space Flight Center.

I am thankful to all of my committee members, and I am especially grateful for Dr. Donohoe's assistance in providing guidance and computing resources. I am thankful to Dr. Ball whose unwavering dedication to his students during his tenure process will always inspire me.

I thank the many friends I have made during this program. I thank Orhan Eroglu for his mentorship and both Md. Mehedi Farhad and Benjamin Nold for their unwavering friendship.

I am indebted to Lily for believing in me.

I am humbled and privileged to receive love and support from my family: Angie, Scotty, and Madison.

TABLE OF CONTENTS

LIST OF TABLES

LIST OF FIGURES

ACRONYMS

AirMOSS Airborne Microwave Observatory of Subcanopy and Subsurface

BRCS Bistatic radar cross-section

CRLB Cramer-Rao lower bound

CRS Coordinate reference system

CYGNSS Cyclone Global Navigation Satellite System

DDM Delay-Doppler map

DEM Digital Elevation Map

DI-KA Direct numerical integration of the KA

DSS Decision support system

ECEF Earth-centered, earth-fixed

EGM96 Earth Gravitational Model 1996

ENU East-North-Up

FM Facet method

FM-KA Facet-method-based KA

GNSS Global navigation satellite system

GNSS-R GNSS reflectometry

GO Geometrical optics

GPS Global Positioning System

HDF5 Hierarchical Data Format version 5

IEM Integral equation method

IGOT Improved GO with topography

IMPRESS Information Processing and Sensing

JRC GWB European Commission Joint Research Centre Global Waterbody

KA Kirchhoff approximation

LVLH Local-vertical, local-horizontal

M&S Modeling and simulation

MLE Maximum likelihood estimator

MRS Microwave remote sensing

MSU Mississippi State University

MUOS Mobile User Objective System

NASA National Aeronautics and Space Administration

NBRCS Normalized bistatic radar cross-section

NFM Nested facet method

NMM3D Three-dimensional Numerical Maxwell Model

NSF National Science Foundation

PDF Probability distribution function

PO Physical optics

RF Radio frequency

RMS Root-mean square

RMSE Root-mean square error

RZSM Root-zone soil moisture

SAR Synthetic aperture radar

SCoBi SoOp coherent bistatic scattering model

SDR Software-defined radio

SM Soil moisture

SMAP Soil Moisture Active/Passive

SMOS Soil Moisture and Ocean Salinity

SNOOPI SoOp P-band Investigation

SoOp Signals of opportunity

SoOp-R SoOp Reflectometry

SP Specular point

SPM Small perturbation method

SWaP Size, weight, and power

SWE Snow water equivalent

TDS-1 Technology Demonstration Satellite-1

UAS Unmanned aerial system

UHF Ultra high frequency

VHF Very high frequency

VSM Volumetric soil moisture

WGS84 World Geological Survey 1984

ZV-GO Zavorotny-Voronvich GO model

CHAPTER I

INTRODUCTION

1.1 Abstract

An overview of microwave remote sensing (MRS) for global land-scattering applications is provided. Currently, L-band signals (between 1 and 2 GHz) are the lowest frequencies available for active and passive remote sensing. Longer wavelengths are expected to benefit current remotely sensed data products such as soil moisture (SM) while also creating the first directly-sensed retrievals for data products such as root-zone soil moisture (RZSM). While active systems are restricted from operating over many nations, signals of opportunity (SoOp) can enable new remote sensing datasets at a global scale. This method presents unique modeling challenges due to the use of non-cooperative, bistatic radar measurements. An overview of the benefits and challenges for SoOp remote sensing is presented in light of creating modeling tools which can operate for ground, air, and spaceborne-scale simulations of dynamic land surface properties and topography.

1.2 Motivation

The remote sensing community is constantly changing with respect to its capabilities, goals, and ease of development for engineering systems. Remote sensing research and developments efforts create new algorithms, software, and hardware that extend the field's capabilities. As institutions such as National Aeronautics and Space Administration (NASA) or the National Science Foundation

(NSF) declare their decadal goals, both researchers and manufacturers make efforts to attain those goals. As surrounding areas of research grow, new technologies are made available to remote sensing. For example, the decreasing costs of unmanned aerial system (UAS)s have afforded researchers the ability to explore this field without large financial investment. [12, 29, 76]

These three patterns have naturally raised interest in MRS through SoOp. SoOp is a MRS technique that exploits anthropogenic signal sources in a bistatic radar configuration. Conventionally for MRS, SoOp remote sensing uses transmitters from space such as communication and navigation satellites (e.g., Global Positioning System (GPS)) to make measurements from ground, air, or space with a custom-built SoOp receiver. MRS has matured significantly since the 1950s through radar and radiometry. SoOp, however, is currently positioned for enthusiastic adoption within the science and engineering community.

From a MRS perspective, the orbits around Earth would ideally consist of scatterometers, synthetic aperture radar (SAR) systems, and radiometers filling the microwave window to allow for monitoring of Earth's natural resources. However, radio frequency (RF) allocation is a resource to be shared among commercial, governmental, military, and scientific interests in addition to the necessary infrastructure for uplink/downlink communications. The current international frequency bandwidths allocated to active/passive remote sensing is shown in Figure 1.1.

Different frequencies have different transmissivities which is an important property for MRS. Frequencies around 1 GHz are used for sensing the upper layer of SM profiles and are known to weaken rapidly within vegetation canopies with water content exceeding 5 kg/m^2. While frequencies at 10 GHz have little volume scattering with snow, values around 20 GHz and higher are largely dominated by volume scattering. Of great importance are very high frequency (VHF)

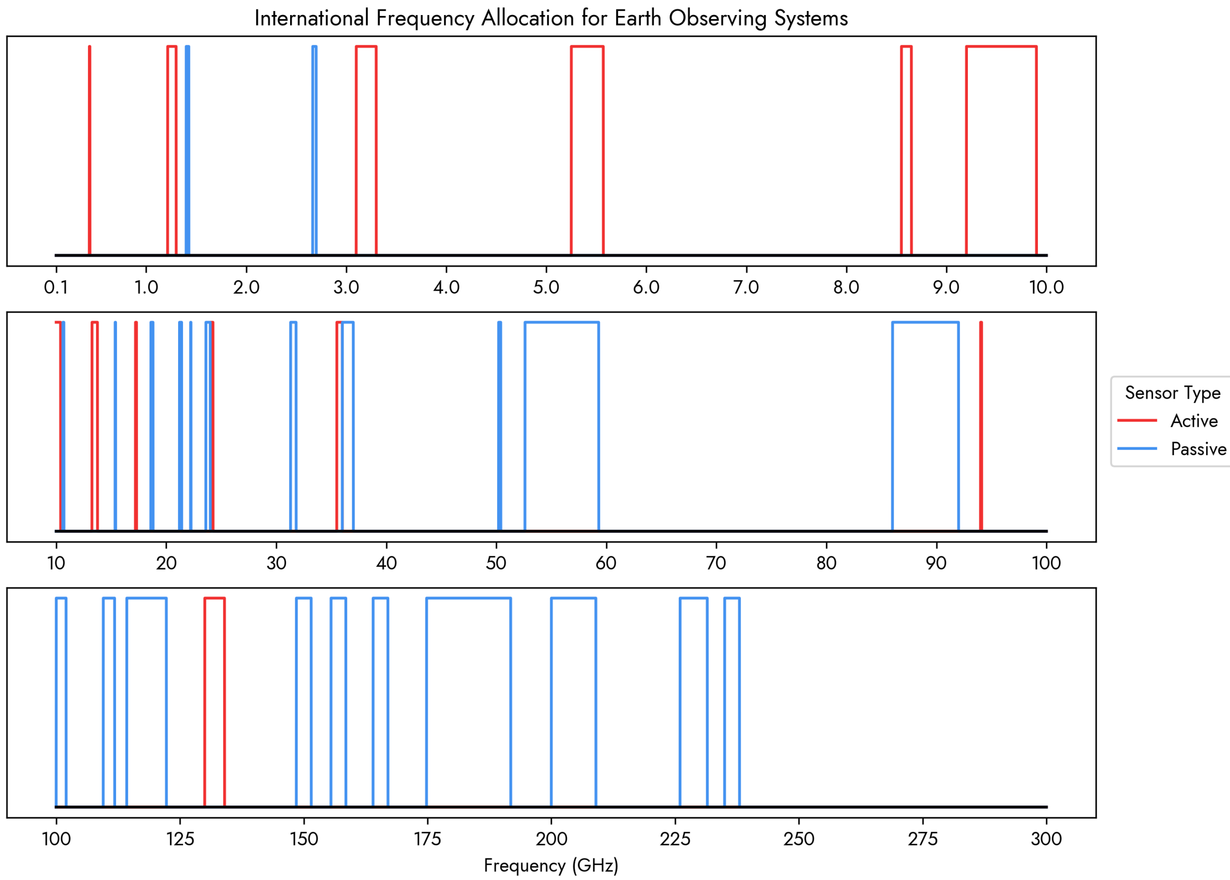

Figure 1.1

United States RF allocation for active and passive remote sensing instruments. Note that allocated bandwidths do not indicate that a satellite system exists in that frequency space. Taken from [1]; 1 July 2022.

and ultra high frequency (UHF) sources (around 100 to 900 MHz) which tend to transmit through dense vegetation canopies and can interact with soil at deeper levels. This portion of the microwave region is heavily used outside of the sciences which makes it difficult for passive techniques due to interference. The large size, weight, and power (SWaP) constraints for creating a science-capable active system is also a limiting factor for science missions.

Both software and hardware advances have made MRS with SoOp an affordable possibility for ground, air, and spaceborne scales. Electronic miniaturization has encouraged the use of small satellites (satellite masses less than 180 kg) and cube satellites, allowing for fleets of low-cost satellite systems. Additionally, software architectures like GNU Radio and a host of commercially available software-defined radio (SDR) systems allow for accessible experimentation with SoOp across all scales.

While SoOp missions have been successfully executed for ocean applications and land missions are underway, SoOp strategies for land applications are still under investigation. Simulations are often reported over areas with simplifying assumptions such as low SM, vegetation, or topography variation. Strategies for developing SoOp MRS techniques for general land purpose applications require robust modeling and simulation (M&S) tools for handling the multiple biomes and surface conditions across the Earth surface.

This dissertation details the advancement of Mississippi State University (MSU)'s SoOp coherent bistatic scattering model (SCoBi) model from a ground-based, single-soil layer model to a spaceborne-capable, multi-layered soil model. The model's capabilities for RZSM remote sensing is presented with suggestions on optimal root-zone sensing techniques. A methodology for open-sourced, end-to-end simulation of bistatic radar scattering over Earth terrain is presented using the facet method (FM).

1.3 Literature Review

1.3.1 Root-zone Soil Moisture Considerations

RZSM generally refers to the upper 1-meter of soil in the context of MRS [3]. RZSM describes the water available for a plant's nutrient uptake nominally near its root system. Thus, RZSM has a clear impact on several areas of science including hydrology modeling, thermal exchange between the earth surface and atmosphere, and crop yield.

Penetration depth is a common metric observed throughout the literature to denote how deep a signal can "see" into a soil moisture profile. L-band signals such as Soil Moisture Active/Passive (SMAP) or Soil Moisture and Ocean Salinity (SMOS) are generally believed to have a penetration depth of 5 cm for example while longer wavelengths should allow for deeper sensing into the soil profile. This metric is one of the primary motivating factors in using signals below L-band for RZSM retrieval. However, the common formulation for penetration depth is based on a two-slab formulation consisting of an air slab ($\varepsilon = 1 - j0$) and another slab of constant dielectric [119]. This metric is insufficient as a "root-zone" value as a single SM layer may not capture the different SM values between the surface and root-zone. This is because the surface is subject to evapotranspiration processes which may cause stronger diurnal fluctuations than those seen deeper within the profile. While some researchers have examined this penetration depth issue in the past [98], the single-layer formulation of penetration depth is still commonly cited within the literature in recent years.

There is currently no global remote sensing tool that is capable of directly measuring RZSM. Systems such as SMAP make use of L-band signals at wavelengths of approximately 20 cm, and metrics for RZSM are produced based on the assimilation of brightness temperature measurements with several Earth system modeling components (e.g., atmospheric circulation modeling, chemistry transport, etc) [99]. In other words, current data products for RZSM are not capable of directly sensing RZSM. For this reason, lower wavelengths such as P-band have garnered interest for the global remote sensing of RZSM.

P-band signals have been studied in backscatter cases throughout the literature, often in support of airborne campaigns such as Airborne Microwave Observatory of Subcanopy and Subsurface

(AirMOSS) or BIOMASS [19,63,103,138]. While BIOMASS is expected to launch in late 2023, it will not be allowed to operate over Europe, Central America, and North America due to operations by the United States Department of Defense [17]. The use of SoOp is particularly exciting as it can leverage signals available between 130 and 370 MHz for MRS [84] while circumventing these radio spectrum restrictions.

The use of SoOp for RZSM retrieval has been assessed in recent years. SoOp has shown to be sensitive to RZSM fluctuations from ground scale [47], and the SoOp Airborne Demonstrator instrument verified that a P-band SoOp receiver can measure the reflected signals from the Mobile User Objective System (MUOS) constellation. The SoOp Airborne Demonstrator showed these measurements are sensitive to changing surface conditions and raised the technology readiness level of this SoOp-based instrument from 3 to 5 [44]. This has lead the development of the SoOp P-band Investigation (SNOOPI) system [48], a spaceborne experimental receiver which will assess the capability of a P-band SoOp receiver to remotely sense changes in RZSM as well as snow water equivalent (SWE). With SNOOPI's launch date approaching, there is an expressed need for modeling RZSM over large-scale earth topography from spaceborne scales using SoOp sources.

1.3.2 Spaceborne Modeling Considerations

Much research has been devoted to the topic of radar scattering from spaceborne scales. The numerous methods found in the literature are choosing between the balance of computational speed and physical accuracy. A perfectly accurate model would require perfect knowledge of all phenomenon within the bistatic configuration. However, such information (if it were to exist) would not only be unwieldy to store and automate, but the numerical evaluation of electromagnetic interactions for this perfect information at spaceborne scales would require exorbitant computational resources to evaluate at any reasonable length of time. It is for this reason the literature varies in its many methods.

The distinction of spaceborne electromagnetic scattering from its ground-based variant is (1) the higher heterogeneity of the surface and (2) the multiple levels of surface roughness that impact the received field. While the various dielectric layers and volumes of the surface can be handled by discretizing a given model, the impact of surface roughness requires special consideration.

Many surfaces can be discretized into infinitely many combinations of roughness scales. For example, smooth grasslands can be discretized from centimeter-level undulations to kilometer-level undulations. For land surface applications, it is common practice to discretize the earth into two- or three-level roughness regimes between centimeter and 100-meter scales of undulations for simulation purposes.

For roughness scales where the surface is considerably smaller than the wavelength, small-perturbation methods are often used to account for scattering towards the receiver. This method requires that small surface roughness conditions ($ks \ll 1$) and low correlation length conditions ($kl < 3$) [119]. For conditions where the surface is considerably large compared to the wavelength, the Kirchhoff approximation (KA) is employed. The KA is broken into two scattering regimes wherein high surface roughness ($ks > 3$) are accounted with the geometrical optics (GO) approximation and slower surface undulations ($ks < 3$) use a method known as the physical optics (PO) approximation. These methods are ultimately approximations for the Stratton-Chu integral.

The integral equation method (IEM) was developed by Fung et al. to eliminate the need to consider "validity regions" for surface roughness conditions relative to the wavelength. It is a comprehensive model that uses both small perturbation method (SPM) and KA in addition to a new formulation that bridges the validity region between these models. However, due to the computational complexity of the model, most spaceborne applications for SoOp forego this formulation in an effort to make roughness simulations over hundreds of square kilometers computationally manageable.

Before discussing land applications, it is worth noting the trends in the more mature area of ocean remote sensing with SoOp. GO is the current dominant method for calculating scattering over ocean surfaces. This method makes use of ocean statistical properties to estimate the ocean surface conditions. Because the model relies on ocean statistics instead of explicit modeling of the sea surface, GO is a relatively efficient model. However, due to its reliance on statistical behavior, the pathlength of the wave is not explicitly preserved and can no longer be deemed coherent. Ohio State University has developed an incoherent model which uses Hagfor's Law to expand the KA to estimate specular and non-specular scattering up to a cutoff frequency for exponentially and Gaussian-correlated surfaces [57]. This model has primarily been used for ocean applications, but its observations on ocean surface roughness sensitivity have been used to suggest land surfaces may have diffuse-dominant contributions in measurements [2].

1.3.3 Current Spaceborne Model Implementations

The current literature can be grouped by various methods used to estimate reflections, diffraction, and incoherent scattering from earth's surface. We group these models into (1.) incoherent methods, (2.) coherent methods, and (3). hybrid models.

Xu et al. [125] uses a PO-based approach for land scattering. The model is deemed partially coherent as a number of scattering facets will have coherently summed components and another set of facets will be summed incoherently depending on the phase distribution of the surface. The model uses three-scale surface roughness where, following the paper's terminology, the surface is defined by $z = f_1(x, y) + f_2(x, y) + f_3(x, y)$ where f_1 defines centimeter-scale roughness, f_2 defines roughness values greater than 5-cm and correlation lengths between 0.5 and 10 meters, and f_3 defines topography taken from DEMs. A three-dimensional Numerical Maxwell Model (NMM3D) is used to calculate microwave roughness contributions and incoherent power while a KA is used for larger, slow undulations. The model is capable of calculating scattering from small facet-sizes (2 cm in size) but requires computation time on the scale of days using high-performance computing clusters [52].

Park et al. makes use of a generalized end-to-end simulator titled GARCA/GEROS-SIM4Land [87] to estimate radiative-transfer-based scattering over earth. It makes use of the previously established Synthetic Aperture Interferometric Radiometer Performance Simulator (SAIRPS) [16] for its foundation. The size of the facets used by this model appears to come directly from the DEM provided. Under the evaluation in [87], the model appears to use facets of one arc-minute, or approximately 1800-meters in size near the equator. It has been used for comparison against TDS-1 measurements over areas of high topography.

Campbell et al. uses a GO-based technique for land scattering which has been titled improved GO with topography (IGOT) [15]. The method is an application of Zavorotny's GO [134] to land surfaces with the distinction that land surfaces are deterministic in comparison to time-varying sea surface conditions. The model is a two-component roughness model defined by the Digital

Elevation Map (DEM) and a random component defining the roughness along the surface. The GO method has also been used in land applications by other groups to estimate delay-Doppler map (DDM)s. Xu et al. have also made use of a radiative-transfer-based implementation of geometric optics to validate their scattering models [125]. It is found in Xu's work that GO maintains good agreement with their implementation of KA under their simulation assumptions when large facets ($\geq$ 30 m) are used.

Dente et al. make use of a hybrid model which combines radiative-transfer-based incoherent modeling with coherent scattering to produce a total DDM [32, 33, 95]. The model uses different models to calculate incoherent and coherent components of the received signal. The incoherent component is evaluated through the advanced integral equation method while the coherent component makes use of the KA. The coherent component assumes Gaussian-beam antennas for transmitter and receiver to simplify the expression of the scattered field. This is used to evaluate a normalized bistatic radar cross-section (NBRCS) of the scattering facet. The model is capable of producing simulations over bare and vegetated surfaces with sloped terrain. The model was tested over multiple spatial resolutions ranging from 100 to 1000 meters.

While not used explicitly in land applications, an implementation of the PO expression known as the FM has been expressed in the literature. It is commonly used in applications such as planetary sounding wherein frequencies between 1 and several hundred megahertz are used to model the multilayered surfaces of low-dielectric planets such as Mars [50, 79, 82]. The FM was previously implemented for ocean applications by Clarizia et al [26].

1.3.4 The SoOp Coherent Bistatic Model (SCoBi)

The SCoBi model was open-sourced in 2018 to address several needs for SoOp applications. The model is designed for ease of modification by representing the received field as network scattering parameters which can be characterized as plane or spherical waves as needed [122]. This explicit treatment of fields through scattering matrix representation allows for compact descriptions of antenna purity; polarization rotation effects by transmitter, receiver, or external sources such as ionospheric rotations; and polarization-specific gain patterns. The received field quantity $\underline{b}$ is a 2×1 column vector representing co- and cross-polarized received signal quantities of units $\frac{V/m}{\sqrt{Z}}$ where Z represents the system impedance. Thus, $|\underline{b}|^2$ directly results in the power of the received signal for a given dielectric medium. The compact nature of this formulation is expressed in [65, equations 4.a, 5, and 12].

Building on decades of research in vegetation scattering (e.g. [68, 104]) to produce an open-sourced model for SoOp capable of modeling SoOp interaction through sparse media. Following traditional approaches for the multiple scattering of waves, vegetation is modeled as a homogenous, equivalent medium through Foldy-Lax theory, and the scattering from discrete elements is modeled through a distorted Borne approximation where the total field in any given scattering direction is considered to be the sum of the induced currents under Huygen's principle while maintainging far-field assumptions for transmitter and receiver.

Given the generalized structure of this framework, new modules can be created with relative ease and integrated into the full formulation as described in [65]. Motivated by this, this dissertation adds to this framework to address several areas of need in SoOp remote sensing. These needs can be briefly summarized as the need to model multilayer, dielectric profiles from ground, air, and spaceborne scales as well as the need to succinctly model topography over very large areas.

1.4 Contributions

SoOp presents several distinct challenges for modeling in terms of efficiency. This dissertation contributes several modeling and simulation tools and analyses to the literature to improve the current SoOp modeling and retrieval capabilities as well as future SoOp constellation designs. These contributions include:

- An open-sourced model designed to address multilayer RZSM applications for SoOp
- A design study which seeks an optimal RZSM retrieval configuration by using multiple SoOp sources
- A numerical solution to the KA which maximizes computational efficiency for landscattering applications
- A modeling framework which can enable analysis of RZSM, vegetation structure, and DDM variability for spaceborne applications

These contributions in conjunction with one another create a progression from the original SCoBi model which assumes a single SM layer under vegetation to a spaceborne model capable of modeling vegetation and RZSM profiles simultaneously. Future applications of this model are expected to help assess the impact of surface features on SoOp measurements from ground, air, and space.

1.5 Outline

This dissertation primarily consists of journal publications submitted during the research phases of this dissertation. Each section addresses a unique aspect of SoOp modeling challenges and contain their own literature review and conclusions.

Chapter II establishes the multilayer module of SCoBi. This module joins a physical optics solution for Gaussian-distributed surfaces of centimeter-scale roughness with an iterative solution for determining multilayer reflection and transmissions for arbitrary dielectric media. As single-layer penetration depth is a common metric which motivates the use of SoOp below 1500 MHz, we create an iterative penetration depth formulation for multilayer dielectric structure which more accurately indicates the attenuation of SoOp through RZSM profiles. A simulation study is performed to assess the variability of different SoOp sources for single and multilayer SM profiles. Different frequency sources are shown to be a promising source of information for retrieval, and the importance of dielectric contrast for layer reflections is clearly visualized.

Chapter III builds on Chapter II by assessing a potential RZSM method using a two-layer representation of SM profiles. By using the Cramer-Rao lower bound (CRLB), we assess the lowest possible retrieval error for different SM configurations and SoOp combinations. For a two-layer profile, the top layer is denoted as surface SM and the second layer as RZSM. The use of two or more frequency sources is found to be the most important configuration requirement for achieving SMAP's standard maximum retrieval error of 4%. Using one SoOp source above and another below 1575 MHz results in extremely low CRLB for surface SM and generally retrievable RZSM for moderately wet soils when the RZSM layer is situated at 30 cm.

Chapter IV contextualizes a solution of the Stratton-Chu integral for large-scale land applications using SoOp. The combined effects of variable bistatic geometry, surface conditions, and the matched-filtering-like nature of SoOp cross-correlation in creating DDMs results in the need to model areas upwards of 300 km from the specular point in order to model a DDM such as Cyclone Global Navigation Satellite System (CYGNSS). Such scales will undoubtedly feature mixed surface slope distributions which may not be easily solved analytically. Here, we present a nested facet method (NFM) which makes use of facets along an equal-area projection to estimate signal scattering within the constraints of the KA's limitation on surface roughness and radius of curvature. This method allows for the nesting of multiple surface roughness types which can enable the study of heterogenous surface areas over Earth. The model is proven capable of running large-scale simulations on consumer-grade computers through parallel CPU processing with manageable computation time given the complexity of the surface heterogeneity.

Chapter V combines the modeling approaches of Chapters II and IV in addition to the model of [65] to create a spaceborne framework generalized SoOp applications. This section describes the model analytically and structurally to describe modeling outputs as well as the flexibility of modeling capabilities. As DDMs are the primary measurements of spaceborne SoOp systems, the model is structured to describe the scattered electric field and the simulated DDM. The model is composed of 5 modules: (1.) a manager module for handling data input and output, (2.) a geometry module for communication between several coordinate reference system (CRS), (3.) a data mapping module for autonomous decision making of unknown surfaces variables, (4.) a scattering module which determines the linearly polarized scattering matrix for both vegetated and non-vegetated surfaces, and (5.) a generalized DDM module.

Chapter VI summarizes the conclusions of this dissertation. Future work is discussed to anticipate the needs of both this models capabilities as well as the general needs of the SoOp community. Emerging trends such as transmissivity and snow analysis are discussed, and improvements to this model are suggested in order to meet the needs of these future experiments.

CHAPTER II

GROUND-BASED MULTILAYER SCOBI MODEL

This section is inherited from the following publication [8]

D. Boyd, M. Kurum, O. Eroglu, A.C. Gurbuz, J. Garrison, B. Nold, R. Bindlish, J. Piepmeier, M. Vega, ”SCoBi Multilayer: A Signals of Opportunity Reflectometry Model for Multilayer Dielectric Reflections,” *MDPI Remote Sensing*, vol. 12, no. 11, pp. 3480, 2020. doi:10.3390/rs12213480

2.1 Abstract

A multilayer module is incorporated into SoOp coherent bistatic scattering model (SCoBi) for determining the reflections and propagation of electric fields within a series of multilayer dielectric slabs. This module can be used in conjunction with other SCoBi components to simulate complex, bistatic simulation schemes that include features such as surface roughness, vegetation, antenna effects, and multilayer soil moisture interactions on the reflected and measured signals. This paper introduces the physics underlying the multilayer module and utilizes it to perform a simulation study of the response of SoOp Reflectometry (SoOp-R) measurements with respect to subsurface soil moisture parameters. For a frequency range of 100-2400 MHz, it is seen that the

SoOp-R response to a single dielectric slab is mostly frequency insensitive, however, the SoOp-R response to multilayer dielectric slabs will vary between frequencies. The relationship between SoOp-R reflectivity and the contributing depth is visualized, and the results show that SoOp-R measurements can display sensitivity to soil moisture below the penetration depth. By simulation of simple soil moisture profiles with different wetting and drying gradients, the dielectric contrast between layers is shown to be the greatest contributing factor to subsurface soil moisture sensitivity. Overall, it is observed that different frequencies can sense different areas of a soil moisture profile, and this behavior can enable subsurface soil moisture data products from SoOp-R observations.

2.2 Introduction

Recent investments into GNSS reflectometry (GNSS-R) for ocean applications have vitalized research into SoOp-R for land-based remote sensing areas. The work of [51,56,102] has shown that GNSS signals can be used to monitor ocean surface roughness and wind vectors from spaceborne SoOp-R measurements. This success has inspired research in the use of the Cyclone Global Navigation Satellite System (CYGNSS) GNSS-R constellation for geophysical remote sensing [23, 28, 42] and the future SoOp P-band Investigation (SNOOPI) satellite which is a technology validation mission of P-band reflectometry using SoOp-R to enable spaceborne remote sensing of root-zone soil moisture (RZSM) and snow water equivalent snow water equivalent (SWE) [45]. These SoOp-R experiments inspire a need for modeling tools that provide insight into the interaction between SoOp-R and geophysical parameters.

In recent years, there has been significant development in the use of signals of opportunity (SoOp) sources within the 100 to 2400 MHz range. Specifically, popular frequencies and sources include Orbcomm's private communication satellite system at I-band (137 MHz), the United States Navy's Mobile User Objective System (MUOS) at P-band (240-270 MHz and 360-380 MHz), global navigation satellite system (GNSS) ($\approx$ 1575.42 MHz), and the XM satellite radio system at S-band ($\approx$ 2338 MHz). Recent technology demonstrations and remote sensing experiments have successfully leveraged these signals to detect geophysicals parameters such as soil moisture (SM) and SWE [24, 44, 47, 48, 61, 94, 130].

It is common throughout the literature to cite the penetration depth of signals below L-band as a motivating factor for the use of very high frequency (VHF) and ultra high frequency (UHF) sources as tools for RZSM remote sensing [119]. For both radar and SoOp-R, the compounding effects of propagation, reflection, and SM profile structure will produce a single microwave remote sensing observable which describes all of these non-negligible components. Relating this profile-encompassing measurement to SM values within the root-zone is, therefore, a truly difficult task without proper intuition of the mechanisms which govern the SoOp interaction within the profile. For this reason, robust modeling of these interactions is required.

The SCoBi [65] is a robust framework which allows for the modeling of many SoOp system variables and scattering surface parameters. It is a publicly available model which has been designed to be highly configurable to allow for additional modeling features [40]. Of particular interest to the area of RZSM remote sensing using SoOp-R is the multilayer module which allows for the modeling of arbitrary SM profiles. This module has been used in previous research for investigating the SoOp-R response to RZSM [47], but its underlying physics and methodology has not been introduced in the literature.

This paper serves as a simulation study which investigates the SoOp-R response to RZSM as well as introduces SCoBi's multilayer module. The primary focus of the simulation is to understand the interactions into the subsurface reflection processes which enable RZSM retrieval. To this end, we observe the response of the SCoBi model to a single dielectric slab, variable configurations of two dielectric slabs, and simple polynomial-based SM profile configurations. The governing principles of the SCoBi model's multilayer module are defined. Additionally, we discuss the integration of this module within the publicly available SCoBi modeling and simulation (M&S) package and briefly describe the package's methods that are available for interested users to carry out their own simulation studies.

This paper is divided as follows. Section 2.3 provides a generalized description of the multilayer module and its capability to model RZSM profiles. Section 2.4 discusses the common methodology of this paper across our simulations. Section 2.5 details our analysis of single-, dual-, and multi-slab profiles to highlight relevant parameters. Section 2.6 includes a discussion of the results and potential advancements of this research. Section 2.7 summarizes our results and provides our conclusions.

2.3 Model

The SCoBi model is a fully polarimetric, bistatic scattering model which allows for a wide number of configurable simulation environments for both the bistatic radar system and the scattering surface [65]. SCoBi simulates a three-dimensional space containing a bistatic radar configuration among a source transmitter, a reflecting surface, and a receiver. The SCoBi model determines the received direct, specular, and diffuse components of the signal emitted from the transmitter.

The model is capable of simulating custom receiver antenna patterns, arbitrary radar positions, configurable vegetation canopies, and transmitter frequencies between I- and S-band.

In late 2018, Mississippi State University (MSU)'s Information Processing and Sensing (IMPRESS) publicly released the SCoBi M&S package under a GNU general public license as a means for researchers to conduct simulation studies using SoOp-R in addition to providing a simple, all-in-one interface for newcomers to the field. The SCoBi M&S package along with its documentation is available for download at https://github.com/impresslab/SCoBi. The current version (v1.0.3) features many capabilities such as comprehensive modeling of vegetation effects, bare terrain, surface roughness effects, arbitrary antenna patterns, arbitrary bistatic geometry, and multilayer soil moisture (SM) profiles. The current version is designed for ground-based and airborne geometry and, therefore, assumes a planar Earth surface. Additionally, the publicly available M&S package does not currently feature incoherent reflection coefficient determination but is intended for releasing in the future. More information on the M&S package can be found in [40].

In this section, we introduce the multilayer SM module that is used by SCoBi to determine the reflection processes within a SM profile. We briefly review the relevant components of the core SCoBi model which use the multilayer module. We then discuss this paper's method for determining penetration depth based on this multilayer module. Finally, the tools available in the M&S package are discussed.

2.3.1 Reflection Processes from a Multilayered Dielectric Slab

The SCoBi multilayer module makes direct use of well-established principles which have seen use in many layered structure applications such as radome design, the analysis and synthesis of speech, geophysical signal processing for oil exploration, the probing of tissue by ultrasound, and the design of acoustic reflectors for noise control for many decades [86, 116]. In order to determine the reflection/transmission processes of an incident wave from or into a multilayered dielectric structure, a matrix formulation of the matching at dielectric discontinuities and the propagation within each layer are derived and the reflectivity is recursively solved in the upward direction.

Consider uniform plane waves which are normally incident on a multilayered dielectric structure beneath a slab of mean vegetation medium as shown in Figure 2.1. The vegetation is replaced by an equivalent dielectric constant of ε_{veg} with a depth h via discrete scatterer approach [68] while the dielectric constant of air ε_{air} is unity. The boundary between air and vegetation layer is diffuse since the fraction of vegetation to the total vegetation layer volume is small. The upper portion of the profile (vegetation and air) represents all area above the SM profile wherein freespace path loss, vegetation effects, and systematic influences shape the electromagnetic wave propagating from the transmitter to the surface. The SM profile's surface, designated as a point $z = 0$ m, represents the vegetation-surface boundary position, which is effectively equivalent to air-surface boundary since the vegetation is a sparse medium. The SM profile is represented by a series of M dielectric slabs of thickness l_i, $M+1$ interfaces, and a semi-infinite half-plane wherein the dielectric constant of the M^{th} dielectric slab extends infinitely and downward in to the soil. Each slab features characteristics such as its complex dielectric constant $\varepsilon_i = \varepsilon_i' - j\varepsilon_i''$, wave-number $k_i = 2\pi/\lambda_i$, wavelength λ_i, and complex characteristic impedance η_i. Waves which are propagating through a medium are represented by electric fields (e.g., E_{i-}'). The subscripts $+$ and $-$ are used to denote the wave modes propagating in the positive (downward) and negative (upward) $z-$directions. The prime (or non-primed) fields indicate that quantities are defined right below (or above) each layer interface.

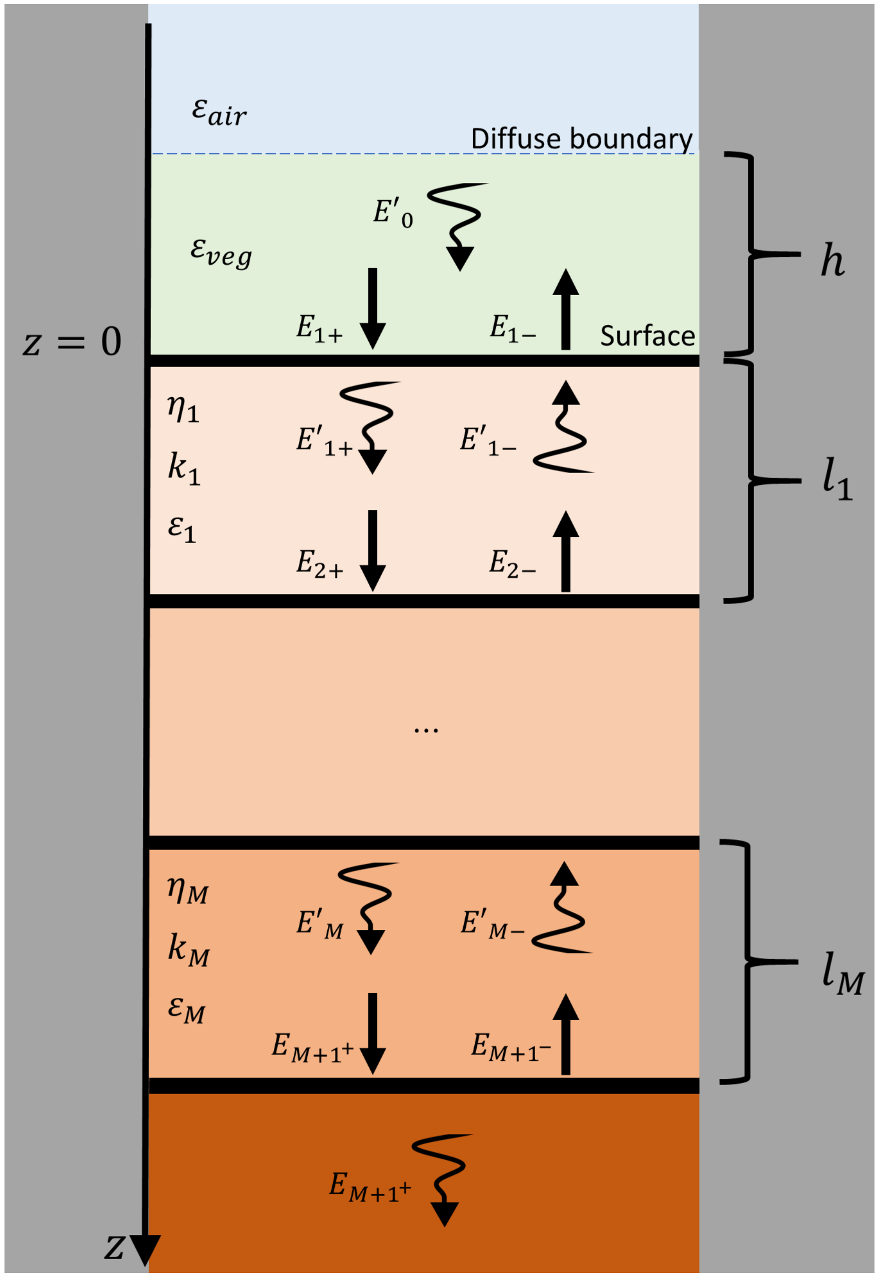

Figure 2.1

Representation of propagation and reflection processes within a discretized soil moisture profile.

Critical values for this structure are the complex valued elementary reflection coefficient $\rho_i = (\eta_i - \eta_{i-1}) / (\eta_i + \eta_{i-1})$ and elementary transmission coefficient $\tau_i = 1 + \rho_i$ across each dielectric interface, where the dielectric contrast between layers is a dominant contributor. The reflection coefficient observed at the surface ($\Gamma_1 = E_{1^-}/E_{1^+}$) is determined through propagation of reflection responses iteratively by initializing the elementary reflection coefficient at the bottom-most interface of the profile with the assumption of no upward waves emanating from the semi-infinite slab. This is called backward-layer recursion as it iterates from bottom to top with decreasing index order. For each dielectric slab, both wave propagation and reflection processes are determined by matching upward and downward fields at each layer and propagating the upward and downward fields from one layer to the next as follows:

$$\begin{bmatrix} E_{i^+} \\ E_{i^-} \end{bmatrix} = \frac{1}{\tau_i} \begin{bmatrix} 1 & \rho_i \\ \rho_i & 1 \end{bmatrix} \begin{bmatrix} e^{j\delta_i} & 0 \\ 0 & e^{-j\delta_i} \end{bmatrix} \begin{bmatrix} E_{(i+1)^+} \\ E_{(i+1)^-} \end{bmatrix} \tag{2.1}$$

where $\delta_i = k_i l_i$ is phase thickness and l_i is the thickness of the i^{th} slab. The first 2×2 matrix factor scaled by reciprocal of τ_i in the right side denotes matching matrix $\underline{\underline{M}}$ while the second 2×2 matrix factor represents propagation matrix $\underline{\underline{P}}$. Multiplying the matrix factors out in Eq. 2.1, we obtain recursions for the intermediate reflection coefficient at each layer boundary with the quotient of the forward propagating wave E_{i^+} and backward reflected E_{i^-} wave as:

$$\Gamma_i = \frac{E_{i^-}}{E_{i^+}} = \frac{\rho_i + \Gamma_{(i+1)} e^{-2j\delta_i}}{1 + \rho_i \Gamma_{(i+1)} e^{-2j\delta_i}} \tag{2.2}$$

where Γ_i is governed by the elementary reflection coefficient ρ_i, the phase thickness δ_i, and the intermediate reflection coefficient $\Gamma_{(i+1)}$ of the previous slab.

To account for polarization and angle for oblique incidence case, the fields are separated into transverse and longitudinal components with respect to the surface normal (the $z-$direction). The transverse components satisfy the identical propagation and matching matrix relationships as in the case of normal incidence with exception of the modification of the media and wave characteristics (e.g., the phase thickness $\delta \longrightarrow \delta_z$ and the characteristics impedance $\eta \longrightarrow \eta_T$) [86]. For oblique incidence (i.e., θ from the surface normal), the longitudinal phase constant is given by $\delta_z = kl \cos\theta$ while the characteristics impedance for horizontal (H) and vertical (V) polarizations are given by $\eta_T = \eta/\cos\theta$ and $\eta_T = \eta\cos\theta$, respectively. The final value (linearly polarized reflection coefficient Γ_1 at the surface) is then used in the SCoBi model as a component of the total reflectometry process by including vegetation and system parameters.

2.3.2 Use of Multilayer Module within SCoBi

Having calculated the Fresnel reflection coefficient from the ground (Γ_1), we now describe how the core SCoBi model uses this term to calculate the total received SoOp-R measurement from the compounding effects of the SoOp-R system and the ground environment. The core SCoBi model makes use of several modules such as bistatic geometry, ground reflection, vegetation effects, and multilayer dielectric structure modules. Note that in some cases such as vegetation and multilayer, not all modules will be used during a simulation depending on the user's simulation requirements. The relationship between the ground reflections and core SCoBi model is explained for the specular component and is used similarly for the incoherent component of the received signal. From an arbitrary geometry, we observe that the signal reflected from the ground takes the form of a ground reflection matrix:

$$\underline{\underline{r}}_g(\theta_s) = \begin{bmatrix} \Gamma_{gp} & 0 \\ 0 & \Gamma_{gq} \end{bmatrix} \tag{2.3}$$

where $\Gamma_{gq} = \Gamma_{1q} e^{-2(k_0 s \cos(\theta_s))^2}$ is the q-polarized Fresnel reflection coefficient of the multilayer dielectric structure as determined by Eq. 4.26 at the surface including the smooth surface roughess represented by the surface root-mean square (RMS) height s. Here, it is assumed that the rough surface under the vegetation is smooth, does not include topography, and follows Kirchhoff's approximation with a Gaussian height distribution. The angle θ_s denotes the angle of specular reflection from the surface, and the subscripts $p \in \{\mathrm{H}, \mathrm{V}\}$ and $q \in \{\mathrm{H}, \mathrm{V}\}$, and as a result, co- and cross-polarized cases are treated simultaneously. From the perspective of the coherent scattering, the reflections from a multilayer profile are embedded within the specular reflection matrix as a matrix product of the incoming and outgoing vegetation transmission matrices $\underline{\underline{t}}$ and the ground reflection matrix $\underline{\underline{r}}_g$, given below:

$$\underline{\underline{r}}_s(\hat{\boldsymbol{o}}_s^+, \hat{\boldsymbol{\imath}}_s^-) = \underline{\underline{t}}(\hat{\boldsymbol{o}}_s^+) \cdot \underline{\underline{r}}_g(\theta_s) \cdot \underline{\underline{t}}(\hat{\boldsymbol{\imath}}_s^-) \tag{2.4}$$

where $\hat{\boldsymbol{\imath}}_s^-$ and $\hat{\boldsymbol{o}}_s^+$ are unit vectors describing the wave propagation in incoming and outgoing directions. The supercripts + and − are used to denote the wave modes propagating away and towards the specular point (SP). The ground reflection matrix is a function of the reflecting angle at the SP θ_s. Under a smooth surface assumption, this value will be equal to the wave's angle of incidence. This specular reflection coefficient can then directly be used by the core SCoBi model to determine the coherent and incoherent components of the received SoOp-R signal. In the absence of vegetation, the vegetation transmission matrix is an identity matrix. The coherent reflection coefficient observed at the receiver terminals is given by

$$\underline{\Gamma}^{coh} = \underline{\underline{g}}_r(\hat{\boldsymbol{o}}_s^+) \cdot \underline{\underline{u}}_{s\rightarrow r}(\hat{\boldsymbol{o}}_s^+) \cdot \underline{\underline{r}}_s(\hat{\boldsymbol{o}}_s^+, \hat{\boldsymbol{i}}_s^-) \cdot \underline{\underline{u}}_{t\rightarrow s}(\hat{\boldsymbol{i}}_s^-) \cdot \underline{\underline{g}}_t(\hat{\boldsymbol{i}}_s^-) \cdot \underline{e}_t \tag{2.5}$$

where the transmit and receive antenna patterns are represented by $\underline{\underline{g}}_t$ and $\underline{\underline{g}}_r$, respectively, while the polarization basis transformations between SP-to-receiver and transmitter-to-SP are given by $\underline{\underline{u}}_{s\rightarrow r}$ and $\underline{\underline{u}}_{t\rightarrow s}$. The nominal polarization state is given by $\underline{e}_t$. Finally, the specular reflection processes are captured by the $\underline{\underline{r}}_s$ term. This $\underline{\underline{r}}_s$ term contains all of the information for the subsurface reflection processes which are the focus of this paper. A more detailed explanation of the core model functionality is available in [65].

The incoherent reflection coefficient is determined similarly to the coherent case. The incoherent reflection coefficient is calculated using several Monte Carlo simulations, and the multilayer SM gradient is used in the calculation of observed scattering mechanisms (e.g., single, double, and triple bounces) which affects the scattering matrix. More information on the incoherent signal processes can be found in [65]. Details on creating scattering particles in addition to all other simulation environment processes are outlined in [40], [39].

2.3.3 Penetration Depth Calculation

Penetration depth refers to the point within a dielectric media where the signal's energy decays to $1/e \approx 36.8\%$ from the amount available at the air-surface boundary layer. Penetration depth, much like the reflection coefficient of a multilayer dielectric slab, is a single value which exists in a large dynamic range depending on a SM profile's soil texture and moisture content. While penetration depth does not indicate a precise limit to a SoOp-R system's SM sensitivity, it is, nevertheless, a useful metric for describing a SoOp-R system's interaction with a SM profile.

The traditional method of determining penetration depth is given by the inverse of the medium's power absorption coefficient [119]. If a low-loss dielectric (small loss tangent) medium is assumed, the resulting form is established [117].

$$\delta_p = \frac{\lambda\sqrt{\varepsilon'}}{2\pi\varepsilon''} \tag{2.6}$$

This method, while useful, is limited to a single uniform slab and determines the depth at which the power of a signal reaches 36.8% as it propagates *through a single slab at nadir incidence angle*. However, the case of layered media having transmission losses is more complicated. Alternatively, the penetration depth can be modified by multiple dielectric discontinuities composing a SM gradient as illustrated in [5, 13]. SCoBi uses a similar approach for the forward-scattering case seen in SoOp-R by explicitly calculating the transmissivity into the soil layers. In order to analyze the relationship between an arbitrary SM profile and the penetration depth, let us summarize the main steps of the theoretical calculations.

Starting from the incident amplitude E_{1^+}, the transmitted amplitude E'_{i^+} from the soil surface to the i^{th} soil layer can be written as

$$E'_{i^+} = \mathcal{T}_i E_{1^+} \tag{2.7}$$

where $\mathcal{T}_i$ is the intermediate transmission coefficient from the top of the soil to the i^{th} layer (in the downward direction). Note that Eq. 2.7 differs from the elementary transmission coefficient τ_i since it combines all the processes from top to the i^{th} interface. To determine the overall transmission response into the i^{th} layer, we start at the top interface with the relation $E_{1^-} = \Gamma_1 E_{1^+}$, where Γ_1 is first obtained via Eq.4.26. We then successively apply inverse of the matching $\underline{\underline{M}}$ and propagation $\underline{\underline{P}}$ matrices given in Eq. 2.1 to obtain Eq. 2.7. This is called forward layer recursion as it iterates from surface to the i^{th} layer into the soil with increasing index order. The downward-going transmissivity is defined as the fraction of energy transferred to the i^{th} layer relative to the surface and is equal to $|\mathcal{T}_i|^2 \,\mathrm{Re}\,(\eta_0/\eta_i)$. It is calculated using Poynting's theorem and taking the ratio of (time-averaged) transmitted power density at the i^{th} interface ($\mathrm{Re}(1/2\eta_i)|E^{'}_{i^+}|^2$) to (time-averaged) incident power density on the surface ($1/2\eta_0|E_{1^+}|^2$). Assuming fine discretization between boundary layers, the penetration depth can be determined by denoting the layer boundary at which the transmissivity reaches $\approx 36.8\%$. The major difference of this approach from the traditional calculation (Eq. 2.6) is its applicability to layered profiles in which one can analyze the penetration depth as a function of SM profile, incidence angle, and polarization.

2.3.4 Simulation Tools and Soil Moisture Profile Representations

Several simulation tools are given in the SCoBi M&S package that allow the user to explore potential SM profile structures. After providing SM samples and soil texture information to the simulator, the SM values are converted to complex dielectric constant values using one of three provided SM dielectric functions: the Wang model [121], the Dobson-Peplinski model [35,90], and the Mironov model [78]. The Wang model is an empirical model developed using data measured at 1.4 and 5.0 GHz, making it ideal for simulations at L- and C-band under similar soil texture conditions. The Dobson-Peplinski model is an empirical model that has been designed using measurements made between 0.3 and 18 GHz. Finally, the Mironov model is a semi-empirical model that has been validated over a range of 0.3 to 26.5 GHz [77]. Previous studies have shown that the performance accuracy of each model will vary depending on the frequency and soil condition of any given measurement, and, thus, a user may require the use of multiple dielectric models depending on the measurement conditions [75, 129]. The simulator is designed to handle both an ”experiment-based” environment where only a small number of SM values are known via in-situ measurements or cases where each SM value is explicitly defined. To this end, the SCoBi simulator features multiple SM fitting functions which are used in conjunction with the SM dielectric functions.

Currently, four functions exist for mapping SM as a function of depth within the profile: a discrete slab model, a 2nd-order polynomial, 3rd-order polynomial, and a logistic function fit. Given a set of SM values, the model computes the dielectric constant for each SM point, and the dielectric constant between each SM point is fit depending on the selected function. For the dielectric slab fit, each slab extends from the given soil depth to the midpoint between its nearest neighbor. This is performed for all values excluding the values between the surface and the first SM value which will assume the value of SM nearest to the surface. The slabs, themselves, are composed of multiple smaller interfaces as defined by the soil discretization of the user’s choice. If the user defines SM for each depth corresponding to the discretization level, each SM value will be explicitly defined, and a midpoint will not be created. The polynomial fits are the least-squares-best-fit for the dielectric constant of the profile as specified by the user. The logistic fit is that of an iterative, traditional logistic regression model [55].

To illustrate the SM profile fitting function, the four dielectric fitting functions are visualized in Figure 2.2 using the input parameters of Table 2.1 to define the profile according to the Mironov model with a soil discretization of one millimeter. It should be noted that these values only depict the relative permittivity of the fitting functions. The second-order and third-order polynomial fitting functions place a regression line corresponding to the respective polynomial order given a set of SM samples. Because the number of SM samples match the number of polynomial coefficients, the third-order polynomial is able to perfectly fit each SM sample provided. The third-order polynomial also depicts the simulator's "lower boundary" as the polynomial fit required to create this curve results in values below the dielectric constant of air. The dielectric slab fit depicts the simulator's slab fitting technique which extends the dielectric constant up to the mid-point between each provided SM sample. The logistic fitting function places a logistic curve between each SM sample before remaining constant for the depth remaining after the final provided SM input.

Table 2.1

Example Soil Moisture Profile Information

Depth (cm)	**Soil Moisture**	**Sand Ratio**	**Clay Ratio**	**Soil Bulk Density** (g/cm^3)
5	10%	10%	31%	1.4
10	30%	10%	31%	1.4
20	20%	10%	31%	1.4
40	40%	10%	31%	1.5

2.4 Methodology

Having detailed the SCoBi model and simulator's functionality for modeling multilayer SM profiles, this subsection details the methodology and simulation description for our study of the subsurface reflection processes that will enable RZSM profile inversion. Additionally, we would like to explore the relationship between penetration depth and the response of a SoOp-R system

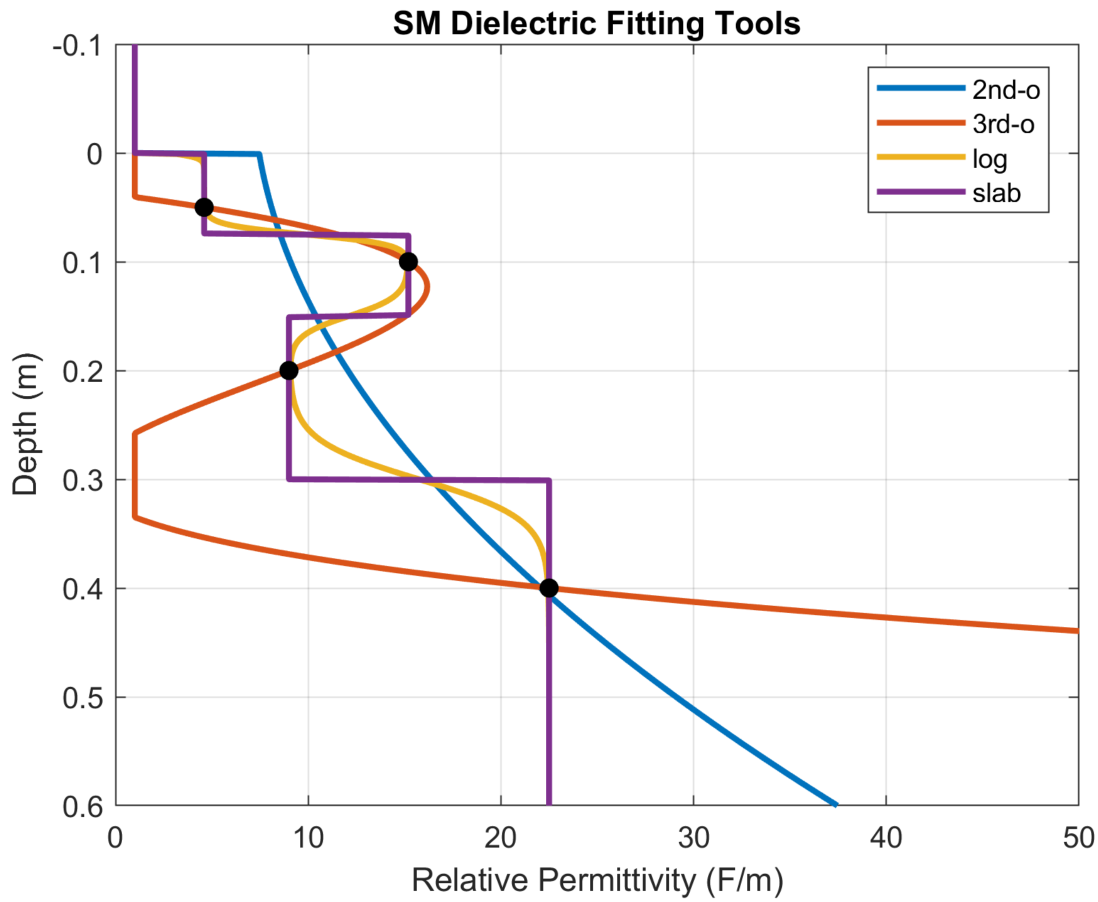

Figure 2.2

Discretized soil moisture profile representation in SCoBi model and simulator package. Each profile is fit using defined dielectric constant values (shown as black points) over a discretized profile. For clarity, only the relative permittivity is shown.

to a profile's depth. For this reason, we will establish the following methodology for obtaining accurate, repeatable SoOp-R simulations using SCoBi.

In order to maintain focus on the response to RZSM and subsurface SM variation, neither surface roughness or vegetation effects are considered. For all simulations, the Mironov model is used [78]. This SM dielectric model is a function of only three variables: frequency, volumetric SM, and the soil's volumetric clay percentage. For most simulations, the clay content is restricted to 31% for most simulations in order to simulate a loamy soil as typically seen in soils intended for crop yield. Each profile is discretized into 1-millimeter interfaces. This is done in order to simulate a continuous SM profile with respect to the incident signal wavelength as opposed to using large dielectric slabs. This discretization is used in this study to create larger dielectric slabs from smaller components (e.g., a 5-cm thick dielectric slab would be composed of 50 one-millimeter slabs of identical dielectric constant values.) This means that the propagation and reflection processes are determined every one millimeter (i.e., account for propagation losses every millimeter and, when applicable, observe signal reflections at dielectrically discontinuous boundary layers.) Unless stated otherwise, all simulations occur at normal incidence. The receiver is assumed to be at low altitude where the earth surface curvature is negligible. As soil substrate composition is widely regarded as having negligible scattering effects in this frequency region, only coherent contributions are considered for these simulations. Because of these simplifications, the observed reflection coefficient ($\underline{\Gamma}^{coh}$ from Equation 2.5) is equal to the surface reflection coefficient (Γ_1 from Equation 4.26.) No incoherent contributions are simulated.

The simulation study in Section 2.5 will examine multiple SM profile configurations as explicitly defined by the M&S package's discrete slab fit function. We examine multiple SM profiles and the SoOp-R response for frequencies between 100 and 2400 MHz. While only a discrete number of communication/navigation sources exist within this region, characterizing the general frequency response in this region is within the general scope of this section. Nearly all simulations are performed at normal incidence.

While some simulations will make use of a frequency sweep across the 100-2400 MHz spectrum, some simulations will take place at discrete frequencies. Due to the popular usage of these bands within SoOp-R experiments throughout the literature, the frequencies at 137.5, 255, 370, 1575.42, and 2338.75 MHz are used for these visualizations.

During simulations involving penetration depth, it is worth noting that the penetration depth is dependent on the polarization of the incidence signal. SCoBi defines these values in terms of linear polarization. For all simulations in this study, the penetration depth is derived from the horizontal component of the emitted signal though we note that for these configurations at normal incidence, neither penetration depth nor reflectivity will change with respect to polarization.

2.4.1 Single Slab Study

Before understanding the multilayer case, it is important to understand how SoOp-R behaves given a single slab of SM. While many simulation studies have been conducted for understanding traditional back-scattering, single-frequency radar systems in relation to SM [18, 67, 85, 103, 109, 118], this study seeks to characterize the forward-scattering, multi-frequency SoOp-R response to various SM profile configurations and controllable receiver variables.

For the initial simulation, we examine the SoOp-R response to a single dielectric slab with values between 5 and 50% SM. The constant SM value extends infinitely from the surface of the soil downwards. All incident signals assume a right-hand circular polarized transmitter. The incident angle along the surface is taken at normal incidence in nearly all simulations. The dielectric constant of SM with respect to frequency is also examined.

2.4.2 Dual Slab Study

We now analyze the response to two dielectric slabs. Two studies are performed: a study showing the SoOp-R response of dual-slab profiles to (1) depth of the second slab, (2) frequency and incidence angle, and (3) soil texture.

In these dual slab simulations, two parallel slabs of soil moisture are placed on top of one another where the first slab acts as a constant SM layer from the air-surface boundary to a defined depth, and the second slab extends semi-infinitely downward. While we acknowledge that such a simple representation may not represent the ”true” response of SM profiles to SoOp sources, the analysis of dual-slab profiles allows us to more easily comprehend the new contributions induced by multilayer SM slabs.

For the first study, the first slab will take values of 20, 30, and 40% SM, while the underlying slab is fixed at a value of 50% SM. While such levels of difference in SM may be uncommon, this is done in order to maximize potential reflections beneath the upper slab and visualize signatures which can be extended into more realistic SM profiles. The primary observables seen in this study will be that of the resultant reflection coefficient, the penetration depth, and the transmissivity of the signal as it passes through the 1-millimeter interfaces across the two dielectric slabs. Only two constant dielectric slabs will be present for each SM profile configuration. This is done in order to quantify the effect that varying the position of a second dielectric slab has on the measured reflectivity.

While penetration depth provides an indication of the location within the profile that a signal's energy falls to 36.8% of its incident energy, direct analysis of a SoOp system's reflectivity response to different SM profile configurations can provide an understanding of the limitations of a SoOp receiver system. In order to provide a metric for monitoring SoOp-R's change in reflectivity as a function of the position of a second dielectric slab beneath a constant SM slab, we seek to determine a depth within the two-layered SM profile where the reflectivity falls below a defined threshold. This depth, referred to as a ”saturation depth” for this study, is obtained by lowering the second slab into the profile to such an extent that changes in reflectivity can no longer be observed as a function of the second slab's location to a user-defined threshold level. In our example, it is assumed that reflectivity does not vary significantly beyond one meter. Over the range of 1 to 2 meters, a mean value of the reflection coefficient is obtained by averaging the reflection coefficients for multiple two-layer SM profile configurations to obtain a “saturated reflectivity.” We then iterate backwards from the bottom-most layer towards the surface and establish a depth at which the reflectivity deviates by a user-specified amount from the saturated reflectivity. For the purposes of our problem, we assume that our system can confidently determine reflectivity up to 1% accuracy. Thus, we seek to use this metric to determine the depth at which the two-slab profile sees fluctuations in coherency that are greater than 1%.

For the second part of this study, fixed dual-slab profiles will be analyzed with respect to frequency and incidence angle. The profiles consist of a first slab with a dielectric constant value derived from the Mironov SM dielectric model, and the lower layer is an arbitrary, high-dielectric constant value beneath the SM layer. The lower layer dielectric constant is defined by the Mironov dielectric model for 50% SM. Two slabs are shown as an example at 10% SM and 30% SM. The four profiles consist of the first slab extending from the surface (0 meters) to the second slab at 0.2, 0.3, 0.4, and 0.5 meters. The horizontal component of the incident wave is analyzed with an angle of normal incidence to determine the transmissivity and penetration depth values.

In the third portion of this dual-slab study, the effect of soil texture on SoOp-R measurements is discussed. Soil texture, typically defined as the amount of sand, silt, and clay shared within a soil layer, is a dependency for many soil dielectric mixing models. SM content is generally the dominating variable for these mixing models due to water's high permittivity, and the distribution of water content within the soil volume can vary the dielectric constant. The use of soil texture and SM as soil dielectric modeling inputs is a common technique dating backing to the 1980s.

The Mironov model used by this paper is a function of frequency, SM, and clay content. In this section, the impact of clay uncertainty on SoOp-R measurements is reported using a study of two slabs. The slabs are are separated by a dielectric interface located at 15 cm. Two profile configurations are used. The first and second dielectric slabs contain 15 and 30% SM in one configuration. 30 and 15% SM are used in another configuration for slab 1 and slab 2. Because the Mironov model is only a function of clay, the change in reflectivity is visualized across a range of 5 to 45% clay content within the first and second slab. Because soil dielectric constant behaves non-linearly in the Mironov dielectric model as a function of SM and clay, the results are plotted by taking the absolute difference between clay content configurations and the "true" clay content value (25% for both slabs.) The results visualize how different combinations of clay values can produce similar reflectivity values when the clay content of the first and second slab's clay content is varied.

2.4.3 Arbitrary Profile Study

After performing simulations on both single and dual-slab profiles, we now view the response of SoOp-R to profiles which feature dielectric constant changes at nearly every interface. In other words, this study seeks to visualize the subsurface contributions from a variable, arbitrary SM profiles on the reflection coefficient. Specifically, we show how the reflection coefficient changes between layers as the iterative method computes the reflection coefficient from the bottom-most interface as it ascends towards the surface. To this end, we visualize three components: several SM profiles, the elementary reflection coefficient derived from the dielectric contrast between each interface, and the intermediate reflection coefficient taken from Eq. 4.26 viewed at the i^{th} interface of each SM profile. The intermediate reflection coefficient values (Γ_i) are terms used to solve for the surface reflection coefficient (Γ_1) that are influenced by the subsurface SM structure. We note that SoOp-R measurements cannot directly measure the intermediate reflection coefficients at these subsurface interfaces. However, such a simulation can help visualize the effects that highly discretized dielectric constant gradients have on multifrequency SoOp-R signals as they propagate through a complex, smoothly-varying SM profile under the SCoBi modeling assumptions.

In the previous studies, we examine SM profiles consisting of either one or two distinct dielectric constant values within the profile. We now examine SM as a function of either 1st- or 2nd-degree order polynomial fitting. We choose the following format to mathematically describe SM profiles as provided in [109]:

$$\theta_{SM}(z) = a_2 z^2 + a_1 z + a_0 \tag{2.8}$$

Where a_2, a_1, and a_0 represent polynomial coefficients, and z represents the SM profile depth in meters. In addition to these parameters, the SM profile is bounded between 3 and 50% volumetric SM for any given polynomial coefficient. The discretization of z assumes an interface every 1 millimeter. Under such a discretization, the subsequent results should allow us to visualize the contributions of heterogeneous areas in the upper portion of the profile [137], which are known to be significant in altering the reflected energy, as well as from deeper portions of the profile.

While it is clear that SM profiles are shaped by many factors including thermal and capillary processes, we use a polynomial function in order to approximate an arbitrary, high-resolution profile under easily configurable conditions. It is not the intent of this simulation to model highly realistic SM profiles, however, it is our goal to depict variable, simple SM conditions with easily depicted changes in the SM gradient to illustrate how SoOp-R measurements behave as arbitrary profiles change.

2.5 Results

This section contains the results of three simulation studies: simulations performed using a single SM value for a semi-infinite dielectric slab, a two-slab study of penetration depth, frequency, and incidence angle, and a study of subsurface reflection coefficient changes using arbitrary profiles represented by simple lines and polynomials. Each of these simulations allows us to look at different aspects of SoOp-R's response to changes in the specular, forward-scattering reflection coefficient as well as the interactions with RZSM.

2.5.1 Single Slab

Figure 2.3 depicts the behavior of the real and imaginary reflection coefficient as well as reflectivity for a frequency sweep between 100 MHz and 2400 MHz with 1 Hz resolution. The commonly referenced SoOp-R sources are depicted as black dashed lines at the corresponding frequency location along the x-axis. In addition to the response of SM, the response of the same frequencies to pure water is shown in Figure 2.3(a) using the model shown in [119]. Between

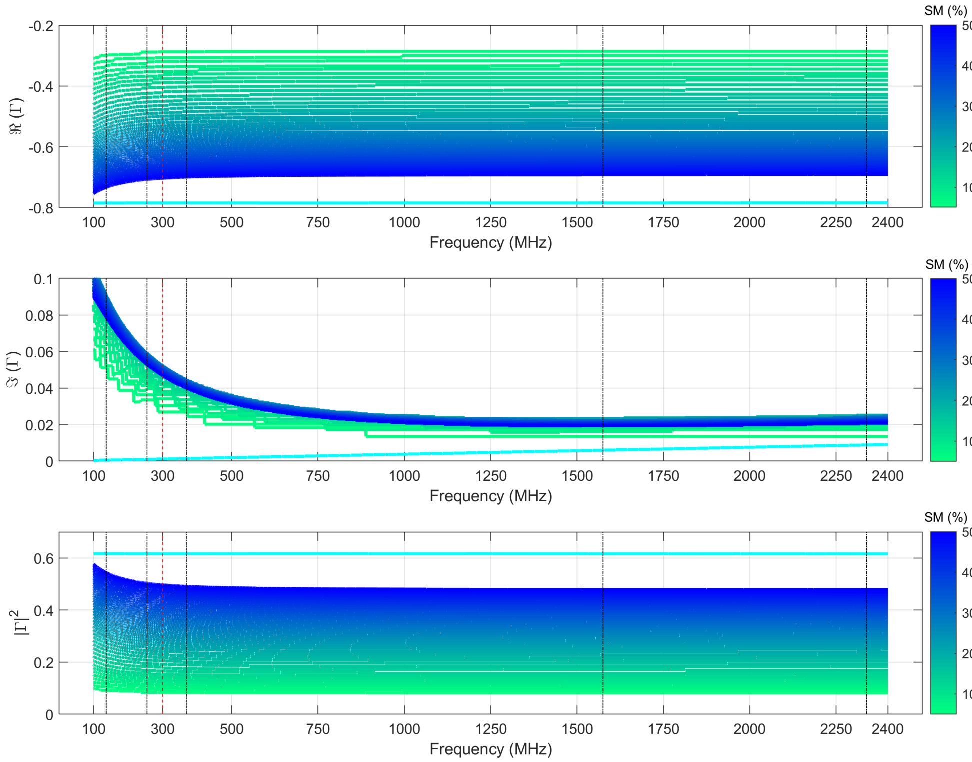

Figure 2.3

Real, imaginary, and magnitude square of the measured reflection coefficient. The color gradient shows the reflection coefficient values for soil moisture between 5 and 50%, and the cyan line shows the reflection coefficient values of water for the given frequency range. The black, dashed lines show the position of the commonly referenced SoOp-R sources, and the red dashed line shows the lower validation region of the Mironov dielectric model. All measurements are performed at normal incidence.

300 MHz and 2400 MHz, the real component of the reflection coefficient is largely frequency insensitive. If the real component of the reflection coefficient is considered as a function of SM, it can be seen that the real component of the reflection coefficient increases in magnitude as a function of SM content. For the imaginary portion of the measurement, theSoOp-R values take on a curvature with respect to frequency, and for most values above 1000 MHz, the values are largely

the same. When examining the reflectivity, similar frequency regimes above and below 300 MHz can be seen.

While the reflectivity does appear to vary below 300 MHz, all values above 300 MHz appear to primarily be a function of SM with little response to changes in frequency. To investigate this, the dielectric constant values produced by the Mironov model are simulated using the same SM and frequency values in Figure 2.3. The results are depicted in Figure 2.4 below alongside the dielectric constant of pure water. For the reader's convenience, the single-layer penetration depth values for the corresponding dielectric constant values is plotted in Figure 2.4 using Eq. 2.6.

It is clear that the reflectivity values observed in Figure 2.3c behaves nearly identically to the general pattern of the real component of the dielectric constant seen in Figure 2.4. It can generally be observed that the real component of the dielectric constant is a more dominating component, especially beyond 500 MHz. Thus, the frequency insensitivity observed in the SM dielectric constant creates a generally flat SoOp-R response across frequencies.

As stated previously, the Mironov model [78] is a physics-based approach to determining the dielectric constant of SM that has been validated for frequencies between 300 MHz and 26.5 GHz. While the values have been largely verified over this range, values below 300 MHz, as denoted by the dashed, red line in Figure 2.3 and 2.4, are not guaranteed because the dielectric model for these frequencies was created by fitting dielectric constant measurements to calculations derived from the generalized refractive mixing dielectric model. As such, values below 300 MHz should be used cautiously as these dielectric constant values have not been validated by measurements.

Ultimately, it can be observed that the response of SoOp-R to SM is proportional to the dielectric model used for SM. This experiment was performed with the Dobson-Peplinski model, and the

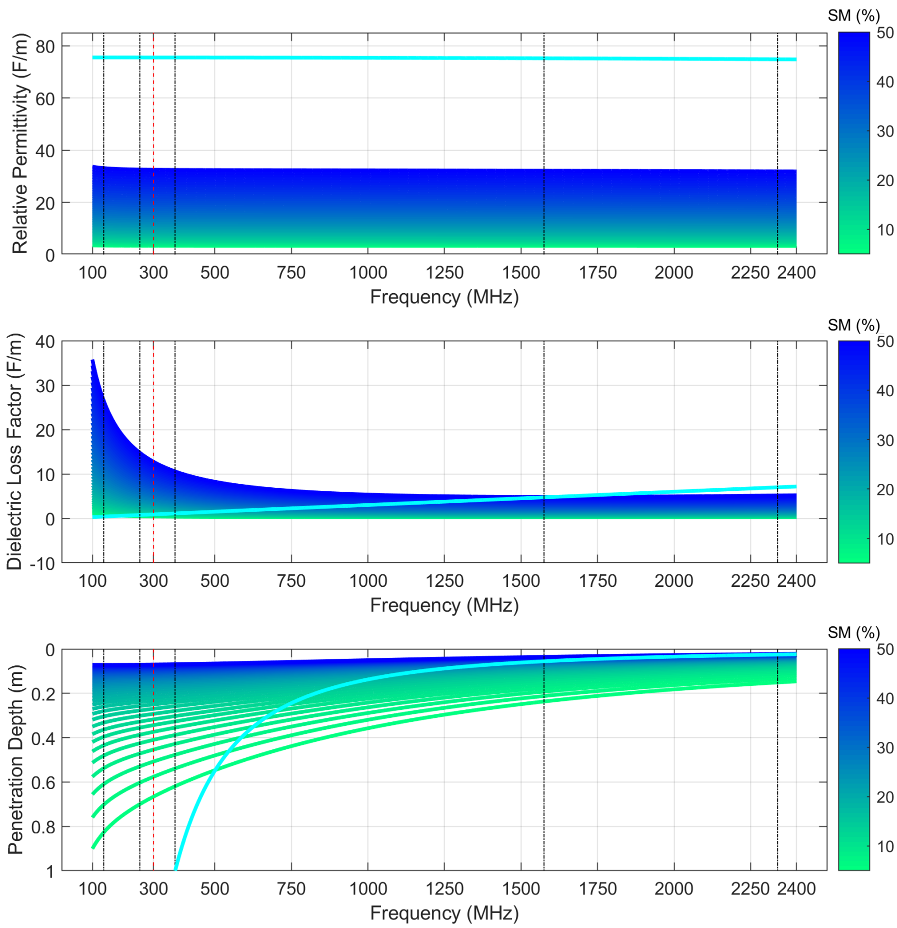

Figure 2.4

Behavior of real and imaginary dielectric constant for multiple soil moisture values as a function of frequency in addition to penetration depth information from Eq. 2.6. The color gradient shows the dielectric constant for soil moisture between 5 and 50%, and the cyan line shows the dielectric constant of water for the given frequency range. The black dashed lines show the position of the commonly referenced SoOp-R sources, and the red dashed line shows the lower validation region of the Mironov dielectric model.

same frequency insensitivity was observed. The Wang model was derived from L- and C-band data only and is not applicable for this frequency sweep simulation.

Understanding that the magnitude of the reflection coefficient from a uniform SM slab does not change drastically across our observed frequency spectrum, we note that the imaginary component of the soil dielectric constant will govern the rate at which these frequencies suffer propagation loss. Different frequencies, by merit of the SM dielectric constant's imaginary component, can potentially observe differences in SoOp-R response to SM profiles based on their moisture content as a function of depth. To investigate this, we now examine the response of SoOp-R to two dielectric slabs in multiple configurations.

2.5.2 Dual Slab Study

2.5.2.1 Saturation Depth of Descending Slab

Using the saturation depth methodology described in Section 2.4, the response of SoOp-R systems at frequencies of 137.5, 255, 370, 1575.42, and 2338.75 MHz is simulated over a series of two slab configurations. Simulations are performed where the first slab uses SM values of 20, 30, and 40%. The results of this simulation are depicted in Figure 2.5.

In the left column of Figure 2.5, we observe the change in reflectivity as the second slab of 50% SM descends into the SM profile. The right column shows the penetration depth for each SM profile configuration as a function of the location of the dielectric boundary between the first and second slabs. The resulting reflectivity alternates about the ”saturated reflectivity” as a function of depth similar to an attenuating sinusoid. This is expected since propagation effects are the primary mechanism that changes reflectivity in this simulation. However, we note that such strong coherent behavior largely exists due to the simple multilayer waveguide structure used in this simulation and that physical SM profiles may not exhibit this exact behavior.

The dramatic increases in penetration depth seen when the second slab lies within the upper 20 centimeters of the profile is dominantly driven by the real component of the reflection coefficient approaching zero. This is a property of the coherent nature of the SoOp-R signals. Thus, for

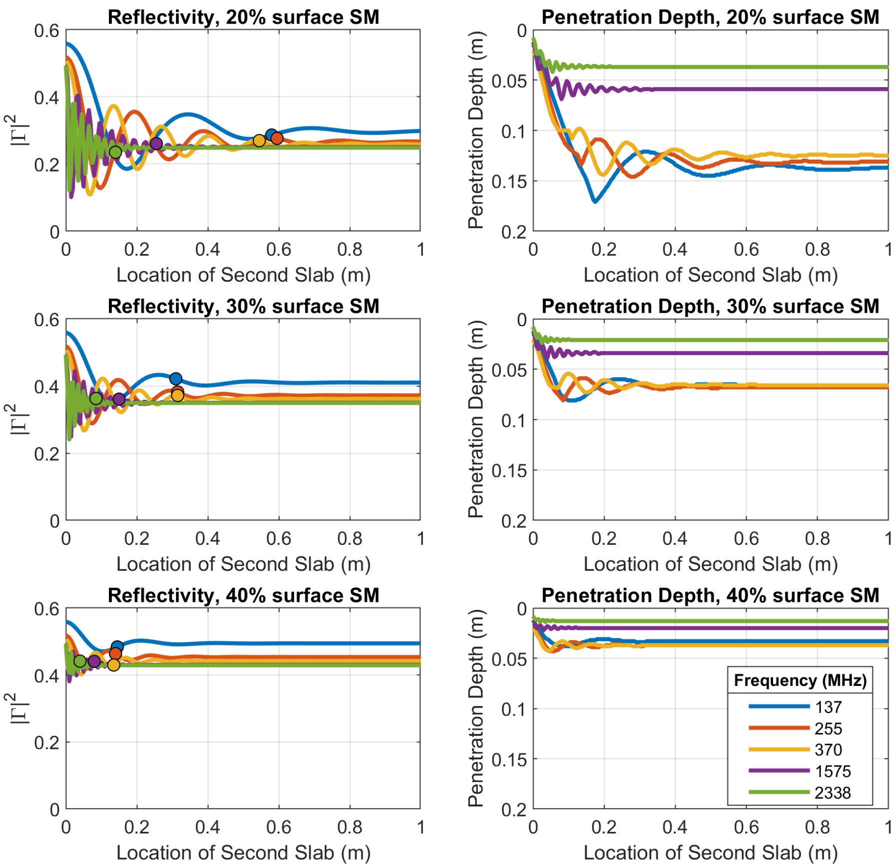

Figure 2.5

(Left column) Changes in reflectivity due to moving a secondary slab beneath a single dielectric slab and (right column) the corresponding penetration depth for each dual-slab configuration. Each row assumes that the first slab's SM value is 20, 30, and 40% SM respectively, and all simulations assume a second slab SM of 50% SM.

specific SM profile configurations, large values of transmission occur whenever the phase of the reflected signal causes either the real or imaginary component of the reflection coefficient to trend towards zero. For all simulated frequencies, we can observe that variations in both penetration depth and reflectivity are largely saturated before the configuration reaches 1 meter in depth.

Using the aforementioned methodology, the colored points along each separate frequency plot in the left column of Figure 2.5 represent the determined saturation depth. By assuming that our

SoOp-R system can detect changes up to ±1% in reflectivity, we observe that reflectivity is affected by changes in dielectric constant occurring at depths deeper than the penetration depth shown in the right column of Figure 2.5 as well as the penetration depth provided by Eq. 2.6. For example, values at 370 MHz under a 20% SM slab is expected to have a penetration depth of 17.9 cm using the traditional penetration depth equation for a single slab (Eq. 2.6). However, by moving a secondary slab beneath this surface slab, we observe SoOp-R responses up to 54.5 centimeters.

Overall, these results suggest that despite the dominantly frequency-independent nature of SoOp-R measurements in relation to SM content, different frequencies are capable of observing changes in reflectivity values based on frequency-dependent propagation and matching properties of a wave traveling through a multilayered medium. Thus, RZSM is potentially measurable by a SoOp-R system by using different wavelengths. Although the method of determining a ”saturation depth” would be more difficult to apply to SM profile configurations that are more complex than a two-slab structure, the general insights obtained show that the contributing area of reflections can extend beyond the penetration depth of a profile. If multiple frequencies can be leveraged, values within the SM profile can potentially be obtained through inversion techniques based on differences in the coherence of the observed reflectivity.

2.5.2.2 Frequency and Angle Response of Dual Slab Configurations

Figure 2.6 depicts the a heatmap of the transmissivity for a frequency sweep of four distinct SM profiles. The white line denotes the location of the second layer across each simulation, and the red curve denotes where the energy has fallen to the level considered to be the penetration depth (≈ -4.3 dB). Additionally, the magenta line shows the location where the energy has fallen to 10%

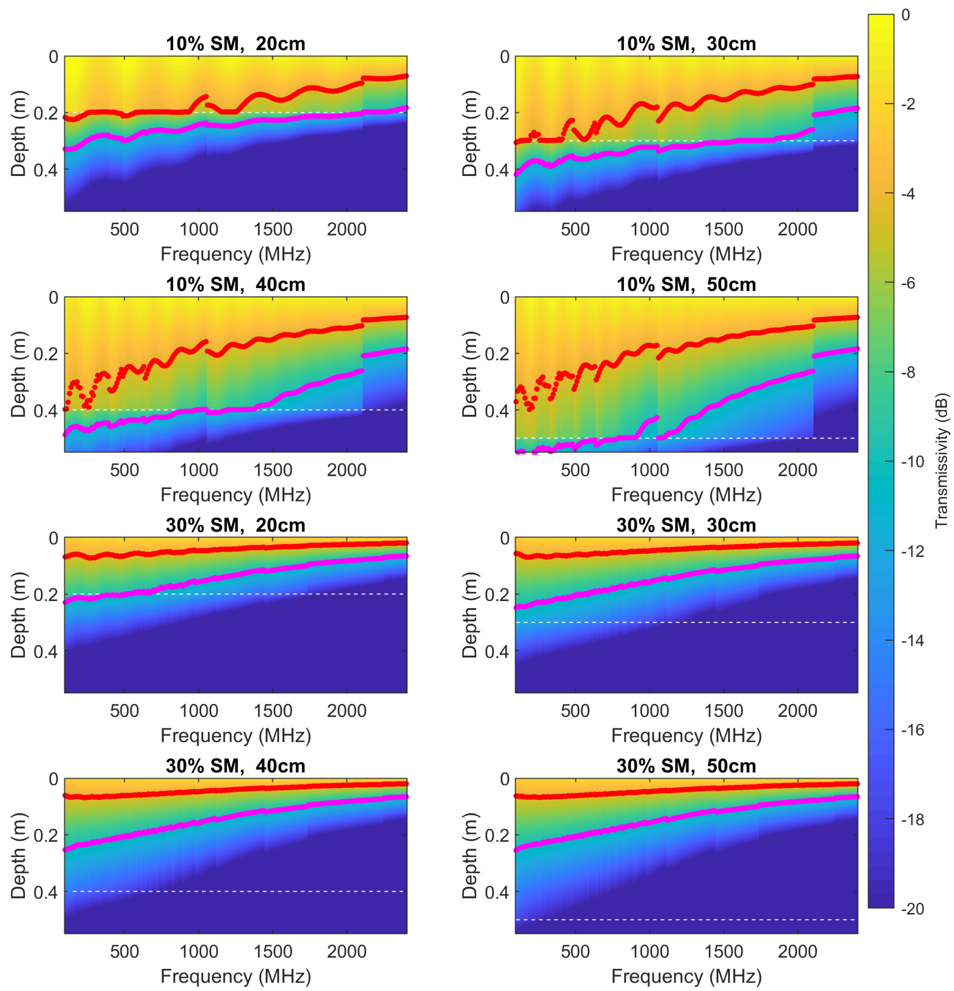

Figure 2.6

Frequency sweep of 4 two-layer profiles. The white lines represent the location of the second layer. The red line represent the penetration depth of the configuration, and the magenta line depicts where the transmittance reaches 10% of its original energy. The first slab SM is 10% for the upper four subplots and 30% for the lower four subplots. The second slab SM is 50% for all subplots.

(-10 dB). For the color axis, the transmissivity of the incident signal is depicted and is bounded between 0 and -20 dB in order to visualize certain coherence properties of this study.

For lower frequencies, the penetration depth occurs near the location of the second dielectric slab. Across the frequency sweep, we can visualize the effects of phase thickness in the calculation of the reflection coefficient. As the high dielectric constant value descends into the profile, the transmittance of the signal oscillates more rapidly across the frequency spectrum. When the SM of the upper layer is increased, we observe higher signal attenuation in addition to faster oscillation across the frequency spectrum.

Across each subplot, the colorbar visualizes the energy of the signal up to the point where 1% (-20 dB) of the energy from the surface remains. It can be observed across the frequency sweep that the transmitted energy and penetration depth varies as a function of frequency despite the previous simulations showing frequency-independence. The coherency effects which cause the penetration depth to fluctuate are largely suppressed at frequencies above L-band for all simulations, and this fluctuation can be further suppressed by increased SM content or larger distance between areas of dielectric contrast. This indicates that, regardless of coherence effects, the use of different frequencies can be leveraged to sense subsurface changes in dielectric constant given a sufficiently sensitive SoOp-R system.

In addition to this frequency sweep, we visualize the transmissivity and penetration depth of a 370 MHz signal as a function of incidence angle as depicted in Figure 2.7. Across all slab configurations, we observe that the penetration depth rapidly approaches zero around 70° incidence. This aligns with many experiments which ignore observations near 70° incidence. Though not depicted, simulations show that the general trend of the effect of changing incidence angle does not vary with frequency. Thus, the significance of different incidence angles for a given profile is that it reduces the total transmissivity of the signal into the SM gradient and, therefore, reduces the contributing area of the SM profile towards the receiver.

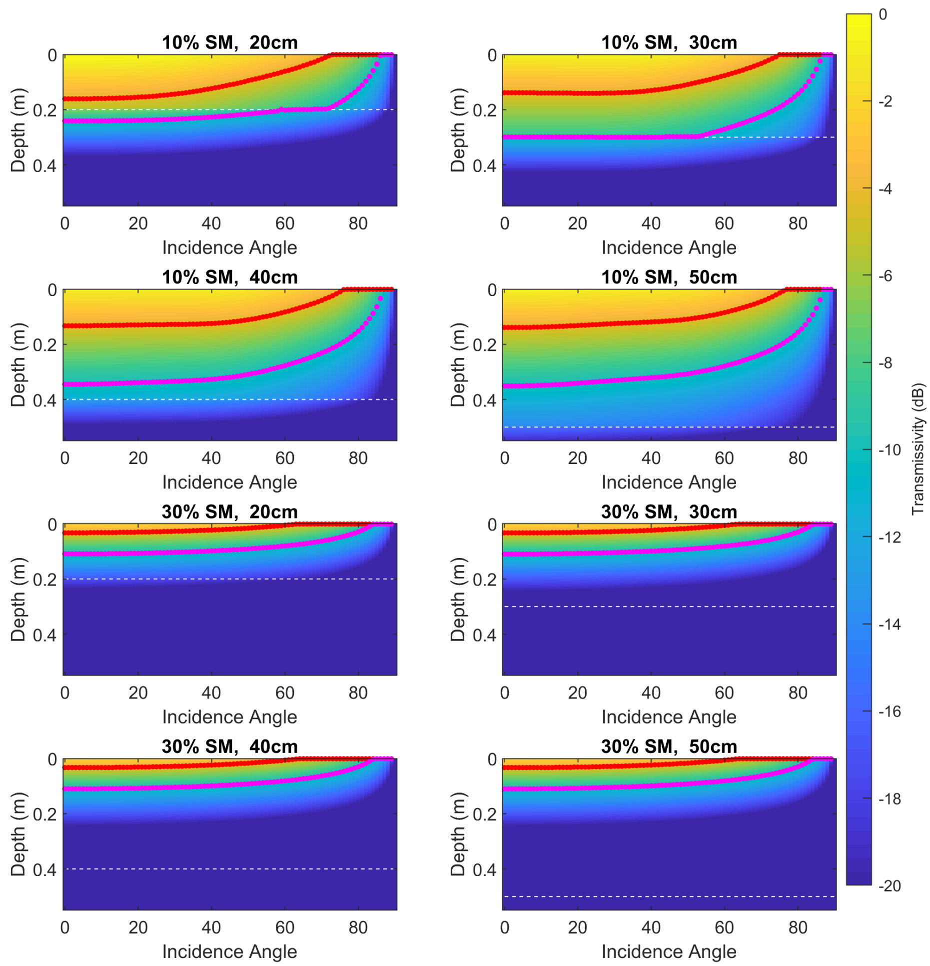

Figure 2.7

Incidence angle sweep of 4 two-layer profiles at 370 MHz. The white lines represent the location of the second layer. The red line represent the penetration depth of the configuration, and the magenta line depicts where the transmittance reaches 10% of its original energy. The upper slab SM is 10% for the upper four subplots and 30% for the lower four subplots. The second slab SM is 50% for all subplots.

2.5.2.3 Clay Content Response to Dual Slab Configurations

Figure 2.8 depicts the difference between multiple clay content combinations and the reflectivity of a dual slab configuration at 25 % for the first and second soil slabs. The center pixel of each image in Figure 2.8 shows a value of zero in natural units ($-\infty$ in dB), and all surrounding pixels show how reflectivity differs from the configuration at the center pixel. However, the colorbar has been fixed to a range of -40 to -15 dB to show meaningful data. These values are plotted for each of the five frequencies at 137.5, 255, 370, 1575.42, and 2338.75 MHz for two distinct SM slab combinations. The top row of subplots shows a configuration of 15% SM for slab 1 and 30% for slab 2. The second row of subplots shows a configuration of 30% SM for slab 1 and 15% for slab 2.

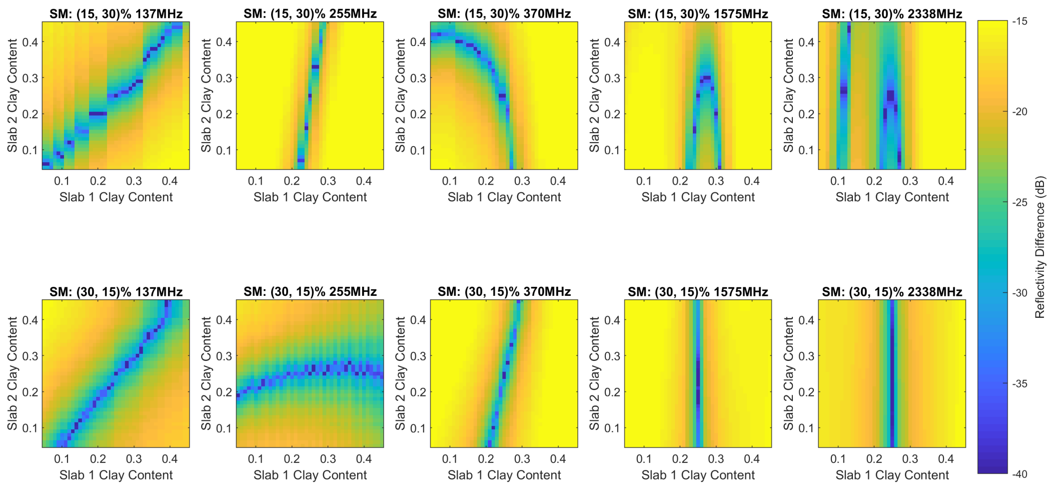

Figure 2.8

Relative difference between reflectivity measurements as a function of clay content within two soil slabs for different frequencies. The upper slab is 15 cm in height, and the second slab is semi-infinite. The top row of subplots show a configuration for SM values of 15 and 30% for slab 1 and 2, and the bottom row uses SM configurations of 30 and 15% for slab 1 and 2.

Lines of pixels in Figure 2.8 are displayed which represent largely minor differences in reflectivity values (< -35dB.) In most cases, these largely similar reflectivity values can be created by simultaneously varying both slab 1 and slab 2's clay content. However, for higher frequencies and higher SM content, the reflectivity measurements will be insensitive to the second slab. This behavior is exhibited in the two lower-right subplots for surface SM of 30% and frequency values of 1575 and 2338 MHz. It can be seen that these lines are all highly dependent on frequency, SM, and clay content.

In general, one can expect higher reflectivity differences for lower SM values due to the dominance of the SM parameters contributions on the dielectric constant. Beyond this observation, simple relationships between reflectivity and clay content are difficult to quantify for the Mironov model. This is because increasing clay content will generally lower the soil dielectric contrast and increase its loss factor. The joint effects of SM and clay are non-linear, and this behavior produces the non-linear lines of pixels below −35 dB.

2.5.3 Arbitrary Profile

Figure 2.9 depicts nine different SM profiles which vary as a function of depth. The leftmost column of subplots (Figure 2.9a, d, and g) depicts a linear, wetting SM profile. The middle column of subplots (Figure 2.9b, e, and h) depicts a linear, drying SM profile. The rightmost column of subplots (Figure 2.9c, f, and i) depicts a second-order polynomial curve for a SM profile fit. Figure 2.9i displays the upper and lower SM boundaries as discussed in Section 2.4.3. Each subplot indicates the polynomial coefficients used to create the depth-dependent SM profile using Eq. 2.8.

From these SM profiles, we calculate the elementary reflection coefficients between dielectric boundary layers in the subsurface of the SM profile in Figure 2.10. The primary driver of elementary reflection coefficients is the difference, or contrast, between two adjacent dielectric slabs. Because of the high level of discretization used in this study (a new slab every millimeter), the magnitude square of the elementary reflection coefficient values is shown in decibels for easier visualization

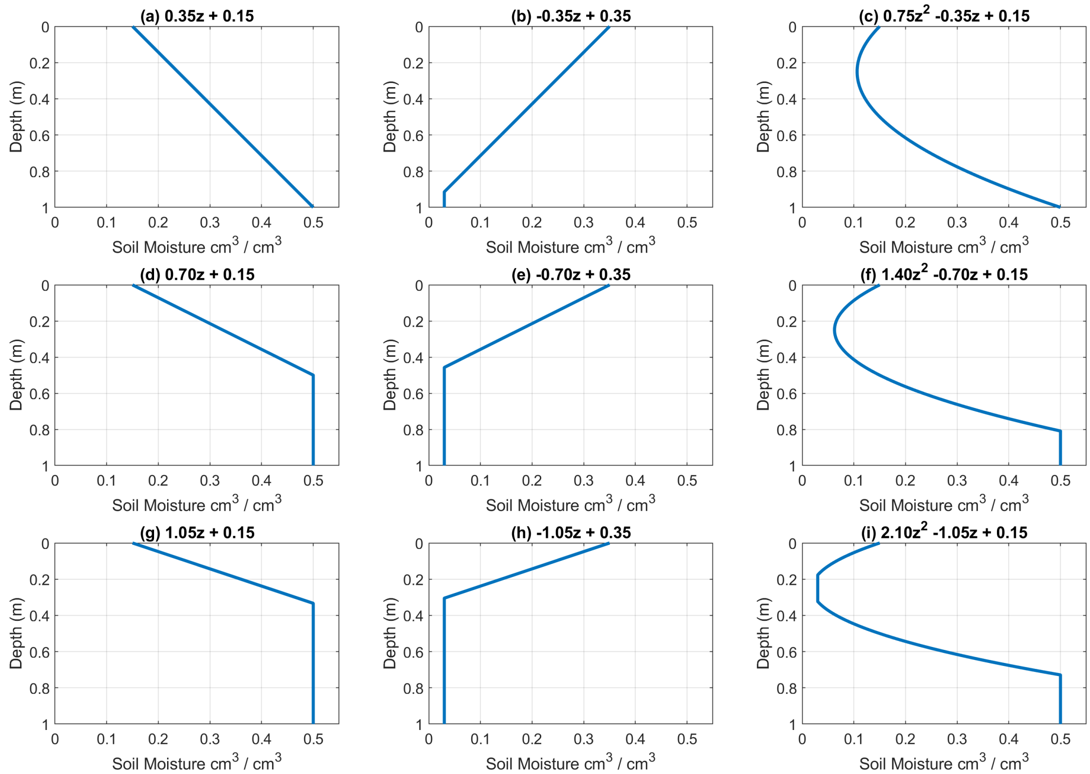

Figure 2.9

Example soil moisture profiles represented by polynomial-based equations indicated by the title of each subplot. Profiles a, d, g represent a positive, linear soil moisture profile. Profiles b, e, h represent a negative, linear soil moisture profile. Profiles c, f, i represent a second-order polynomial fit.

at low dielectric contrast. Whenever minimal dielectric contrast is present (i.e., adjacent dielectric slabs possess nearly the same dielectric constant value), the elementary reflection coefficient approaches zero. We see that in all cases, the elementary reflection coefficient value is greater for areas of lower SM content and is lower for areas of higher SM content. With the shape of these elementary reflection coefficients depicted, we now observe how the intermediate solution for the total reflection coefficient of the entire SM profile is determined.

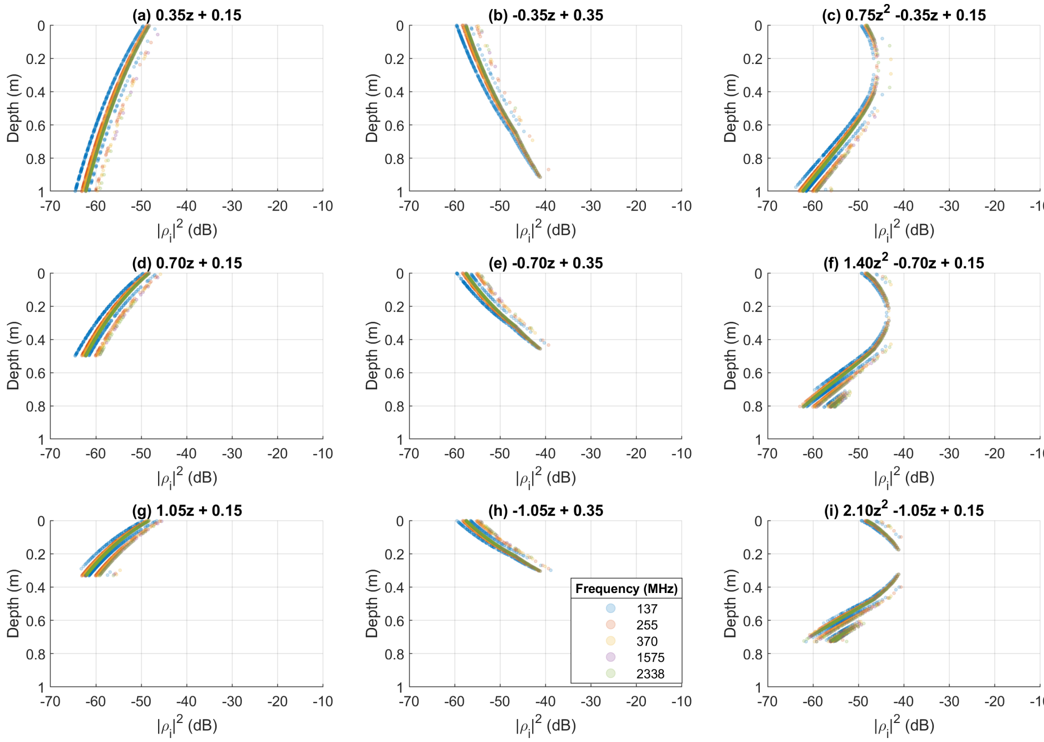

Figure 2.10

Elementary reflection coefficient in the subsurface of the soil moisture profiles of Figure 2.9. Each subplot shares a common legend indicating the frequency of each reflection coefficient. Contributions from the air-surface interface are not depicted.

In Figure 2.11, we show the subsurface, intermediate reflection coefficients at each interface for each profile in Figure 2.9. As discussed in Section 2.3 in the description of Eq. 4.26, the reflection coefficient is initialized from the bottom of the profile with the value of the elementary reflection coefficient, and the joint reflection and propagation effects are determined in order to calculate the intermediate reflection coefficient at the i^{th} interface as it ascends towards the surface of the profile. Our most general observations can be made with Figure 2.11a. For the lowest frequencies at 137, 255, and 370 MHz, the coherency of the signal is clearly depicted. The coherent nature is generally suppressed in the wetting SM profiles, while the coherency can be clearly visualized in the drying profiles. This is likely due to the overall lower SM content of the drying profiles. For all cases of higher frequency signals at 1575 and 2338 MHz, the reflection coefficient varies greatly, but generally follows the same path towards the surface as the lower frequency values. From these results, it is expected that at higher discretization levels, these higher frequency values will show smoother variations. As is expected, the reflection coefficient for lower frequencies tends to have a higher value than its high frequency counterparts.

Viewing each column of subplots in Figure 2.9, we observe that the SM profile increases as a function of depth more rapidly from subplot to subplot. This in turn produces higher dielectric contrast and higher values of subsurface reflection coefficient values in Figure 2.11. Thus, the total observed reflection coefficient seen by a SoOp-R system which seeks to resolve RZSM will be most largely affected by the rate at which SM changes with respect to depth in a profile.

As noted previously, we observe an area of no change in SM in Figure 2.9i. This same depth location produces an interesting phenomenon in the intermediate reflection coefficient of Figure 2.11i. Once the reflection coefficient reaches this portion, the value begins to degrade as it rises towards the surface. This is explained by the two processes which govern the reflection coefficient estimation: propagation and reflections. When there is no change in dielectric constant, no reflections will occur. Thus, each frequency observes an attenuated loss in reflection coefficient value due to propagation loss, with the greatest loss occurring with higher frequencies. Once the reflection coefficient calculation observes non-zero elementary reflection coefficients, the dielectric discontinuities will contribute to reflections observed by the SoOp-R system.

Figure 2.10 also visualizes the non-linear losses accrued by the reflected energy within the profile. Comparing Figure 2.10a to Figure 2.10b, we see that as the lower frequency reflectivity values approach the surface in Figure 2.10a, the reflectivity increases and contributes to the overall observed reflectivity at the surface. For Figure 2.10b, the reflectivity value decreases as it approaches the surface due to the drying SM profile. For this subplot, even the lower frequencies are more easily altered by propagation processes which contribute to the oscillatory behavior across the calculated reflectivity values. However, comparing Figure 2.10b to Figure 2.10e, we observe that these reflection coefficient values are less susceptible to the oscillatory behavior. This is due to the larger dielectric contrast which allows for contributions arising from reflection processes to become more dominant across each layer.

This simulation, overall, shows the importance of dielectric contrast. As the previous simulations have shown, different frequencies are capable of observing differences in SoOp-R measurements due to differences in both the coherence of the reflection coefficient as well as a given frequency's tolerance to propagation losses as determined by a frequency's dielectric loss properties. If greater dielectric contrast between layers is observed, there will be more opportunity for the reflected signal's energy to be reflected towards the receiver. Conversely, if the SM profile changes slowly, fewer reflections will be produced, and the effects of propagation loss will be more strongly pronounced.

2.6 Discussion

The SCoBi model used in these simulations is highly modular and designed to examine a wide variety of SoOp-R scenarios. By allowing the user to model their own SM profile, vegetation canopies, antenna radiation patterns, and bistatic configuration, it is our intent to provide a simple, configurable M&S package to model and design SoOp-R experiments using fundamental

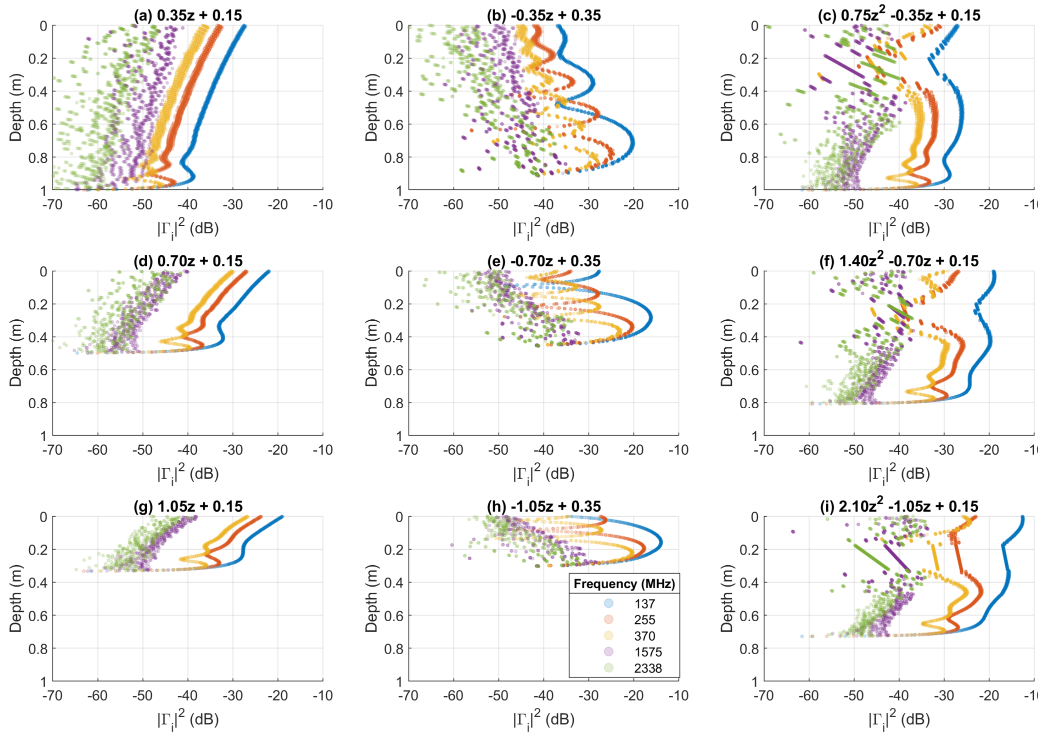

Figure 2.11

Intermediate reflection coefficient solution in the subsurface of the soil moisture profiles of Figure 2.9. The reflection coefficient is initialized by the bottom-most elementary reflection coefficient and determined as the signal travels upward through the profile. Each subplot shares a common legend indicating the frequency of each reflection coefficient. Contributions from the air-surface interface are not depicted.

microwave theory based on Maxwell's equations. Interested parties are encouraged to use the codes available in this package to adapt to their M&S needs. The SCoBi multilayer module is currently being used in modeling and simulations in support of the SNOOPI experiment [45], RZSM inversion research being conducted at Purdue University [10], and farmland SM remote sensing at Mississippi State University.

The version of SCoBi used in this study is designed for low-altitude applications. A SCoBi update is in development in support of future SNOOPI measurements which includes more comprehensive tools that are appropriate for spaceborne applications. Specifically, a future release of SCoBi is in development which will utilize a grid of several flat-earth approximations superimposed over a Digital Elevation Map (DEM) to calculate the total received electric field emerging from each facet. Since the absolute phase of the signal is preserved, the total topographic effects will be considered a superposition of each grid along the DEM. This expected update will enable analysis with respect to topographical relief, spherical Earth surface scattering, and incoherent contributions from surface roughness effects. While coherency can be reasonably assumed under smooth surface assumptions at low altitudes, topographic relief has been shown to be a significant factor in GNSS-R applications for spaceborne applications [33, 88]. Thus, the results of these simulations must be carefully considered for spaceborne applications where incoherent contributions from factors such as topography may be dominant. Future studies which discuss the signatures and dynamic range of signal contributions from topography, surface roughness, and vegetation would be highly beneficial to the literature for understanding the utility of the different available frequencies.

In addition to surface roughness effects, rough layering between dielectric slabs within the profile have not been included in this study. This methodology has been incorporated into the study of radar backscatter previously. Given a two-layer model, it has been shown that the subsurface layer roughness can have a measurable impact on the overall reflected energy [37, 110]. It is suggested that subsurface layer roughness should be used when a significant shift in soil texture composition occurs [64]. However, the SM profiles in this paper assume a homogenous soil texture composition in nearly all simulations. If prior information is known about uneven dielectric variations within the profile, we note that such subsurface layer roughness values should be considered.

As discussed in Section 2.5, the measured reflectivity is a function of both wave propagation effects and reflections along dielectric discontinuities. As shown in Figure 2.4, the relative permittivity for the examined frequency region is largely identical, and the loss factor is largely frequency insensitive above 1000 MHz. Because of this frequency insensitivity, the dielectric discontinuities across the vertical SM gradient will be the same, and this will produce nearly identical values of reflections at each boundary layer. However, because of the frequency dependence of the propagation effects, different frequencies will observe different responses to a SM gradient based on reflections towards the receiver as shown in Figure 2.11. For this reason, we conclude that multiple frequencies can leverage the differences observed in the measured reflection coefficients to determine subsurface SM values.

Our simulations exhibit the behavior of SoOp measurements given a SM profile represented by a single slab, two slabs, and an arbitrary number of slabs. By following this process of increased layering, we can clearly visualize that the dielectric boundaries produce identical reflections given a single air-surface interface as shown in Figure 2.3. When looking at two dielectric slabs, we can observe that the position of the dielectric slabs within the profile will cause the SoOp-R observation to become frequency dependent. From these two simulations, we can obtain all of the components to rationalize the behavior of the SoOp-R response to complicated profiles represented by n-degree polynomials and, therefore, any SM model based on the profile's dielectric properties and layering structure. While this paper presented several simple representations of the SM vertical profile, this research can be further explored by examining the feasibility of SoOp-

R-enabled SM inversion using hydrologically-based SM models. Inclusion of parameters such as hydraulic potential, evapotransporation modeling, hydraulic conductivity, and soil pressure head can assuredly be beneficial for the creation of SM data products, however, such profile-specific and hydrology-focused simulations are beyond the scope of this paper. Additionally, this simulation did not account for surface roughness or vegetation effects, and this was done in order to provide a focused insight into the simplified case of SoOp-R reflections from a bare soil profile. Future studies could further this research by characterizing the impact of various vegetation structures and surface roughness parameters on the measured SoOp-R signal.

2.7 Summary and Conclusion

This work presents the multilayer module of the SCoBi model and simulator. The SCoBi multilayer module enables the modeling and simulation of user-defined SM profiles using well-established, fundamental electromagnetic theory. The inclusion of the multilayer module in the SCoBi framework is designed to allow users to conduct comprehensive SoOp-R simulations of RZSM regardless of their scientific background. When paired with SCoBi's other modules, SCoBi can enable multifaceted analysis of SoOp-R simulations with respect to surface SM, RZSM, surface roughness effects, vegetation, bistatic geometry, and many other modeling considerations for land remote sensing. The details of the model as well as the simulator functionality are described.

This paper presents an analysis of the multifrequency SoOp-R response to RZSM represented by multilayer dielectric slabs with variable depth, SM content, and discretization. The analysis uses the recently-developed Mironov model to represent the complex SM dielectric constant within each layer. We provide the following general observations:

From our simulations, we observe that the dielectric constant value of SM is largely frequency independent for the examined frequency range of this study. While this study uses the Mironov model primarily to determine the dielectric constant value of SM, this phenomenon is observed in the Dobson-Peplinksi SM dielectric model as well. We observe that the coherence of these signals can be leveraged in order to observe changes in subsurface SM.

Penetration depth is briefly examined for a simple, two-dielectric slab simulation series. While penetration depth is often cited in literature to indicate a general area at which SM may be retrieved, this paper discusses an example method of determining a profile-specific sensing depth by moving a dielectric slab down a profile and observing the position where the reflectivity is less than the SoOp-R system's confidence threshold for reflectivity measurements. If a SoOp-R system can confidently measure reflectivity to a desired precision level, the depth at which SM may be sensed can be much greater than the suggested penetration depth.

The effect of variable clay content within the Mironov soil dielectric model is examined. As the Mironov model is a function of only frequency, clay content, and SM, the clay content of the Mironov model is the only parameter available to describe soil composition. When this clay content is varied for two soil slabs, we find that many combinations of clay content can result in similar resulting reflectivity values. This suggests the importance of soil texture classification in order to minimize errors induced by uncertainty in soil texture.

We also examine the effects of profiles which vary in SM as a function of depth. It can be observed that the dielectric contrast between layers is the driving force for responses to subsurface SM. If a portion of the profile features no variation in dielectric constant, only propagation loss occurs, and no energy will be reflected towards the receiver in order to be sensed. The lower frequencies can take advantage of higher penetration and sense dielectric contrast deeper into the soil whereas higher frequencies have a limited response over shallow regions of the soil. This further emphasizes the importance of leveraging more than one frequency source to retrieve subsurface SM.

CHAPTER III

CRAMER-RAO BOUND FOR GROUND-BASED MULTILAYER INVERSION

D.R. Boyd, A.C. Gurbuz, M. Kurum, J. Garrison, B. Nold, R. Bindlish, J. Piepmeier, M. Vega, "Cramer-Rao Lower Bound for SoOp-R-Based Root-Zone Soil Moisture Remote Sensing," *IEEE Journal of Selected Topics in Applied Earth Observation and Remote Sensing*, vol. 13, pp.6101–6114, 2020. doi:10.1109/JSTARS.2020.3029158. © 2020 IEEE.

3.1 Abstract

SoOp Reflectometry (SoOp-R) is a maturing field for geophysical remote sensing as evidenced by the growing number of airborne and spaceborne experiments. As this approach receives more attention, it is worth analyzing SoOp-R's capabilities to retrieve subsurface soil moisture (SM) by leveraging communication and navigation satellite transmitters. In this research, the Cramer-Rao lower bound (CRLB) is used to identify the effects of variable SoOp-R parameters on the best achievable estimation error for root-zone soil moisture (RZSM). This study investigates the use of multiple frequency, polarization, and incidence angle measurement configurations on a two-layered dielectric profile. The results also detail the effects of variable SM conditions on the capability of SoOp-R systems to predict subsurface SM. The most prevalent observation is the importance of

using at least two frequencies to limit uncertainties from subsurface SM estimates. If at least two frequencies are used, the CRLB of a profile is retrievable within the root-zone depending on the surface SM content as well as the number of independent measurements of the profile. For a depth of 30 cm, it is observed that a CRLB corresponding to 4% RZSM estimation accuracy is achievable with as few as 2 dual-frequency-based SoOp-R measurements. For this depth, increasing number of measurements provided by polarization and incidence angle allow for sensing of increasingly wet SM profile structures. This study, overall, details a methodology by which SoOp-R receiver system can be designed to achieve a desired CRLB using a trade-off study between the available measurements and SM profile.

3.2 Introduction

SoOp-R within remote sensing refers to the process of leveraging available transmitter sources to perform remote sensing of a geophysical parameter such as ocean surface roughness, sea ice detection, SM, vegetation biomass, or snow water equivalent [51, 102, 133]. The field has experienced many successful ocean-based applications, experiments, and missions from a dedicated research community since the late 1990s [46, 72, 102, 115]. This success has since inspired land-based remote sensing applications for SM and snow water equivalent [23, 24, 48, 61, 62, 94, 130].

One of the most prominent benefits of the signals of opportunity (SoOp) method is its capability to leverage the available frequency sources from non-cooperative, anthropogenic transmitters to perform measurements. This is achievable in a cost-efficient manner when compared to traditional radar developments by removing the size, weight, and power (SWaP) constraints required for an onboard transmitter. Thus, there is great interest in applying the available frequency sources for ground-based, airborne, and spaceborne applications for remote sensing.

RZSM is a highly sought geophysical observable due to its wide impact across many fields of Earth science such as hydrology, weather forecasting, and crop-yield estimation [3]. RZSM, as the name suggests, is defined as the water content available to a given vegetation's root-uptake system within a SM profile. Since the root-zone of a given vegetation structure can vary based on root length, the root-zone typically refers to the upper 1 meter of a SM profile when discussed irrespective of a particular plant. RZSM data products are a critical resource for hydrological modeling [4].

Within the remote sensing community, remote sensing via radar backscatter is currently the most studied field for determining RZSM. Radar backscatter's sensitivity to surface SM has been explored as early as the 1970s [118]. This field has advanced to include successful airborne missions using synthetic aperture radar (SAR)-based P-band remote sensing systems to provide RZSM products [19, 109]. Studies using radar backscatter at this frequency have detailed the effect of multilayer backscatter for the purpose of RZSM inversion [63].

Recent experiments and simulation studies suggest that multi-frequency observations should be used in resolving RZSM from SoOp-R microwave remote sensing techniques [11]. Some of the most commonly referenced SoOp sources include the Orbcomm communication constellation centered at 137 MHz, the United States Navy's Ultra-High Frequency Follow-On system centered at 255 MHz and the Mobile User Objective System (MUOS) centered at 370 MHz, global navigation satellite system (GNSS) sources which feature publicly available codes at 1575.42 MHz, and the XM Satellite Radio constellation at 2338 MHz.

While simulations have clearly shown that SoOp-R measurements observe the effects of RZSM when simulating multilayered dielectric structures [8], it is helpful to determine the estimation accuracy of differing SoOp-R configurations on RZSM profiles. Such studies can help design future SoOp-R experiments as well as provide insight on the potential uncertainty embedded within inversion algorithms. To the author's knowledge, no such research has been performed for the use of forward-reflected signals for the purpose of RZSM estimation.

A common technique to compare the performance of any unbiased estimator is the use of the CRLB [58]. The CRLB is a popular statistical signal processing technique which expresses a lower bound on the estimation variance providing the best benchmark we can ever expect to achieve with an unbiased estimator. An estimator achieving CRLB is efficient, and it is the minimum variance unbiased estimator for a given model. The CRLB is useful in parameter estimation for remote sensing as it provides a robust metric for characterizing different measurement configurations and its impact on an unknown parameter [30, 96, 101]. Application of the CRLB to the RZSM problem allows us to determine the estimation bound of any estimator given the same modeling and simulation environment.

This paper seeks to determine the estimation accuracy for RZSM for a number of simple SM profile configurations and bistatic SoOp-R scenarios. The simulations consist of many two-slab configurations for RZSM estimation in which the combination of frequencies, incidence angles, and polarizations of signals are considered to achieve the most optimal estimation accuracy possible. The modeling and simulation environment as well as the CRLB calculations are presented in Section 3.3. The simulations are presented in Section 3.4 and are discussed in Section 3.5. Our concluding remarks on the study are presented in Section 3.6.

3.3 Modeling and Theory

This section presents the theory and modeling for the CRLB study used by this paper. Section 3.3.1 details the model used to produce the SoOp-R measurements as a function of both ground and system variables. Section 3.3.2 presents our implementation of the CRLB for this paper. All data presented is simulated.

3.3.1 SoOp-R and Environment Modeling

The model used to simulate the bistatic SoOp-R environment and resulting measurements is the SoOp coherent bistatic scattering model (SCoBi) model v1.0.3 [38, 65]. The SCoBi model is a fully polarimetric simulation tool that allows for comprehensive modeling of the ground reflecting surface, geometry, antenna configurations, and cross-channel noise processes. Since the model is based on analytical wave theory, the amplitude and phase information of the coherent signal is preserved through the simulation process. For bare soils, the reflection coefficient is calculated through an iterative process by which the propagation and reflection processes of a signal incident upon a series of dielectric slabs is calculated directly from Maxwell's equations. The SCoBi model is capable of modeling many features such as multiple SM dielectric representations, vegetation structures, and surface roughness effects.

While the received signals are generally composed of contributions from vegetation, topography, surface roughness, soil type, and water bodies under a typical spaceborne bistatic scenario, we assume a dominantly specular signal over a bare surface SM profile for the purposes of this study. The multipath reflection coefficient $\underline{\Gamma}_{coh}$ is calculated from the following relation.

$$\underline{\Gamma}_{coh} = \underline{\underline{g}}_r(\hat{\boldsymbol{o}}_s^+) \cdot \underline{\underline{u}}_{s\rightarrow r}(\hat{\boldsymbol{o}}_s^+) \cdot \\ \underline{\underline{r}}_s(\hat{\boldsymbol{o}}_s^+, \hat{\boldsymbol{i}}_s^-) \cdot \underline{\underline{u}}_{t\rightarrow s}(\hat{\boldsymbol{i}}_s^-) \cdot \underline{\underline{g}}_t(\hat{\boldsymbol{i}}_s^-) \cdot \underline{e}_t \tag{3.1}$$

where i and o describe the incoming and outgoing directions of the wave propagation, $\underline{\underline{g}}_r$ and $\underline{\underline{g}}_t$ are the receiver gain and transmitter gain respectively, $\underline{\underline{u}}_{s\rightarrow r}$ and $\underline{\underline{u}}_{t\rightarrow s}$ represent the polarization basis transformation between specular-point-to-receiver and transmitter-to-specular-point respectively, $\underline{\underline{r}}_s$ is the specular reflection matrix, and $\underline{e}_t$ is the nominal polarization state. More details on the derivation of the reflection coefficient and its constituent parameters can be found in [65].

This problem assumes specular-dominant contributions based on the system geometry and previous research findings [41]. For this study, we assume a fixed altitude and azimuth. Because of the flat, homogeneous slabs that are used in this study, many parameters will have negligible effect on the received signal. Under a specular reflection assumption where the surface roughness is within the Rayleigh scattering regime, the contributing area of the spatial footprint is restricted to the first Fresnel zone [133], which varies as a function of frequency, incidence angle, and platform altitude. However, because the reflecting surface is assumed to be semi-infinite and homogeneous within each layer, factors such as spatial resolution and azimuth direction can be ignored.

A simplified depiction of the modeling and simulation environment for this paper's simulations is shown in Figure 3.1. The receiver is pointed directly towards the specular point, and no antenna losses are simulated. The primary system variables considered are transmitter frequency, transmitter incidence angle (equal to the surface scattering angle for bare soils), and receiver polarization. While some communication satellite systems use left-hand circular polarization (L), all transmitter polarizations in this study are fixed at right-hand circular polarization (R) in order to more easily describe the co- and cross-polarization relationships with the CRLB.

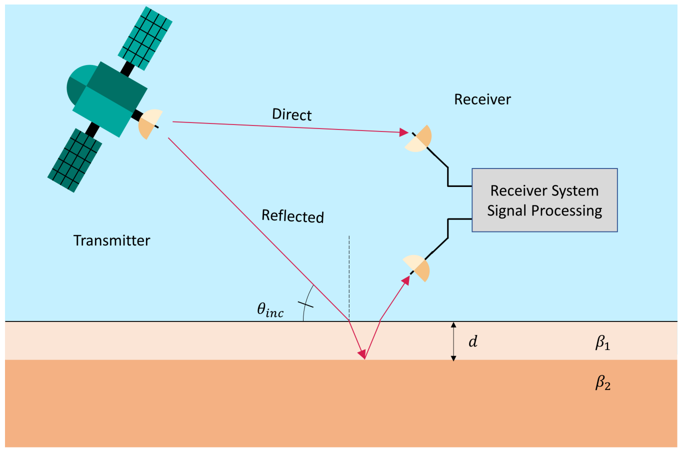

Figure 3.1

Simplified geometry of this paper's modeling and simulation environment. The unknown SM variables are designated as β_1 and β_2 for the first and second SM slabs. No surface roughness is assumed. An initial slab is assumed to contain constant SM from the surface until the dielectric discontinuity at location d. The SM content (β_2) at depth d is considered to be the root-zone for this study. © IEEE 2020.

For simplicity and ease of understanding, the SM profile is represented by two layers: a surface SM value extending from the air-surface interface to the next dielectric discontinuity and a second slab extending downward infinitely across the half-space. The dielectric value of these two slabs is calculated using the Mironov dielectric model [78]. This model is parameterized by volumetric SM and soil clay content. The latter of which is assumed to be 31% for this study. As previously mentioned, surface roughness is not considered.

The general geometry in this simulation study, while capable of being modeled in SCoBi, is simplified to constant values. SCoBi is capable of modeling antenna beam patterns as well as losses from polarization mismatch and antenna cross-talk. However, full consideration of the bistatic geometry between the transmitter, receiver, and specular point should be considered when implementing such an analysis. Since such a study would require fixed points of reference relative to the location of transmitters, antenna beam direction (including both incidence and azimuth angle), and the physical location of the receiver, we choose to assume these values are negligible so that the results are generalized for SoOp-R applications.

Soil texture is an important parameter in establishing the dielectric of soil because soil texture can change the distribution of water content within a soil layer. Clay content, the configurable parameter for the Mironov soil dielectric model, changes the dielectric of soil nonlinearly. However, because soil texture does not change significantly over time like SM, it is common to assume that it is static as we do in this study.

3.3.2 Cramer-Rao Lower Bound Model

The CRLB is considered to be one of the simplest methods for placing a lower bound on the variance of any unbiased estimator. It also provides a way for determining the minimum variance unbiased estimator. In the case of a deterministic modeling and simulation scenario, the CRLB presents the ultimate performance of an unknown parameter estimator for the given set of specific model inputs. Although CRLB defines the performance bound, the maximum likelihood estimator (MLE) is an asymptotically efficient attaining CRLB.

Since all of our information about estimating the RZSM parameter is embodied in the observed measurements and the underlying probability distribution function (PDF) for that data, the CRLB that defines the estimation accuracy also depends on the PDF. We use the SCoBi model to simulate the coherent reflection coefficient measurements.

We first discuss the parameterization of our forward model and simulation environment for the CRLB calculation. After having fixed certain parameters within the SCoBi model, the remaining controllable variables are described. The controllable parameters will be contained in the vector $\boldsymbol{x} = [f, \theta_{inc}, q]$ where f is the frequency of the transmitter and receiver, θ_{inc} is the incidence angle of the signal at the air-surface boundary, and q is the polarization of the receiver antenna. The unknown parameter vector representing the SM of the upper and lower layers is given by $\boldsymbol{\beta} = [\beta_1,\ \beta_2]$. The output reflection coefficient $\underline{\Gamma}_{coh}$ from (3.1) is computed using the forward SCoBi model $f_{SCoBi}(\boldsymbol{x}; \boldsymbol{\beta})$. The output measurement y is the sum of our model output and measurement noise n.

$$y = f_{SCoBi}(\boldsymbol{x}; \boldsymbol{\beta}) + n \tag{3.2}$$

The measurement noise in (3.2) is assumed to be a zero-mean, white Gaussian process for the reflection coefficient with a common variance of σ^2. As the reflection coefficient is a complex number, the noise power is assumed to be distributed evenly across the real and imaginary components of the signal. Selecting a noise term for the reflection coefficient should adequately reflect typical noise values observed by SoOp-R systems.

The SCoBi model output buried in Gaussian noise is treated as a multivariate probability distribution function whose inputs are defined by the measurement vector $\boldsymbol{y}$, system input vector $\boldsymbol{x}$, and unknown parameter vector $\boldsymbol{\beta}$ as defined in (3.3).

$$p(\boldsymbol{y};\boldsymbol{x},\boldsymbol{\beta}) = \mathcal{N}(f_{SCoBi}(\boldsymbol{x},\boldsymbol{\beta}),\sigma^2\boldsymbol{I}) \tag{3.3}$$

Under these conditions, the CRLB for parameter $\boldsymbol{\beta_i}$ is found as the $[i,i]$-th element of the inverse of a matrix

$$\mathrm{var}(\hat{\beta}) \geq \left[\boldsymbol{F^{-1}}(\boldsymbol{\beta})\right]_{ii} = CRLB(\boldsymbol{\beta_i}) \tag{3.4}$$

where $\boldsymbol{F(\beta)}$ is the $\alpha \times \alpha$ Fisher information matrix that is defined by

$$[\boldsymbol{F(\beta)}]_{ij} = -E\left[\frac{\partial^2 \ln p(\boldsymbol{x};\boldsymbol{\beta})}{\partial\beta_i\partial\beta_j}\right] \tag{3.5}$$

for $i,j = 1,2,\ldots,\alpha$ where α is the total number of unknown parameters [58]. In our case, representing the unknown RZSM with $\boldsymbol{\beta} = [\beta_1,\ \beta_2]$ for upper and lower layers, $\alpha = 2$ and the matrix $\boldsymbol{F(\beta)}$ is 2×2. However, the presented CRLB model is able to handle any given number of unknown parameter settings.

In addition, since our model is a complex, multivariate Gaussian [59, 108], calculation of the Fisher information matrix can further be simplified using

$$\boldsymbol{F_{ij}} = \frac{2}{\sigma^2}\Re\left(\left[\frac{\partial f_{SCoBi}(\boldsymbol{x},\boldsymbol{\beta})}{\partial\beta_i}\right]^H\left[\frac{\partial f_{SCoBi}(\boldsymbol{x},\boldsymbol{\beta})}{\partial\beta_j}\right]\right). \tag{3.6}$$

3.4 Simulation Study

The following study presents multiple simulations which examine the resultant CRLB when the input for the modeling and simulation environment is changed. Specifically, the five main variables of interest are frequency, incidence angle, polarization, SM content, and SM slab position. As some simulations require slightly different environments to illustrate the effect of certain inputs, the methodology for each simulation is presented alongside the associated results. Working under the assumption that the square root of the lower-bound is directly comparable to SM retrieval accuracy constraints, all results will depict the $\sqrt{CRLB}$. For all figures depicting the $\sqrt{CRLB}$ along the y-axis, each subplot shows the value as a percentage instead of natural units.

All simulations share certain common features. The $\sqrt{CRLB}$ is calculated using measurements from the combination of all available inputs (e.g., a simulation at 3 frequencies, 2 angles, and 2 polarizations will produce 12 measurements to determine the $\sqrt{CRLB}$.) All measurements use a common noise variance σ^2 based on a reflectivity noise floor of -34 dB. This value is chosen based on the distribution of 2017 and 2018 CYGNSS reflectivity observations over land [42]. While it is likely that different communication systems will observe different noise distributions, a common noise variance for all frequencies will help focus the simulations on a generalized characterization of the impact of the receiver system variables. Nearly all measurements are performed using a SM profile consisting of two slabs where the first slab extends from the air-surface interface to a depth d in centimeters. When the 5 commonly available SoOp-R transmitters at 137.5, 255, 370, 1575.42, and 2338 MHz are used as variable parameters in subsequent figures, these frequencies are denoted as a, b, c, d, and e in order to achieve efficient spacing within the figures.

The following study intends to show the reader the benefits of using different combinations of frequencies, polarizations, and incidence angles for different SM values and RZSM depth positions. Similar to the concept of dropout in neural network regularization, this study begins with a large number of measurements and removes parameters that are unnecessary to obtain the desired RZSM retrieval estimation accuracy. The number of parameters used is larger than what can be expected from most experimental applications. However, by visualizing ”smooth” $\sqrt{CRLB}$ gradients from the use of a large number of measurements, it is our intention to more easily visualize the influences of frequency, polarization, and incidence angle to the reader by removing these parameters and observing their impact on the $\sqrt{CRLB}$ calculation.

3.4.1 CRLB as Function of Depth and Frequency

In this section, the relationship between the $\sqrt{CRLB}$, frequency, and sensing depth is examined. In the context of this paper, the sensing depth refers to positions within the root-zone where the second slab's SM content (β_2) can be sensed within a desired degree of error. A target $\sqrt{CRLB}$ that is less than or equal to 4% will be the primary focus since this is a commonly targeted goal for surface SM estimation.

While penetration depth is a good metric for establishing a general depth where signal contributions can be sensed, the most commonly used penetration depth formula assumes a single SM value for the entire profile and, therefore, cannot account for the reflection properties of multilayer dielectric structures. For this reason, the $\sqrt{CRLB}$ will be used directly to determine depths where RZSM can be sensed with a desired 4% accuracy.

To establish a reasonable depth for RZSM estimation with this paper's system configuration, two initial cases are presented. First, a scenario where 120 SoOp-R measurements are used to determine the $\sqrt{CRLB}$. For the second scenario, we then restrict the measurements to only five values. These two simulations are used to illustrate the range of potential RZSM depths d where a $\sqrt{CRLB}$ estimation accuracy of 4% can be achieved. While it is unlikely to obtain 120 measurements over short temporal spans in field applications, this initial number of parameters allows us to visualize the $\sqrt{CRLB}$ while mitigating anomalies that stem from an undesirable combination of measurements.

The $\sqrt{CRLB}$ is calculated across the upper 1 meter of an example SM profile. For a two slab profile, the second slab is lowered within the profile to examine the effects that the location of the second slab (i.e., the RZSM slab) induce on the $\sqrt{CRLB}$. Because there are only two layers, this can also be described as moving the position of the single dielectric discontinuity within the profile deeper into the soil. Two configurations are used in this study. One configuration assumes 120 reflection coefficient measurements from the combination of values resulting from the 5 frequencies, 6 incidence angles equally spaced from 20° to 70°, and the 4 receiver polarizations (X, Y, L, and R.) The second configuration assumes 5 measurements collected at the 5 available frequencies with each measurement occurring at L-polarization and a 20° incidence angle.

Figure 3.2 presents the resultant $\sqrt{CRLB}$ values for the RZSM (β_2) estimates. The x-axis indicates the location of the dielectric discontinuity within the profile. Each subplot within the figure indicates the SM content of the second slab (i.e., RZSM), while the different colored lines represent the SM value of the first slab (i.e., surface SM.) The upper-left and upper-right subplots within the figure indicates the first measurement configuration using 120 measurements, while the lower-left and lower-right subplots indicate the second measurement configuration of only 5 measurements.

It is immediately apparent that the depth for resolving RZSM β_2 is dependent on the SM profile and receiver configuration. An important factor for this behavior is the nature of subsurface reflection properties which are dominantly controlled by the dielectric contrast of subsurface slabs [11]. As the size of the surface SM slab increases, the waves propagating through the first slab will undergo more attenuation processes which make RZSM retrieval more difficult. If we observe a RZSM value of 20%, we find that the point at which our RZSM estimation reaches ± 4%

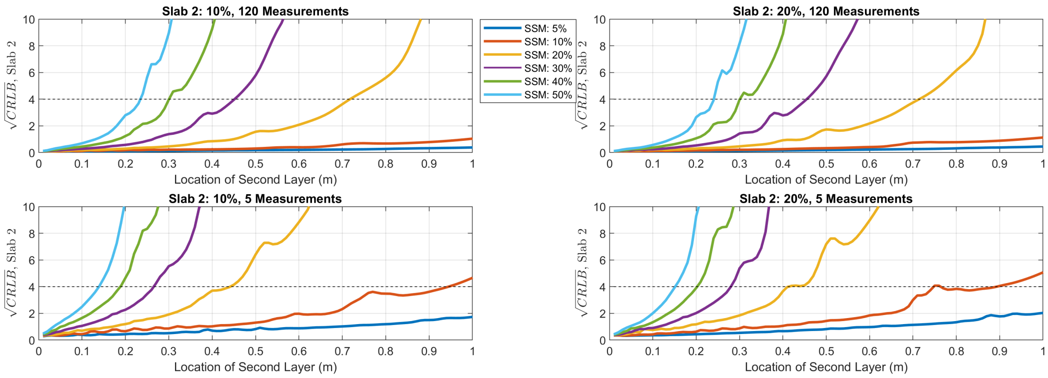

Figure 3.2

Root-zone soil moisture $\sqrt{CRLB}$ as a function of depth. The upper two subplots show the $\sqrt{CRLB}$ from the combination of five frequencies (137, 255, 370, 1575.42, and 2338 MHz), six angles (20, 30, 40, 50, 60, and 70°), and four polarizations (X, Y, L, R) producing 120 measurements. The bottom two subplots show five measurements from (137, 255, 370, 1575.42, and 2338 MHz at L-polarization and 20° incidence. © IEEE 2020.

accuracy is at 71, 45, 30, and 24 cm for surface SM values of 20, 30, 40, and 50% volumetric soil moisture (VSM). Given five measurements, this same estimation accuracy is achieved at depths of 41, 27, 20, and 15 cm for the same SM and RZSM values. This simulation, therefore, shows the potential, variable depths at which we can estimate RZSM for a specified accuracy range of ± 4%.

The $\sqrt{CRLB}$ for surface SM estimates β_1 were also calculated alongside each value for β_2, although they are not depicted. The surface SM estimates show that the surface SM $\sqrt{CRLB}$ is always lower-bounded significantly lower than the desired accuracy range of ± 4% as expected. When changing from 120 measurements to 5 measurements, the worst-case $CRLB$ changes from less than 0.4% to roughly 1%. Thus, the multi-frequency measurements are capable of resolving the surface SM regardless of the SM content or location of the dielectric discontinuity within these simulations.

Having established the effect that depth has on the $\sqrt{CRLB}$ when 5 frequencies are used for many SM profiles, we now examine the effect of frequency combinations and RZSM depth simultaneously. Figure 3.3 depicts the resultant $\sqrt{CRLB}$ for these simulations for the RZSM (β_2). The results are restricted to example SM profiles featuring relatively high SM content. The frequencies used are 137, 255, 370, 1575, and 2338 MHz which are represented by the letters a, b, c, d, and e along the x-axis of each subplot. The depth of the slab position is indicated along the y-axis. Within the simulation, the slab is moved in 1 cm increments down the SM profile. The upper-left and upper-right subplots feature a surface SM of 20% and a RZSM value of 10% and 30% respectively. The lower-left and lower-right subplots feature a surface SM of 30% and a RZSM value of 20% and 40% respectively. This is performed to visualize a consistent dielectric contrast with respect to SM value for each row of subplots. While this paper is interested in understanding depths where a 4% estimation error can reliably be obtained, the results are thresholded up to a maximum $\sqrt{CRLB}$ of 10% to provide understanding of the increasing estimation error with respect to depth, frequency combinations, and SM profile structure.

The results of Figure 3.3 show distinct changes with respect to SM content as well as the number of frequencies used. The visually striking group of pixels which exceed the $\sqrt{CRLB}$ threshold of 10% in this image are observed at frequencies of 1575 and 2338 MHz (d and e). Due to the shorter wavelengths, these signals show limited configurations where RZSM can be sensed. For example, in the upper-right subplot of Figure 3.3, the $\sqrt{CRLB}$ derived exclusively from 1575 MHz reaches high error values around 22 cm, and the 2338 MHz signal reaches high error values around 12 cm. By lowering the RZSM slab further into the profile, contributions from these depths are buried in noise.

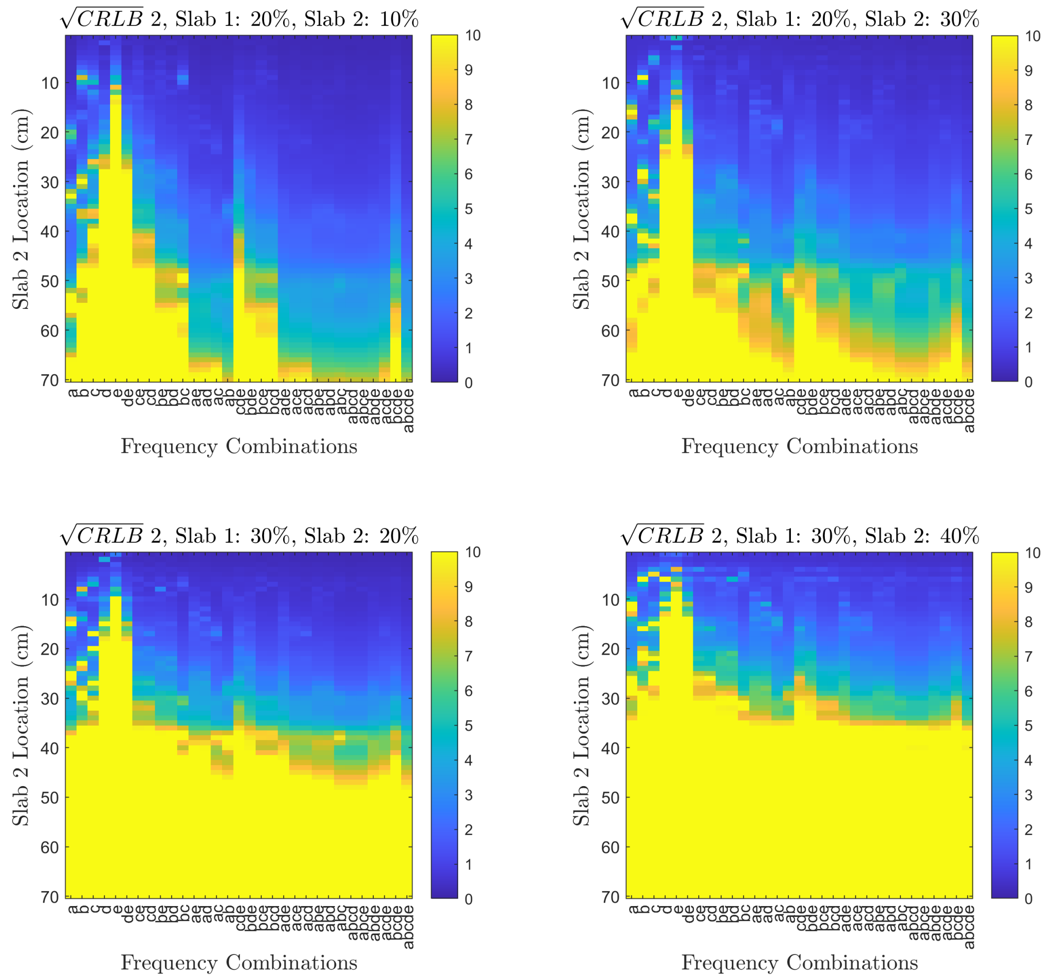

Figure 3.3

$\sqrt{CRLB}$ of RZSM as a function of depth and frequency for wet SM profiles. Frequency combinations are noted along the x-axis where a, b, c, d, and e correspond to 137, 255, 370, 1575, and 2338 MHz respectively. Each frequency samples measurements in X and Y polarization as well as at 20, 45, and 70° incidence. The location of the second slab is shown on the y-axis, and the value of the resultant $\sqrt{CRLB}$ is shown by the color bar. © IEEE 2020.

Across the range of frequency combinations along the x-axis, the $\sqrt{CRLB}$ for measurements using a surface SM value of 20% remain far below the 10% threshold up to the y-axis limit of 45 cm for most dual-frequency combinations. Whenever the surface SM is increased to 30%, only portions of the dual-frequency combinations can sense below the maximum $\sqrt{CRLB}$ threshold, and the RZSM value can be seen to alter the depth where this threshold is reached for frequency combinations. This threshold indicates an area where the signal becomes buried by our system noise and can no longer be confidently used in RZSM estimation. As visualized in the lower-left subplot, the use of multiple frequencies can allow for RZSM estimation deeper into the profile than the maximum depth of a single frequency's estimation capabilities.

There are multiple depths where the RZSM can be estimated using a single frequency when the SoOp-R signal remains above the noise floor. As mentioned previously, this is caused by frequency and depth-dependent properties of the signal's interaction with the profile. While this indicates that an estimator which can achieve a desirable $\sqrt{CRLB}$ from a single frequency might exist, this estimator is likely insufficient for handling changes in the SM gradient.

Throughout Figure 3.3, there are many instances of abrupt changes in $\sqrt{CRLB}$ along different depths. For example, a sharp increase in $\sqrt{CRLB}$ occurs at 33 cm for 137 MHz (a) and at 30 cm for 255 MHz (b) in the upper-left subplot. This occurs for two reasons. When the Jacobian matrix is calculated with respect to the unknown SM parameters, certain depths will exhibit limited change with respect to SM. Because of the coherency of the reflection coefficient, we note that this generally occurs at a point where the reflection coefficient has reached a maximum or minimum with respect to depth. Thus, there are depths where perturbing the forward model with respect to SM will observe limited change due to the frequency-dependent coherency fluctuations of the reflection coefficient. The resulting matrix multiplication and inversion of the Fisher-information matrix based on these points of insensitivity to perturbation generate the large $\sqrt{CRLB}$ values seen. Because these points are dependent on the SM profile layering, frequency, and SM content, it is difficult to know where these insensitive points will appear prior to measurements. For this reason, we suggest the leveraging of multiple frequencies to make efficient use of these coherency effects.

It is evident from these simulations that longer wavelengths are generally better estimators than shorter wavelengths. The use of the lowest frequency (137 MHz, *a*) generally provides the deepest estimation levels as shown in the upper-left subplot. When combined with another frequency, most $\sqrt{CRLB}$ fluctuations are eliminated. For estimation of RZSM, the combination of the three lowest frequencies (*abc*) tends to provide the deepest estimation. The inclusion of the two higher frequencies (*abcde*) is seen to eliminate most large fluctuations in $\sqrt{CRLB}$ across all depths. Thus, for deeper RZSM estimation, the use of 137 MHz is suggested.

Similar to the previous simulation, the surface SM's $\sqrt{CRLB}$ was calculated for each frequency and depth combination shown in Figure 3.3. There results, in most cases, resulted in estimation error far below 0.5%. However, it should be noted that shorter wavelengths (L-band or higher) performed more consistently at estimating surface SM as longer wavelengths are generally more sensitive to variations in subsurface SM.

In summary, the use of multiple frequencies for estimating RZSM is important for repeatable, accurate estimation of $\sqrt{CRLB}$ with longer wavelengths proving to be the most useful for estimation at deeper points in the profile. From a physics-based perspective, it is known that the use of a single frequency can result in ambiguity with respect to depth contributions due to propagation effects and the sinusoidal oscillations of reflection coefficient values as a function of depth. By using multiple frequencies, there is a higher probability of observing depth-dependent signal interactions within the profile, enabling better and more consistent estimation. In the following simulations, the combination of the two lowest frequencies (137 and 255 MHz) as well as combinations of a low and higher frequency (370 and 1575 MHz) are depicted to further illustrate the impact of frequency-specific combinations on estimation accuracy.

3.4.2 CRLB as a Function of Variable and Configurable System Parameters

Within this section, we observe the impact of incidence angles and polarization on $\sqrt{CRLB}$. Based on the previous results, a fixed depth of 30 cm is chosen colorredfor all subsequent analyses as this location shows good estimation accuracy despite increased SM content and reduced frequency observations. For each simulation, we observe the impact that combinations of polarization and incidence angle have on the resultant $\sqrt{CRLB}$ while the remaining parameters are fixed.

3.4.2.1 Varying Angle

The effect of using different incidence angles on the $\sqrt{CRLB}$ is visualized in Figure 3.4. Each measurement uses two polarizations (X and Y) and a combination of frequencies to calculate the $\sqrt{CRLB}$. The left-most column depicts the combination of all five frequencies, the middle column depicts the combination of 137 and 255 MHz, and the right column depicts the combination of 370 and 1575.42 MHz. Each row represents a different SM value for the second dielectric slab.

The general shape of the $\sqrt{CRLB}$ value across the incidence angle sweep is worth discussing from this figure. When all five frequencies are used, no angle performs better than another if the simulation stays away from the grazing angle. However, as we go beyond 75°, the performance of the estimation begins to degrade dramatically. This is in agreement with many spaceborne radar quality control filtering processes to limit measurements near 65°. For the simulations in this study, it is suggested that angles below 75° can be used with relatively equal and positive impact for estimating RZSM.

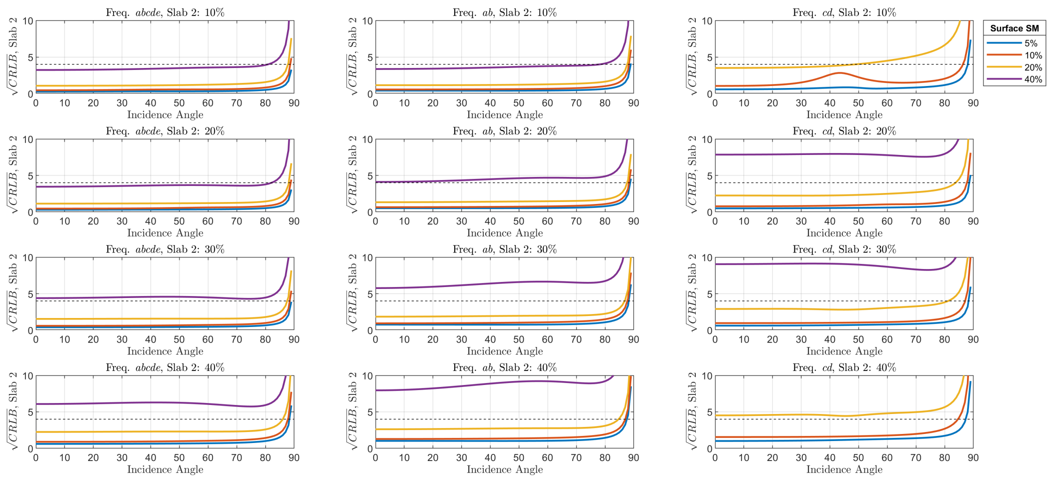

Figure 3.4

Root-zone soil moisture $\sqrt{CRLB}$ as a function of incidence angle. Each column represents a combination of frequency values where the combinations are (137, 255, 370, 1575.42 and 2338.75 MHz), (137 and 255 MHz), and (370 and 1575.42 MHz.) Each frequency value is indicated by the letters a, b, c, d, and e in ascending order. Each measurement uses X and Y polarizations. Each row indicates the value of the SM in the second slab, and the color of each line shows the SM in the first slab. © IEEE 2020.

The middle and right columns separate the problem into two groups of dual frequency combinations. As demonstrated earlier, it is more difficult to estimate moist soils (especially at 30% or above) given reduced frequency measurements. However, the use of the two lowest available frequency values provides the most optimal estimation for the fewest visualized parameters. In contrast to the $\sqrt{CRLB}$ values using 5 frequencies, the values using two frequency measurements feature larger fluctuations in the $\sqrt{CRLB}$ at different surface SM values and at different incidence angles. This is explained by the shifting insensitivity of certain frequencies to a given SM profile configuration which impact the $\sqrt{CRLB}$. When more frequency observations are added, the abrupt changes in $\sqrt{CRLB}$ seen in the dashed line are resolved. Thus, the reduced sensitivity at certain angles is a combination of frequency-dependent and SM profile-dependent properties.

The impact of using different frequency combinations and different incidence angle combinations are shown in Figure 3.5 across multiple SM profile configurations. The incidence angles used are 20, 45, and 70°, and the frequency values and notation are the same as those used in 3.3. As performed previously, each measurement uses all combinations of available frequency, polarization, and incidence angle values. The polarization values used are X and Y.

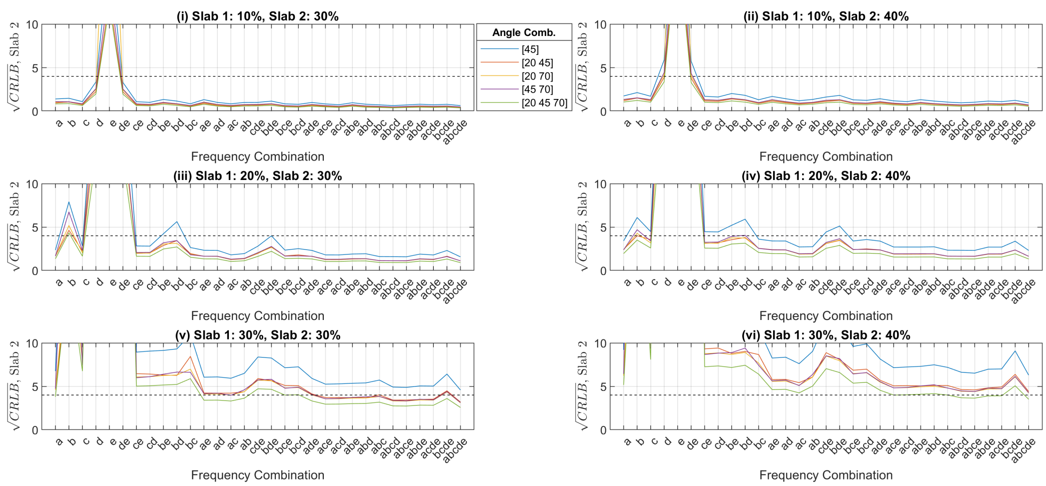

Figure 3.5

Root-zone soil moisture $\sqrt{CRLB}$ as a function of frequency. Frequency combinations are noted along the x-axis where a, b, c, d, and e correspond to 137, 255, 370, 1575, and 2338 MHz respectively. The second slab is fixed at 30 cm below the air-surface boundary. The colored lines show combinations of incidence angle measurements corresponding to the legend at the top of the figure. © IEEE 2020.

Whenever the SM content, primarily the surface SM, is drier, the use of multiple incidence angles is limited. The benefit of using multiple angles, as well as multiple frequencies, is tied most directly to the surface SM content. As higher surface SM causes more reflections at the surface (and, therefore, less energy traveling towards the second slab), the use of multiple measurements becomes more important. As the surface SM increases, the improvement seen by using multiple incidence angles is also shown to be highly important. Thus, Figure 3.5 shows the benefit of using multiple incidence angles as SM content within the profile increases.

While previous simulations have shown the combination of the lowest frequencies tends to produce the most efficient estimator, the lower-left-most subplot of Figure 3.5 shows that the combination ab (137 and 255 MHz) does not perform as well as all other combinations of 137 MHz with another frequency. This is reaffirmed by the lower-left subplot of Figure 3.2 where 255 MHz is shown to be an unideal estimator for a slab fixed at 30cm in the SM profile. This stresses the importance of frequency-, depth-, and SM-dependent interactions in the $\sqrt{CRLB}$ calculation.

Because incidence angle alters the amount of energy transmitted into the SM profile, it can be thought of as adjusting one's sensitivity to the depth of the profile. For this reason, multiple combinations allow one to have adjusted sensitivity to the profile, allowing for better estimation at different depths. This property justifies the improved $\sqrt{CRLB}$ with respect to increasing number of incidence angles as shown in Figure 3.5.

3.4.2.2 Varying Polarization

The effects of combining four polarization states of the receiver are shown in Figure 3.6. Within the upper-left and upper-right subplots, all five frequencies are used, and angles of 20, 45, and 70° incidence are used. Within the lower-left and lower-right subplots, the effect of reducing measurements to a pairing of 137 and 255 MHz (shown in the solid line) and the pairing of 370 and 1575.42 MHz frequencies (shown in the dashed line) is depicted. The x-axis indicates the polarization of the receiver and the number of combinations used for a maximum of 2 polarizations across X, Y, R, and L polarizations.

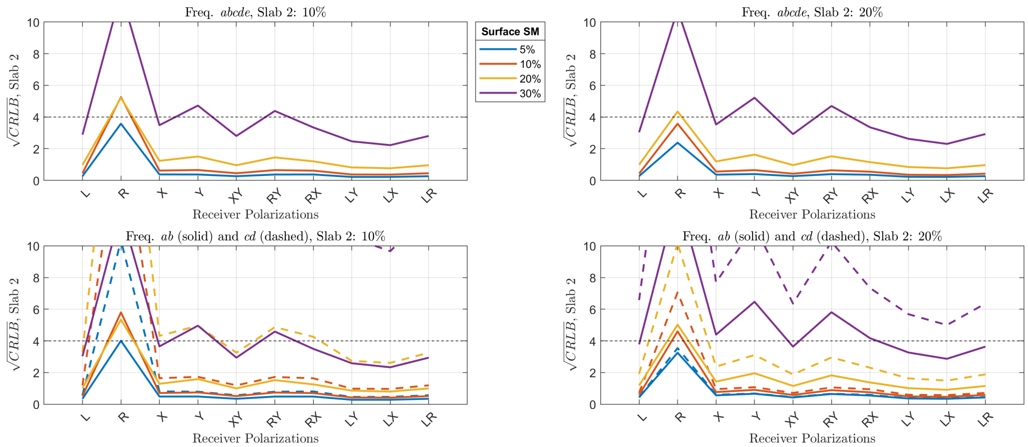

Figure 3.6

Root-zone soil moisture $\sqrt{CRLB}$ as a function of polarization. Each measurement uses incidence angles of 20, 45, and 70°. The top row uses all available frequencies (137, 255, 370, 1575.42 and 2338 MHz) denoted by the letters *abcde*. The bottom row depicts two separate dual frequency combinations. The combination represented by the solid line uses 137 and 255 MHz as denoted by the letters *ab*. Dashed lines use 370 and 1575.42 MHz as denoted by the letters *cd*. The x-axis value represents the receiver's polarization measurement used by each frequency and incidence angle measurement. © IEEE 2020.

Since the wave of a specular, incident signal on the air-surface boundary tends to induce a 90° phase shift and change the polarization state, $\sqrt{CRLB}$ values that only use R polarization do not provide much benefit for the calculation of the $\sqrt{CRLB}$ at 20° incidence. However, the remaining L, X, and Y information provides significant benefit, especially at higher SM conditions. Unlike Figure 3.4 and Figure 3.5 where the resulting $\sqrt{CRLB}$ changed depending on the SM profile, the $\sqrt{CRLB}$ here seems to only be scaled as the SM profile varies. When the number of frequencies is reduced, we observe the same trend in the changing $\sqrt{CRLB}$ as a function of polarization but with a higher $\sqrt{CRLB}$ value caused by eliminating important information from the CRLB calculation. Ultimately, the effect of polarization appears to be relatively independent of frequency as each line shown observes the same shape at different amplitudes as controlled by the polarization information. In general, the use of the cross-polarized signal (L-polarization for these simulations) provides the most information. Additional polarization information, however, can be useful in estimation of more wet soils as shown in the lower-right subplot for the line representing 30% surface SM.

While there is clearly increased performance when the RZSM value increases from 10 to 20%, this behavior is caused by the interaction of the signals with the provided multilayer dielectric structure. This SM-profile-specific behavior is illustrated most clearly in the following section.

3.4.3 CRLB as a Function of Soil Moisture

For this simulation, the $\sqrt{CRLB}$ as a function of surface SM and RZSM is visualized for selected SoOp-R configurations. Figure 3.7 depicts the second slab's $\sqrt{CRLB}$ of a two-slab configuration at 30 cm under varying SM conditions. The upper and lower SM slabs are swept across SM from 5 to 50% in 1% increments. Six receiver configurations are depicted. Each subplot in the left column uses information provided by X- and Y-polarized signals as well as three angles (20, 45, and 70°.) Each subplot in the right column uses information provided by L-polarized signals at 20° incidence only. The top row of subplots uses all five frequencies, the middle row of subplots use two frequencies (370 and 1575 MHz), and the bottom row of subplots use two frequencies (137 and 255 MHz). The number of total measurements are depicted in the title of each subplot. Thus, the total number of measurements range from 5 to 30 for the top row of subplots, and the two remaining rows range from 2 to 12 measurements.

These simulations most clearly show the relationship between the number of measurements, SM, and frequency for calculating the $\sqrt{CRLB}$ of RZSM at 30 cm. The upper-left simulation using

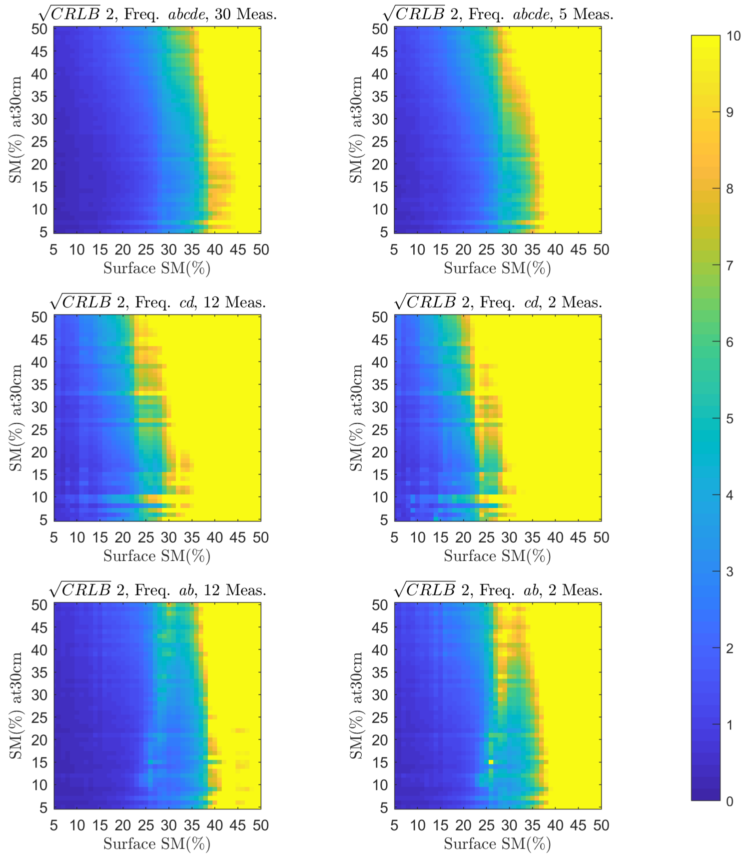

Figure 3.7

Root-zone soil moisture $\sqrt{CRLB}$ as a function of surface and root-zone soil moisture. All subplots in the left column use X and Y polarizations and 3 angles (20°, 45°, and 70°.) All subplots in the right column use L polarization and a 20° angle. The top row uses all available frequencies (137, 255, 370, 1575.42 and 2338 MHz) denoted by the letters *abcde*. The middle row uses two frequencies (137 and 255 MHz) denoted by the letters *ab*. The bottom row uses two frequencies (370 and 1575 MHz) denoted by the letters *cd*. The title of each subplot denotes the number of measurements used in each configuration. © IEEE 2020.

the most observations shows an ideal case where 30 measurements are taken at many frequencies. For this measurement configuration, the ± 4% $\sqrt{CRLB}$ is achieved across a range of surface and root-zone SM combinations where (35, 15)% and (26, 50)% serve as the two endpoints achieving this desired threshold. This subplot also shows that the $\sqrt{CRLB}$ at 30 cm will achieve, at its worst, a 5% error for any combination of SM values for the provided range.

By reducing the number of measurements from 30 to 5 as shown in the upper-right subplot, we can visualize the effect of using fewer measurements with multiple frequencies. By comparing the upper-left subplot the upper-right subplot, it can be seen that the $\sqrt{CRLB}$ values all shift downward along the RZSM axis and to the left on the surface SM axis. After accounting for this shift, the shape of the image representing the CRLB values at each location is generally maintained. In other words, the use of multiple frequencies is able to perform similar estimation at the tradeoff of lower SM values overall. The endpoints of the curve achieving a 4% $\sqrt{CRLB}$ with surface SM and RZSM values is (30, 5)% and (20, 50)%.

The mid-left and lower-left subplot visualizes the impact on the $\sqrt{CRLB}$ by using only 2 frequencies with a total of 12 measurements from combinations of polarization and incidence angle. When the upper-left subplot of 30 observations from 5 frequencies is used as reference, the shape of the $\sqrt{CRLB}$ image is shown to change significantly. Where the two upper subplots visualize a point where all succeeding surface SM values yield a $\sqrt{CRLB}$ beyond 10%, the colorredtwo images here create a sort of blind-spots between surface SM values where the $\sqrt{CRLB}$ increases significantly before decreasing again at a higher SM value (e.g., between 25 and 35% surface SM in the lower-left subplot.) This is caused directly by the sensitivity of the frequencies used to calculate the $\sqrt{CRLB}$. Thus, increasing the number of frequency sources has the effect of smoothing out the blind-spots for SM combinations in the profile. This simulation reconfirms the frequency-dependent behavior observed in Figure 3.3. Generally, however, the endpoints of surface and root-zone SM values achieving a 4% $\sqrt{CRLB}$ are (35, 15)% and (32, 38)% for the mid-left subplot and are (28, 15)% and (18, 50)% for the lower-left subplot.

The mid-right and lower-right subplot show the effects of reducing the 12 measurements from the mid- and lower-left subplot down to 2. When this occurs, the endpoints achieving a 4% $\sqrt{CRLB}$ are (34, 9)% and (21, 50)% for the mid-right subplots and (24, 5)% and (12, 50)% for the mid-lower-right subplots. The general shape of the mid- and lower-left subplot is maintained, but the reduced number of measurements from polarization and incidence angle make the limit the desired $\sqrt{CRLB}$ to shallower depths.

Overall, it is observed that reducing frequencies produces a more varied error $\sqrt{CRLB}$. When either polarization observations or incidence angle measurements are reduced, the maximum RZSM value corresponding to the calculated $\sqrt{CRLB}$ threshold is also reduced. However, the overall shape of the image is maintained.

This simulation also visualizes how the $\sqrt{CRLB}$ calculation is specific to frequency-dependent interactions with the multilayered SM profile structure. As shown in the middle and lower subplots, large patches in the SM / RZSM values where one might expect a linear change in the $\sqrt{CRLB}$ result in large fluctuations. Even without such large changes, each subplot shows small fluctuations in the $\sqrt{CRLB}$ where the value either increases or decreases in somewhat unexpected ways. This behavior was previously displayed in Figure 3.6 when the $\sqrt{CRLB}$ value decreased despite the RZSM value increasing. This behavior is caused by the sensitivity of the different wavelengths to changes in the profile's dielectric. It can be reasonably assumed that, given a sufficient number of frequency sources, these unexpected fluctuations in $\sqrt{CRLB}$ can be eliminated.

3.5 Discussion

The results of this paper assist in visualizing the range of potential inversion accuracy for a wide variety of SM configurations and SoOp-R configuration scenarios. In order to mirror the commonly target 4% estimation accuracy of SM seen across multiple SM-centric remote sensing missions, this paper primarily focuses on analyzing where a 4% $\sqrt{CRLB}$ value is achieved. The range at which this is achievable is highly dependent on the RZSM depth, the SM content of the profile, and the SoOp-R configuration. The results suggest that if one were to follow this modeling pursuit of a two-layer dielectric slab, a RZSM data product should potentially include an indication of the location in the profile where the SM is being sensed due to the sensing depth being highly variable. The simulations shown provide a framework which can potentially aid in SoOp-R receiver design for characterizing system performance at varying ground and receiver-system conditions.

This paper works under the assumption that the SoOp-R measurements experience complex Gaussian noise. While there is precedent in the literature for assuming that the noise for such a SoOp-R-based SM measurement is Gaussian [132], this may not be the case for all circumstances. Different scattering surfaces could potentially induce different noise distributions which would require different assumptions for CRLB studies.

The same noise variance is used for each frequency in this paper. It is unlikely that the noise variance for each system will be identical in reality as the different frequencies / transmitter systems will have independent features that will effect the SNR of the SoOp-R system. For example, different coherent integration times could easily change the total SNR for the system. At this time, the authors are unaware of any noise characterization that has been performed on these systems for SoOp-R applications. While this paper helps to establish the general impact that multiple parameters have on the estimation accuracy, noise variances tailored to each system will help characterize future studies more accurately for the currently available communication systems.

While incidence angle alters the available energy incident upon the surface, incidence angle does not significantly effect the SoOp-R measurement. Because of this, there does not appear to be any incidence angle which provides a more optimal solution if results are contained in a region that does not approach grazing angle. Similarly, the benefit of multi-polarization measurements for RZSM estimation is largely from the addition of observed measurements. Assuming that the polarization is not co-polarized relative to a circularly-polarized transmitter, any standard polarization choice will produce comparable results for lower SM values. As SM content increases, the differences will become more pronounced. For a circularly-polarized source, the optimal antenna in terms of obtaining the minimum $\sqrt{CRLB}$ will use cross-polarization.

A critical assumption made by this paper is that two discrete values representing SM and RZSM are unknown parameters to be solved simultaneously. However, there are many representations and approaches which can be used to solve for RZSM. For example, by fixing the surface SM value based on available data products from resources such as Soil Moisture Active/Passive (SMAP) and Soil Moisture and Ocean Salinity (SMOS) missions, the CRLBcan assuredly be further improved. Alternatively, many inversion-based RZSM papers assume that SM is represented by several discrete layers in the profile (as opposed to the two used here) which can be parameterized by SM mapping functions. The decision by this paper to use two slabs was chosen, in part, to easily visualize the joint effects of known and unknown parameters on estimation accuracy. Further research can explore the impact of discretization of the SM profile on the CRLB, but this is beyond the scope of this paper.

Surface roughness is a critical variable that not only decreases the reflection coefficient, but it also contributes to non-negligible incoherent scattering once the roughness exceeds the Rayleigh scattering criterion. In particular, the compounding effects of surface roughness and topography could be significant over contributing areas within a spaceborne receiver's footprint while will generally be on the order of several hundreds of meters. While previous research has observed successful surface SM estimation from GNSS-R signals under a dominantly coherent signal assumption [21, 105, 128], the effects of topography and surface roughness deserve an in-depth analysis for these spatial scales [31, 34, 53]. Under a moderately SMooth surface assumption ($\approx$ 1.5 cm), coherent signals at L-band and lower will be minimally effected by surface roughness. However, S-band signals will likely be dominantly incoherent at such scales. The joint usage of coherent and incoherent signals should be explored for a variety of topographies and surface roughness values to understand how these components can be leveraged for geophysical parameter estimation from spaceborne platforms.

3.6 Summary and Conclusion

This research presents the study of the $\sqrt{CRLB}$ for SM within a two-layer SM profile by means of SoOp-R measurements. The profiles and measurements are created using the open-source modeling and simulation package SCoBi. Within this study, 30 cm is established as a reasonable depth for RZSM estimation. This study investigates the use of the SoOp-R parameters frequency, polarization, and incidence angle for simultaneous estimation of surface SM (β_1) and RZSM (β_2.) These parameters are used because engineers possess some degree of control in the design process of a SoOp receiver system.

The depth at which RZSM can achieve a $\sqrt{CRLB}$ of 4% is examined by observing the $\sqrt{CRLB}$ as a function of depth for multiple SM profile configurations and two SoOp-R configurations. The two SoOp-R configurations both use 5 frequencies where the first configuration uses 120 measurements from a combination of 6 angles and 4 polarization measurements while the second is restricted to observations at L-polarization and 20° incidence. The 4% lower bound is achieved at 45 cm for the configuration using 120 measurements and 27 cm for a configuration using 5 measurements for a SM profile composed of 30% surface SM and 10% RZSM.

The combined effects of frequency and depth are visualized in Figure 3.3. The results show that an estimator using a single frequency which achieves low $\sqrt{CRLB}$ values may exist. However, changes in the slab position and SM content will consistently cause sharp changes in $\sqrt{CRLB}$ at potentially unforeseeable depths due to nature of SoOp-R interaction with the profile. The addition of a single frequency will largely eliminate these abrupt changes in $\sqrt{CRLB}$. Longer wavelengths are seen to be the most significant factor in increasing the depth at which RZSM can be estimated as one would expect. Based on the problem configuration, this paper chooses to examine the effects that polarization, incidence angle, and SM content play on the $\sqrt{CRLB}$ for RZSM content at 30 cm as this depth provides reasonable estimation above the noise floor for this system.

For polarization and incidence angle measurements, it is found that both variables are helpful in estimating moderately wet SM content. As for polarization, the $\sqrt{CRLB}$ is calculated from a combination of 5 frequencies and 3 angle measurements (20, 45, and 70°) as well as at 2 frequencies (both pairings of 137 and 255 MHz as well as 370 and 1575.42 MHz) with the same angle measurements. It is observed that polarization observations largely perform the same assuming that the receiver is not co-polarized with respect to a circularly polarized transmitter.

However, increasing the number of polarizations used does improve the $\sqrt{CRLB}$ moderately. For incidence angles, it is found that incidence angles between 0 and 75° ensure stable $\sqrt{CRLB}$ when all 5 frequencies are used. When the frequencies are reduced, some frequency-dependent uncertainties can occur with respect to incidence based on the wavelength's interaction with different SM profile configurations at different angles.

A sweep for multiple SM profile configurations is examined under different SoOp-R configurations. It is found that RZSM at 30 cm can achieve a $\sqrt{CRLB}$ of 4% with as few as 2 measurements given sufficient SM profile configurations. When the number of frequencies is limited, the 4% threshold between surface SM and RZSM borders will become increasingly nonlinear, however, this border is made more linear with increasing frequency combinations. RZSM with a $\sqrt{CRLB}$ of 4% can be estimated when both surface SM and RZSM are 30% given 30 measurements. If only two frequencies are used, RZSM can be estimated with 4% $\sqrt{CRLB}$ if surface SM and RZSM are limited to 20% for a combination of 370 and 1575 MHz while a pairing of 137 and 255 MHz can achieve this $\sqrt{CRLB}$ at 30% surface SM.

CHAPTER IV

A NESTED FACET METHOD OF THE KIRCHHOFF APPROXIMATION FOR LARGE-SCALE LAND SCATTERING

This section is inherited from the following journal publication under review [7]

D. Boyd and M. Kurum, ”A Nested Facet Method of the Kirchhoff Approximation for Large-Scale Land Scattering,” *IEEE Transactions on Geoscience and Remote Sensing*, 2023. in review

4.1 Abstract

A nested facet method (NFM) of the Kirchhoff approximation is developed for land applications using signals of opportunity (SoOp). This NFM follows the form of a tree data structure wherein a planar facet is superimposed with a series of child facets. The electric field of a parent facet is taken as the coherent sum of each child facet. The method is found to be flexible and efficient for use on consumer-grade computers, offering significant performance boosts compared to direct integration methods and is easily parallelizable. This solution to the Stratton-Chu integral can provide flexible scattering solutions in areas where analytical or statistics-based solutions may struggle to find an appropriate distribution of the surface.

4.2 Introduction

Microwave remote sensing at global scales has primarily been lead by active radar and passive radiometer applications. As a broad categorization, passive radiometer systems are designed to measure naturally emitted microwave signals from earth surfaces, while active systems such as synthetic aperture radar (SAR) will generate and measure anthropogenic signals. Passive techniques generally feature coarse spatial resolution due to the incoherent averaging of very weak signals over a receiver footprint. SAR systems are generally high spatial resolution but are limited by size, weight, and power (SWaP) constraints for spaceborne systems in addition to international frequency spectrum management. In scenarios where active signals are desired, the repurposing of globally available navigation and communication transmitters for bistatic microwave remote sensing, hereafter referred to as signals of opportunity (SoOp), has shown to be a successful avenue for microwave remote sensing.

The use of SoOp and GNSS reflectometry (GNSS-R) for Earth surface geophysical variable retrieval is a maturing research area. Government-supported research such as the HydroGNSS mission and SoOp P-band Investigation (SNOOPI) technology demonstration are nearing launch and are expected to provide surface and root-zone soil moisture data products respectively [49, 120]. Private companies such as Spire and Muon Space are also supporting the development of global navigation satellite system (GNSS)-based data products [22, 73]. New land-sensing technologies and applications within SoOp are being explored such as the SoOp-SAR concept [131], GNSS-transmissometry [66], and GNSS-R-based machine learning data products [70]. SoOp has shown to be sensitive to several key variables for environmental and hydrological remote sensing due to the wavelength variety available to receivers. For example, the use of signals between I-and S-band show potential for improving root-zone soil moisture data products [60]. Larger wavelengths also exhibit sensitivity to snow-water equivalent through phase techniques [106]. The larger wavelengths of SoOp sources can also aid sensing in densely vegetated areas and even assist in estimating vegetation optical depth [66, 124]. These increasingly complex environments, in addition to the large areas under consideration during delay-Doppler map (DDM) generation, demand comprehensive modeling tools to meet their computational challenge. For the scope of this paper, the computation time of surface scattering and bistatic radar cross-section (BRCS) is of primary interest.

A recent comparison of several scattering models was published in [14] by means of comparing the results to a Cyclone Global Navigation Satellite System (CYGNSS) ground track. Given the uncertainties with Digital Elevation Map (DEM)-scale slopes and surface soil moisture variability, each model captures the general changes in DDM and peak reflectivity across the track. Current models are primarily solutions of the Kirchhoff approximation (KA) [113, Chapter 2] which is applicable for slow varying surfaces with large radius of curvature. These models can be described as purely coherent, incoherent, or mixed based on their formulation.

Analytical models generally make use of surface statistics to describe the average response of the scattered signal. This generally requires making assumptions about the probability distribution function (PDF) of the surface topography. The most prominent method of this form is the Zavorotny-Voronvich GO model (ZV-GO) model developed for ocean applications [135]. This model assumes an arbitrary surface distribution and computes the expected field intensities. The ZV-GO has been modified for use in land applications through the improved GO with topography (IGOT) [74] which follows the surface decomposition technique of [111] to decomposes the surface into a deterministic component taken from DEM data and random components describing both microwave roughness scales and intermediate roughness scales. Once the surface PDF is properly characterized, statistical models such as ZV-GO and IGOT boast extremely fast computation times. These models are strictly incoherent which can be limiting for certain SoOp data products.

Dente et. al have used a hybrid approach to determine the forward scattered electric field [31,34]. The field is segmented into distinct coherent and incoherent calculations. The coherent component is found through a solution of the Kirchhoff approximation where a planar surface is illuminated by a spherical wavefronts transmitted and received by Gaussian antenna patterns. The incoherent component uses the advanced integral equation method. In both cases, a microwave roughness scale is imposed on the facet. This solution found agreement with Technology Demonstration Satellite-1 (TDS-1) DDMs using 300-m facets to describe very large surface areas.

Tsang et. al [114] have developed several solutions to the KA, each seeking a different tradeoff between speed, accuracy, and generalizability of the solution [100, Table 1]. Each model assumes three roughness regimes: a microwave scale, a DEM scale, and an intermediate scale between the microwave and DEM scales. The original method is a direct numerical solution of the KA discretized across a 2-cm grid [53]. The fine-scale partially coherent patch model makes use of the facet method (FM) to solve the KA where the coherent term is computed by the facet method and the incoherent term is solved through Monte Carlo averaging of the intensities [126]. The analytical Kirchhoff solution assumes a three-layer roughness model where the intermediate and microwave roughness scales have an assumed homogenous, joint correlation function. Encouraging results have been found for select simulations by assuming an exponentially distributed microwave roughness and a Gaussian distributed intermediate roughness [100, equation 92].

These models are all solutions to the KA and make use of the tangent-plane approximation in some capacity. Due to the complexity of land surface topography distribution, the development of flexible and efficient numerical solutions are worth exploring as SoOp land data processing matures.

This paper provides a generalized solution to the FM based on the results of [27] within the context of large-scale land remote sensing. The behavior of the model over simple surface geometries is explored, and the computational load of the model is discussed. The model is shown to be accurate under appropriate surface roughness conditions and computationally efficient under evaluation.

Section 2 provides the solution to the facet-method-based KA (FM-KA) and develops a generalized solution of child facets nested within the coordinate reference system (CRS) of a parent facet denominated as nested facet method (NFM). Section 3 provides a discussion of the components that comprise the general FM-KA and NFM and their impact on simulations. Section 4 provides analysis on the accuracy and computational cost of the FM-KA and NFM. We then provide concluding remarks on the applicability of this model.

4.3 Nest Facet Method Formulation

4.3.1 Coordinate System and Variable Conventions

As this model deals with the scattering of fields from parallelogram-shaped facets, we begin by describing facet properties and the CRS conventions used in this model. In this paper, bold variables (e.g., $\mathbf{w}$) indicates a vector and a hat operator (e.g., $\hat{\mathbf{w}}$) indicates a unit vector. A facet will be denoted as k_a where k is the k-th facet on a surface $f_a(x, y)$. The integer a indicates the equal-area projection regime for the surface $f_a(x, y)$ and is further explained in Section 4.3.2. We now focus on describing the properties of the facet k_a as depicted in Figure 4.1.

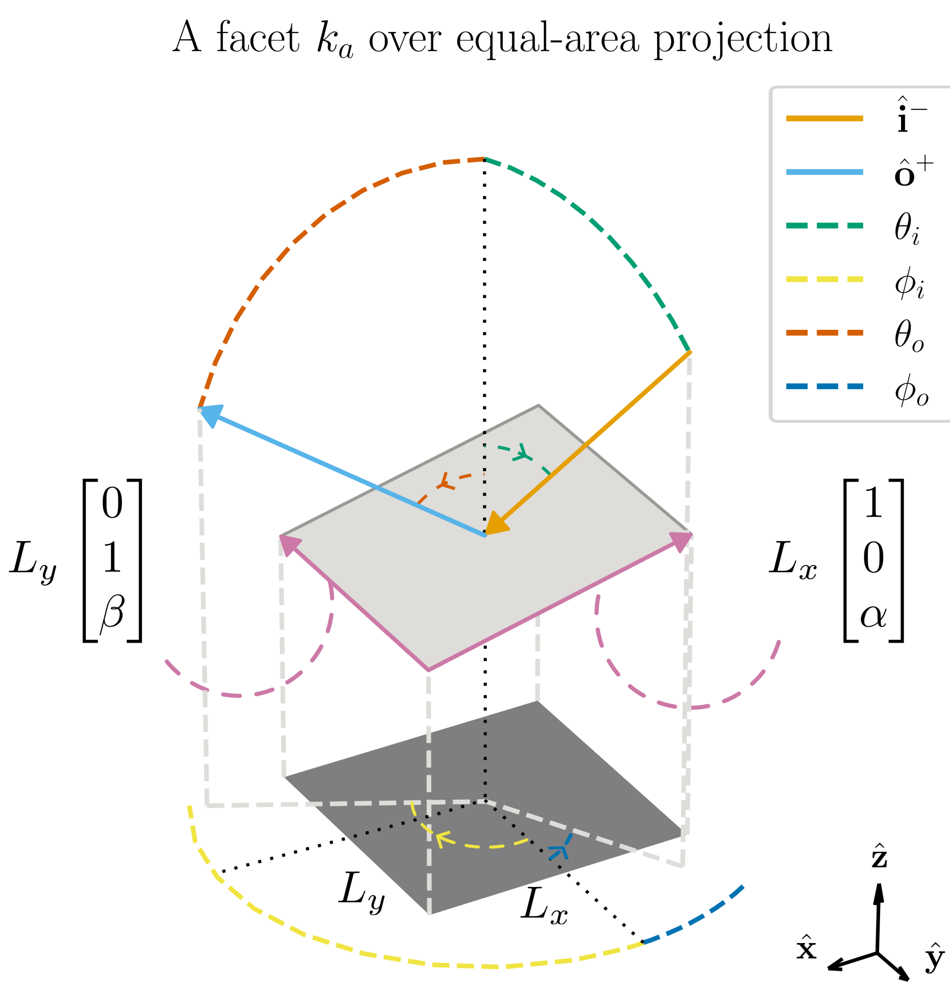

Figure 4.1

A single facet k_a over an equal-area projected CRS using forward-scattering alignment conventions. The legend describes the incidence and azimuth angles for the incoming unit vector $\hat{\mathbf{i}}^-$ and the outgoing unit vector $\hat{\mathbf{o}}^+$.

The facet k_a exists over an equal-area Cartesian CRS where the length of each grid element in the $x-$ and $y-$ directions are L_x and L_y respectively. The CRS of Figure 4.1 denotes the $\hat{\mathbf{x}}$, $\hat{\mathbf{y}}$, and $\hat{\mathbf{z}}$

unit vectors in their respective positive directions and are also visualized through the black dotted lines extending from the center of the equal-area projection. Each facet has an associated incident vector $\hat{\mathbf{i}}^-$ and an outgoing vector $\hat{\mathbf{o}}^+$ where the superscripts + and − indicate the direction along the z-axis. These vectors are indicated in the legend of Figure 4.1. Additionally, the incidence and azimuth angles θ and ϕ associated with vectors $\hat{\mathbf{i}}^-$ and $\hat{\mathbf{o}}^+$ are indicated by the subscripts i and o respectively. Each angle is depicted in Figure 4.1 and are denoted in the legend. As indicated by the scattering vector of Figure 4.1, a forward-scattering alignment convention is used. Additionally, the arcs from the between the the incidence and outgoing vectors are drawn with respect to the appropriate axis. Incidence angles are assumed to always be positive and in the domain $\theta \in [0, 90]^\circ$ while azimuth angles exist in the domain $\phi \in [-180, +180]^\circ$ where a positive angle indicates clockwise rotation about the z-axis.

For each facet, the incline with respect to the z-direction for the x- and $y-$ axis are equal to the slope and aspect variables α and β respectively. The surface assumes an equal-area projection $L_x L_y$, but the total area of the facet is determined by the vectors of the parallelogram denoted in pink in Figure 4.1 where the dotted lines point to the surface vector values. The total area of any given facet can be determined by its $x-$ and $y-$ gradients through $L_x L_y \sqrt{\alpha^2 + \beta^2 + 1}$.

4.3.2 Model Overview

An overview of this paper's NFM is given in Figure 4.2. This method uses a three-scale hierarchy of surfaces $f_1(x, y)$, $f_2(x, y)$ and $f_3(x, y)$ which represent DEM-scale resolution, intermediate-resolution, and microwave-resolution topographies respectively.

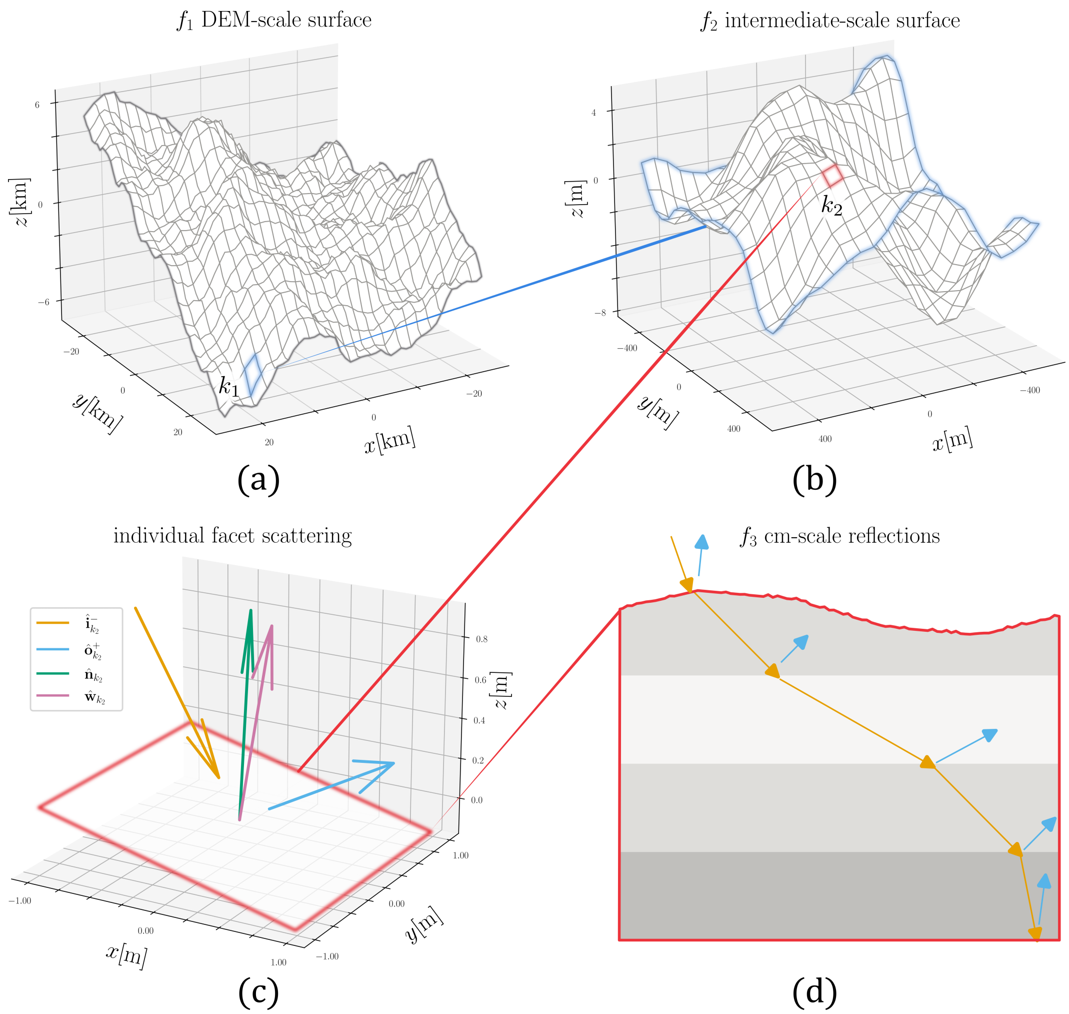

Figure 4.2

Overview of the facet method implementation. (a) A large scale surface is provided. (b) The large-scale surface is decomposed into user-defined subsurfaces. (c) The received field is determined by scattering from the subsurface facets. (d) Microwave-scale effects are incorporated to each facet through reflection coefficient definition.

A large-scale surface is assumed in Figure 4.2(a) which makes use of topography resolutions typically provided by publicly available DEM sources (i.e., ≥ 30[m]). This surface is the first roughness scale provided to the system and is denoted as $f_1(x, y)$ wherein a set of x and y coordinates explicitly provide the surface height along the z-axis. For the use case of SoOp Reflectometry (SoOp-R) over Earth surfaces, $f_1(x, y)$ corresponds to the ellipsoidal height of a surface. On

$f_1(x, y)$ are a total number of facets K_1 and a given facet $k_1 \in [1, K_1]$. Each facet k_1 has the associated CRS properties and variables discussed in Section 4.3.1. Each facet k_1 is the parent of a child surface with intermediate topography scale. The facet k_1 highlighted in blue of Figure 4.2(a) is the parent of the child surface visualized in Figure 4.2(b).

An intermediate-scale surface is presented in Figure 4.2(b). In the context of an ellipsoidal height mapping of f_1, this intermediate surface is intended to convey relevant roughness conditions between the extent of the $f_1(x, y)$ surface and microwave roughnesses which can affect the chosen wavelength used in the Kirchhoff approximation. As this is the second surface used in this model, it is denoted as $f_2(x, y)$. $f_2(x, y)$ represents a child surface whose origin is imposed on a parent facet center from $f_1(x, y)$. When discussing a specific instance of a surface over the k-th facet of $f_1(x, y)$, we denote the surface as $f_{2,k_1}(x, y)$. However, any surface of topography-scale $f_2(x, y)$ is always the child surface of a parent facet k_1 and the notation $f_2(x, y)$ can be safely considered shorthand for $f_{2,k_1}(x, y)$ unless stated otherwise. For all facets k_2 on the surface $f_2(x, y)$, the amplitude of the wavefront over $f_2(x, y)$ is assumed to be constant due to the large ranges provided by spaceborne transmitter and receiver positions. This assumption will allow us to make simplifications to the solution of the FM-KA as later discussed in Section 4.3.4. A single facet k_2 on surface $f_2(x, y)$ is highlighted in red in Figure 4.2(b) and its scattering properties are shown in Figure 4.2(c).

For the facet in Figure 4.2c, all of the facet variables and properties discussed in Section 4.3.1 (e.g., surface slopes, effective area, etc.) are applicable to the facet k_2. All facets along $f_2(x, y)$ are, therefore, directly integrable.

The scattering geometry of Figure 4.2(c) presents incident and scattering vectors $\hat{\mathbf{i}}_{k_2}^{-}$ and $\hat{\mathbf{o}}_{k_2}^{+}$ respectively. Under the parallel ray approximation, the incident and scattering unit vectors for each child facet k_2 approximately equal to its parent facet k_1 of surface $f_1(x, y)$ atop which $f_2(x, y)$ is placed. As such, the parent facet's unit vector for incident and outgoing rays can be used accordingly and are directed towards the center of each facet. Based on this setup, the strength of the scattering can be easily understood by the bisector of the incident and scattering vectors. This is often referred to as the halfway vector in optics and will be denoted as $\hat{\mathbf{w}}_{k_2}$ (c.f., [135, equation 7].) The strength of the reradiated electric field from the individual facet is at its maximum when the surface normal $\hat{\mathbf{n}}_{k_2}$ and bisector $\hat{\mathbf{w}}$ are aligned.

The calculation of the scattered field in Figure 4.2(c) makes use of Fresnel reflection coefficients. The Fresnel reflection coefficient can have information pertaining to surface and subsurface properties included into its calculation. Figure 4.2(d) illustrates this by having both centimeter-scale roughness and multilayer dielectric effects embedded into the coefficient. As this is the third roughness scale introduced, we denote it as $f_3(x, y)$.

While many assumptions are used to simplify the solution for the electric field, the first two roughness scales $f_1(x, y)$ and $f_2(x, y)$ are not required to follow a particular distribution in order to solve for the electric field. To illustrate this, the surface in Figure 4.2(a) was generated using Perlin noise [92] while the secondary surface in Figure 4.2(b) was generated using a Weierstrass-Mandelbrot function [43, eq. 3.47]. This property could prove useful in recreating radio realistic surfaces which may be difficult to solve analytically. With that being said, the microwave roughness f_3 surface characterization follows a Gaussian distribution as discussed in Section 4.3.5

4.3.3 Model

This implementation of the KA follows solutions to the far-field Stratton-Chu integral as provided by [26, 107, 117]. With the assumed time factor of $\exp(j\omega t)$, the integral is defined by

$$\mathbf{E}_o = \mathcal{K}_{k_a}\hat{\mathbf{o}}^{+} \times \int \left[\hat{\mathbf{n}} \times \mathbf{E}_{i,q} - \eta_s \hat{\mathbf{o}}^{+} \times \left(\hat{\mathbf{n}} \times \mathbf{H}_{i,q}\right)\right] \exp\left(jk_0 \mathbf{r} \cdot (\hat{\mathbf{o}}^{+} - \hat{\mathbf{i}}^{-})\right) dS \tag{4.1}$$

where

$\hat{\mathbf{o}}^{+}$ is the outgoing scattering vector traveling upwards along the local CRS z-axis

$\hat{\mathbf{i}}^{-}$ is the incoming incident unit vector traveling downwards along the local CRS z-axis

$\hat{\mathbf{n}}$ is the local surface normal for a surface

$\mathbf{r}$ is the local position vector in Cartesian coordinates

η_s is the impedance of the surface

$\mathbf{E}_{i,q}$ is the electric field on the surface normalized by E_0 induced by an incoming incident vector

$\mathbf{H}_{i,q}$ is the magnetic field on the surface normalized by E_0

$\mathbf{E}_o$ is the outgoing electric field

Additionally, the incident phase and spreading loss terms at the surface center are

$$\mathcal{K}_{k_a} = -jE_0 k_0 \frac{\exp(-jk_0 R_{tk_a} + R_{rk_a})}{4\pi R_{tk_a} R_{rk_a}} \tag{4.2}$$

where R_{tk_a} is the range from the transmitter to facet center k_a and R_{rk_a} is the range from facet center k_a to receiver respectively.

This definition of Stratton-Chu assumes that coherent summation is achievable by accounting for the phase difference induced by the range $\mathbf{r} \cdot \hat{\mathbf{i}}^{-}_{k_a}$ which is feasible under the constraints of the parallel ray approximation. The Stratton-Chu integral describes the solution of a scattered electromagnetic wave over a given surface. The solution detailed in the subsequent sections discretize a large surface into multiple rectangularly segmented areas where equation 4.1 can be applied and coherently summed to establish a solution for a scattered wave. We begin by solving this equation for a general case.

4.3.3.1 General Solution of the Facet Method

The model assumes multiple topography scales as depicted in Figure 4.2. While the specific implementation assumes two scale features, we will describe the FM-KA for a given arbitrary topography scale a. In other words, this model only implements values for $a \in [1, 2]$. Regardless of the number of topography levels, we can describe the total, coherently summed field over a surface of the equal-area projection scale a as the total electric field received from each facet k_a over a total number of facets K_a along the surface $f_a(x, y)$.

$$\mathbf{E}_s^{\text{total}} = \sum_{k_a=1}^{K_a} \mathbf{E}_{k_a} \tag{4.3}$$

Where each parent facet $k_a \in [1, K_a]$ can be described as the summation of several child facets $k_{a+1} \in [1, K_{a+1}]$.

$$\mathbf{E}_{k_a} = \sum_{k_{a+1,k_a}=1}^{K_{a+1,a}} \mathbf{E}_{k_{a+1},k_a} \tag{4.4}$$

For legibility, we will assume that k_{a+1} and K_{a+1} are shorthand for k_{a+1,k_a} and K_{a+1,k_a} as the child facet k_{a+1} must naturally be associated with a parent facet k_a. For example, any facet k_2 along the surface $f_2(x, y)$ must belong to a parent face k_1 from the domain $f_1(x, y)$. The wavenumber

k_0, however, is not associated with this notation denoting facets and retains its definition of $2\pi/\lambda_0$ where λ_0 is the wavelength within the medium of transmission.

The local horizontal and vertical polarization bases can be described with respect to the surface normal of each facet k_a along $f_a(x, y)$. We write theses polarization basis vectors with respect to the ray incident along facet k_a from the transmitter as $\hat{\mathbf{i}}^-_{k_a,i}$, the vector from scattering element k_a to the receiver as $\hat{\mathbf{o}}^+_{k_a,i}$, and the surface normal along k_a as $\hat{\mathbf{n}}_{k_a}$. The polarization basis vectors are then

$$\hat{\mathbf{h}}_{k_a,i} = \frac{\hat{\mathbf{i}}^-_{k_a} \times \hat{\mathbf{n}}_{k_a}}{\left|\hat{\mathbf{i}}^-_{k_a} \times \hat{\mathbf{n}}_{k_a}\right|} \tag{4.5a}$$

$$\hat{\mathbf{v}}_{k_a,i} = \hat{\mathbf{h}}_{k_a,i} \times \hat{\mathbf{n}}_{k_a} \tag{4.5b}$$

$$\hat{\mathbf{h}}_{k_a,o} = \frac{\hat{\mathbf{n}}_{k_a} \times \hat{\mathbf{o}}^+_{k_a}}{\left|\hat{\mathbf{n}}_{k_a} \times \hat{\mathbf{o}}^+_{k_a}\right|} \tag{4.5c}$$

$$\hat{\mathbf{v}}_{k_a,o} = \hat{\mathbf{n}}_{k_a} \times \hat{\mathbf{h}}_{k_a,o} \tag{4.5d}$$

To maintain consistency with an arbitrary polarization bases pq (e.g., E_{pq} in [119, eq. 5.15]) and to provide simpler notation, we write these polarization bases with respect to the arbitrary polarization of the incident wave q

$$\hat{\mathbf{q}}_{k_a,i} = \begin{cases} \hat{\mathbf{h}}_{k_a,i} & q = \mathrm{h} \\ \hat{\mathbf{v}}_{k_a,i} & q = \mathrm{v} \end{cases} \tag{4.6a}$$

$$\hat{\mathbf{q}}_{k_a,o} = \begin{cases} \hat{\mathbf{h}}_{k_a,o} & q = \mathrm{h} \\ \\ \hat{\mathbf{v}}_{k_a,o} & q = \mathrm{v} \end{cases} \tag{4.6b}$$

Given a surface defined by a Cartesian system with components X_{k_a}, Y_{k_a}, Z_{k_a}, the gradients along x- and y-axes for this surface are given by α_{k_a} and β_{k_a}. The size of each rectangular facet k_a is denoted along the equal-area projection XY plane by L_{x,k_a} and L_{y,k_a} for a given surface $f_a(x, y)$.

We now find a solution of the electric field over a single facet k_a. Taking the solution of [117, eq. 12.11-12.16] for linear polarization bases of arbitrary orientation q, the inner cross-products of equation 4.1 which describe the electric and magnetic fields on a facet k_a can be solved under the tangent-plane approximations as as

$$\begin{aligned} \hat{\mathbf{n}}_{k_a} \times \mathbf{E}_{i,q} = (1 + \Gamma_{gh})(\hat{\mathbf{q}}_{i,k} \cdot \hat{\mathbf{h}}_{k_a,i})(\hat{\mathbf{n}}_{k_a} \times \hat{\mathbf{q}}_{k_a,i}) \\ - (1 - \Gamma_{gv})(\hat{\mathbf{n}}_{k_a} \cdot \hat{\mathbf{i}}^{-}_{k_a})(\hat{\mathbf{q}}_{k_a,i} \cdot \hat{\mathbf{v}}_{k_a,i})\hat{\mathbf{h}}_{k_a,i} \end{aligned} \tag{4.7a}$$

$$\begin{aligned} \eta(\hat{\mathbf{n}}_{k_a} \times \mathbf{H}_{i,q}) = -(1 - \Gamma_{gh})(\hat{\mathbf{n}}_{k_a} \cdot \hat{\mathbf{i}}^{-}_{k_a})(\hat{\mathbf{q}}_{k_a,i} \cdot \hat{\mathbf{h}}_{k_a,i})\hat{\mathbf{h}}_{k_a,i} \\ - (1 + \Gamma_{gv})(\hat{\mathbf{q}}_{k_a,i} \cdot \hat{\mathbf{v}}_{k_a,i})(\hat{\mathbf{n}}_{k_a} \times \hat{\mathbf{q}}_{k_a,i}) \end{aligned} \tag{4.7b}$$

where Γ is a Fresnel reflection coefficient. The reflection coefficients used in this term are further developed in equation 4.24.

By making use of the stationary-phase approximation, we can eliminate the dependence of the integration term of equation 4.1 from the surface fields of equation 4.7 (see [117, eq 12.20 and 12.21]). Additionally, we observe the presence of the unit angle bisector within equation 4.1 as

$$\hat{\mathbf{w}}_{k_a} = \frac{\hat{\mathbf{o}}^+_{k_a} - \hat{\mathbf{i}}^-_{k_a}}{\left|\hat{\mathbf{o}}^+_{k_a} - \hat{\mathbf{i}}^-_{k_a}\right|} \tag{4.8}$$

where we further define it in relation to the incident wave number as

$$\mathbf{w}_{k_a} = k_0(\hat{\mathbf{o}}^+_{k_a} - \hat{\mathbf{i}}^-_{k_a}) = \begin{bmatrix} w_{x,k_a} & w_{y,k_a} & w_{z,k_a} \end{bmatrix}^\mathsf{T} \tag{4.9}$$

We now group all terms not dependent on the integral which describe the total electric field along the surface induced by a q-polarized source as

$$\mathbf{u}_q = (\hat{\mathbf{o}}^+_{k_a} \times (\hat{\mathbf{n}}_{k_a} \times \mathbf{E}_q - \hat{\mathbf{o}}^+_{k_a} \times \eta(\hat{\mathbf{n}}_{k_a} \times \mathbf{H}_q))) \tag{4.10}$$

This allows us to rewrite equation 4.1 as

$$\mathbf{E}_{o,q} = \mathbf{u}_q \int \exp(j\mathbf{r} \cdot \mathbf{w}) dS \tag{4.11}$$

Because the surface S is explicitly defined by a directly integrable Cartesian CRS, we can perform a change of variables using the relation

$$dS = \sqrt{\alpha^2_{k_a} + \beta^2_{k_a} + 1} dxdy \tag{4.12}$$

which allows us to express equation 4.11 as

$$\mathbf{E}_{o,q} = \mathcal{K}_{k_a} \mathbf{u}_q \iint \exp(j\mathbf{r} \cdot \mathbf{w}) \sqrt{\alpha^2_{k_a} + \beta^2_{k_a} + 1} dxdy \tag{4.13}$$

Following [27, eq. 10], we express the solution of the integral over a rectangular facet of length L_{x,k_a} and L_{y,k_a} as the product of two parameters. First, we regroup the solution to express the effective area of the facet as

$$A_{k_a} = L_{x,k_a} L_{y,k_a} \sqrt{\alpha_{k_a}^2 + \beta_{k_a}^2 + 1} \tag{4.14}$$

The remaining components of the surface phase integral then express surface reradiation as a function of the surface gradients in $x-$ and $y-$ directions and the scaled bisector $\mathbf{w}_{k_a}$

$$G_{k_a} = \operatorname{sinc}\left(\frac{L_{x,k_a}}{2}(w_{x,k_a} + w_{z,k_a}\alpha_{k_a})\right) \operatorname{sinc}\left(\frac{L_{y,k_a}}{2}(w_{y,k_a} + w_{z,k_a}\beta_{k_a})\right) \tag{4.15}$$

where the aforementioned gradients are α_{k_a} and β_{k_a} and the Cartesian components of $\mathbf{w}_{k_a}$ were previously defined in equation 4.9. The sinc term is defined as $\frac{\sin(x)}{x}$. We use this to write equation 4.11 once more as

$$\mathbf{E}_{k_a,q} = \mathcal{K}_{k_a} A_{k_a} G_{k_a} \mathbf{u}_q \tag{4.16}$$

Given this solution for the electric field induced by a q-polarized signal along facet k_a, we can describe the p-polarized component of the total, coherently summed field as

$$E_{p,q}^{\text{coh}} = \hat{\mathbf{p}}_a \cdot \sum_{k_a=1}^{K_a} \mathbf{E}_{k_a,q} \tag{4.17}$$

where $\hat{\mathbf{p}}_a$ represents a linear polarization reference for the scattered field for the surface CRS belonging to k_a as observed by a receiver. The value of $\hat{\mathbf{p}}_a$ follows the evaluation of equation 4.5, however the surface normal of equation 4.5(c) is replaced with the CRS $\hat{\mathbf{z}}$ unit vector.

4.3.4 A nested facet method

Having a general solution, we now create a NFM by simplifying the calculation of a child facet's electric field using properties of its parent facet. For better legibility, we will formulate this model using the topography scales depicted in Figure 4.2 but note that these can easily be abstracted to an arbitrary topography scale a as discussed in Section 4.3.7.

Recall that $f_{k_2}(x,y)$ is the child of a parent surface $f_{k_1}(x,y)$ where the origin of the child surface $f_2(x,y)$ rests on the center of parent facet k_1 as depicted in Figure 4.2(b). The local CRS of $f_2(x,y)$ is defined by the rotation from the CRS of the parent facet $f_{k_1}(x,y)$ as given by

$$R(\alpha_{k_1},\beta_{k_1})_{k_1\to k_2} = \begin{bmatrix} c_x & \alpha_{k_1}c_x & 0 \\ 0 & c_y & \beta_{k_1}c_y \\ -\alpha_{k_1}c_z & \beta_{k_1}c_z & c_z \end{bmatrix} \tag{4.18}$$

where

$$c_x = (1+\alpha_{k_1}^2)^{-1/2} \tag{4.19a}$$

$$c_y = (1+\beta_{k_1}^2)^{-1/2} \tag{4.19b}$$

$$c_z = (\alpha_{k_1}^2 + \beta^2 + 1)^{-1/2} \tag{4.19c}$$

We can then safely describe the surface fields $\hat{\mathbf{u}}$ on the child surface using the rotated incoming and outgoing vectors of the parent surface.

$$\mathbf{u}'_q = \hat{\mathbf{o}}^{+\prime}_{k_1} \times (\hat{\mathbf{n}}_{k_2} \times \mathbf{E}_q - \hat{\mathbf{o}}^{+\prime}_{k_1} \times \eta(\hat{\mathbf{n}}_{k_2} \times \mathbf{H}_q)) \tag{4.20}$$

where

$$\hat{\mathbf{o}}^{+\prime}_{k_1} = R(\alpha_{k_1},\beta_{k_1})_{k_1\to k_2}\hat{\mathbf{o}}^{+}_{k_1} \tag{4.21a}$$

$$\hat{\mathbf{i}}^{+\prime}_{k_1} = R(\alpha_{k_1},\beta_{k_1})_{k_1\to k_2}\hat{\mathbf{i}}^{+}_{k_1} \tag{4.21b}$$

$$\hat{\mathbf{n}}'_{k_1} = \begin{bmatrix} 0 & 0 & 1 \end{bmatrix}^{\intercal} \tag{4.21c}$$

The surface $f_{k_2}(x, y)$ can then be generated over an equal area projection where its unit vector $\hat{\mathbf{z}}$ is aligned with its parent facet's normal vector $\hat{\mathbf{n}}'_{k_1}$. This concept is visualized in Figure 4.2(b) where the locally flat CRS projection highlighted in blue is shown to be a tilted plane in the parent facet's CRS of Figure 4.2(a).

With this modification, all parameters outside of the integrand in equation 4.13 are accounted. However, the phase component of $\mathcal{K}_{k_1}$ is unlikely to be representative over the surface $f_2(x, y)$ for available remote sensing wavelengths over Earth. To account for this phase difference, the parallel ray approximation can estimate the change in phase by means of

$$\omega_{k_2} = \exp\left(-jk_0(\hat{\mathbf{i}}^-_{k_1} \cdot \mathbf{r}_{k_2} - \hat{\mathbf{o}}^+_{k_1} \cdot \mathbf{r}_{k_2})\right) \tag{4.22}$$

With this approximation, the field emitted from a single facet k_2 as a function of parent facet parameters k_1 can be expressed as

$$\mathbf{E}_{k_2,q} \approx \mathcal{K}_{k_1}\omega_{k_2}A_{k_2}G_{k_2}\mathbf{u}'_q \tag{4.23}$$

The polarization components can then be found using the same methods presented in equation 4.17. We note that the scalar electric field component observed by the receiver in equation 4.17 can be used in the CRS of the parent facet surface without polarization rotation because the incoming and outgoing vectors will be properly aligned with this method.

4.3.5 Microwave roughness scale considerations

Let us assume that a final roughness scale describing contributions from microwave roughness is desired. Using Figure 4.2 as a reference, we will denote a three-scale roughness regime where the final roughness scale $f_3(x, y)$ describes microwave contributions. Unlike the previous formulations which directly consider numerical calculation of the scattering along a facet, the third-scale roughness term $f_3(x, y)$ in this implementation assumes a surface distribution. In this case, an assumed Gaussian surface height distribution is used in order to modify the Fresnel reflection coefficient as derived in [25, 112]

$$\Gamma_{pq} = r_{pq} \exp\left(k_0 s \cos(\theta_i)\right) \tag{4.24}$$

where the incident angle θ_i is $\arccos(\hat{\mathbf{n}}_{k_2} \cdot \hat{\mathbf{i}}^-_{k_2})$, s is the surface root-mean square (RMS) height, and both p and q correspond to arbitrary destination and source polarizations respectively. For the case of ground reflections, the reflection coefficient becomes Γ_{vq} for a vertically polarized ground reference and an arbitrarily polarized incident field.

$$\theta_{k_a,i} = \cos(-\hat{\mathbf{i}}^-_{k_a} \cdot \hat{\mathbf{n}}_{k_a})^{-1} \tag{4.25}$$

where k_a represents either a facet k_1 or k_2.

As depicted in Figure 4.2(d), the reflection coefficient can make use of multilayer dielectric reflections in order to simulate variable land conditions such as soil moisture gradients. The modified reflection coefficient is then determined through an iterative process as

$$\Gamma_i = \frac{\rho_i + \Gamma_{(i+1)} \exp(-2j\delta_i)}{1 + \rho_i \Gamma_{(i+1)} \exp(-2j\delta_i)} \tag{4.26}$$

where i indicates the layer of the dielectric medium, Γ_i is the solution to the iterative reflection coefficient at layer i, and δ_i is the layer i's phase thickness. Further reading of this solution can be found in [6, Section 1.6] and [86, Chapter 6]. The authors have previously implemented this model in [9, 11] in the context of root-zone soil moisture (RZSM) retrieval. In order to more clearly depict the impact of topography on the received field, the effect of dynamic dielectrics across surfaces will be limited and the Fresnel reflection coefficient used will assume a single representative dielectric layer. The soil moisture dielectric model used in this paper is [36, 91].

4.3.6 Conversion to Scattering Matrix

A discussion on conversion of the electric field calculation to a scattering matrix are presented in Appendix A.1.

4.3.7 Generalized Nested Facet Method

While this paper focuses on the analysis of one and two-scale nested facet methods, we now note that this model is easily generalized. The child surface for the current facet k_a can be invoked at any point that a facet within the bounds of the KA is considered too large to approximate the surface. Under this concept, the NFM can be considered a tree data structure as visualized in Figure 4.3

The general NFM visualized in Figure 4.3 uses a set number of equal-area projection regimes A from which the various surfaces $f_1(x, y), f_2(x, y), ...f_A(x, y)$ reside. Within each equal-area projection regime are a set of facets from k_a to k_{N_a}. The electric field for a given facet is calculated by the coherent sum of all child facets. The dotted lines surrounding each group of facets represent an individual CRS within an equal-area projection regime. The CRS rotation from one surface to another is indicated by the rotation symbols between each surface regime. In the same way that a general tree data structure does not demand each parent node have an equal number of children,

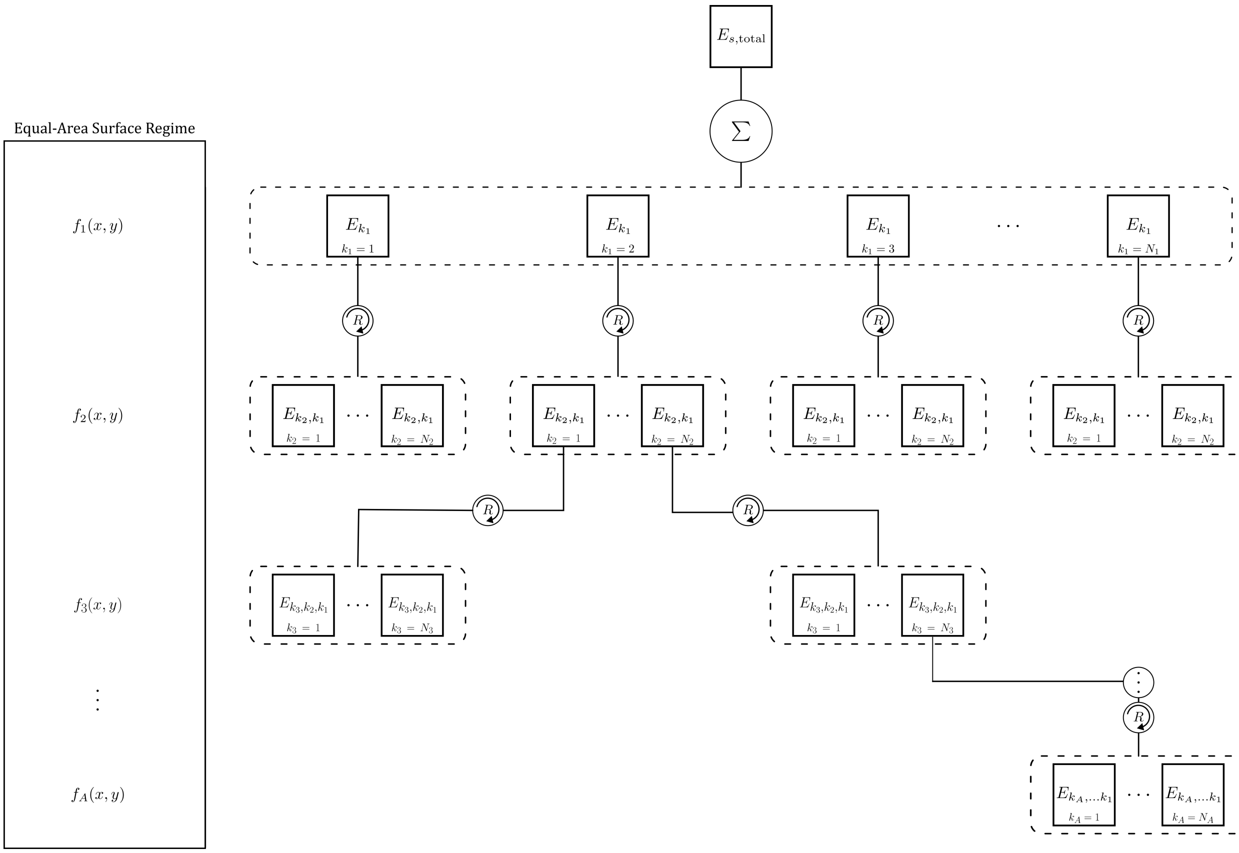

Figure 4.3

A generalized nested facet method visualized as a tree data structure. Each square represents a facet, and dotted rectangles group facets into a surface with a common CRS relative to the parent facet. Each row represents a different equal-area projection regime for the various surfaces. The rotation symbol represents CRS rotation.

not all parent facets within a surface regime require an equal number of child facets. This property can be used to tailor the FM to the shape of the surface when increased resolution is necessary. The NFM created with Figure 4.2 can be considered an instance of the generalized structure seen in Figure 4.3.

4.4 Influence of FM Components on Simulated Electric Fields

In the current and subsequent sections, the behavior and variability of the constituents describing the NFM of equation 4.23 and the general FM-KA of equation 4.16 are simulated over slow-varying topographic structures to provide intuition of their impact on SoOp applications over land. While we are describing the behavior of the NFM of equation 4.23, the behavior of equation 4.23 and 4.16 can be considered interchangeable when considering the contributions from individual facets as opposed to the summation of multiple child facets.

To investigate current SoOp opportunities for land applications, we use CYGNSS and SNOOPI as example SoOp systems, each providing notably different frequencies and bistatic geometry. The assumed frequency and altitudes for each system are noted in table 4.1. Note that ”Tx” and ”Rx” are shorthand for transmitter and receiver.

Table 4.1

Nominal Altitude and Frequency of Simulated Bistatic Systems

	Tx [km]	Rx [km]	Frequency [MHz]
CYGNSS	20200	520	1575.42
SNOOPI	35786	349.52	370

For all subsequent simulations, we assume that the transmitter and receiver are aligned along the x-axis. We define the incident and outgoing unit vectors from the origin of the simulation centered on the specular point as

$$\hat{\mathbf{i}}_s^- = -\begin{bmatrix} \sin\theta_i \cos\phi_i & \sin\theta_i \sin\phi_i & \cos\theta_i \end{bmatrix}^\mathsf{T} \tag{4.27a}$$

$$\hat{\mathbf{o}}_s^+ = \begin{bmatrix} \sin\theta_o \cos\phi_o & \sin\theta_o \sin\phi_o & \cos\theta_o \end{bmatrix}^\mathsf{T} \tag{4.27b}$$

where the subscripts i and o represent the incoming and outgoing directions for the incident and azimuth angles θ and ϕ. Assuming that the transmitter-to-specular-point range R_{ts} and receiver-to-specular-point range R_{rs} are equal to the altitudes listed in Table 4.1, the position of the transmitter and receiver for these simulations can then be defined as $-R_{ts}\hat{\mathbf{i}}_s^-$ and $R_{rs}\hat{\mathbf{o}}_s^+$. We note that a more accurate representation would involve defining the ranges in an earth-centered, earth-fixed CRS. However, this method of defining the transmitter position allows us to maintain the parallel-ray approximation and accurately capture the changes in unit vectors.

As the scope of this paper is focused on isolating the impact of topographical variadtions on the received signal, a constant surface dielectric is used for all subsequent simulations. The surface uses a homogenous Dobson-Peplinski dielectric [36, 91] calculated from 25% soil moisture, a sand fraction of 80%, a clay fraction of 7%, and a bulk density of 1.25 g/cm^3.

4.4.1 Phase approximation errors

The electric field determined by equation 4.23 is enabled by the phase factor of equation 4.22. This approximation of the change in relative range is either acceptable or unacceptable based on the bistatic configuration, carrier frequency, and the size of the region in which the parallel ray approximation is applied. The phase angle errors induced by equation 4.22 are illustrated in Figure 4.4 for both CYGNSS and SNOOPI systems.

Two configurations are shown for both SNOOPI and CYGNSS for specular reflection at 0° and 70° where the x-axis represents the magnitude of the range term present in equation 4.22 where

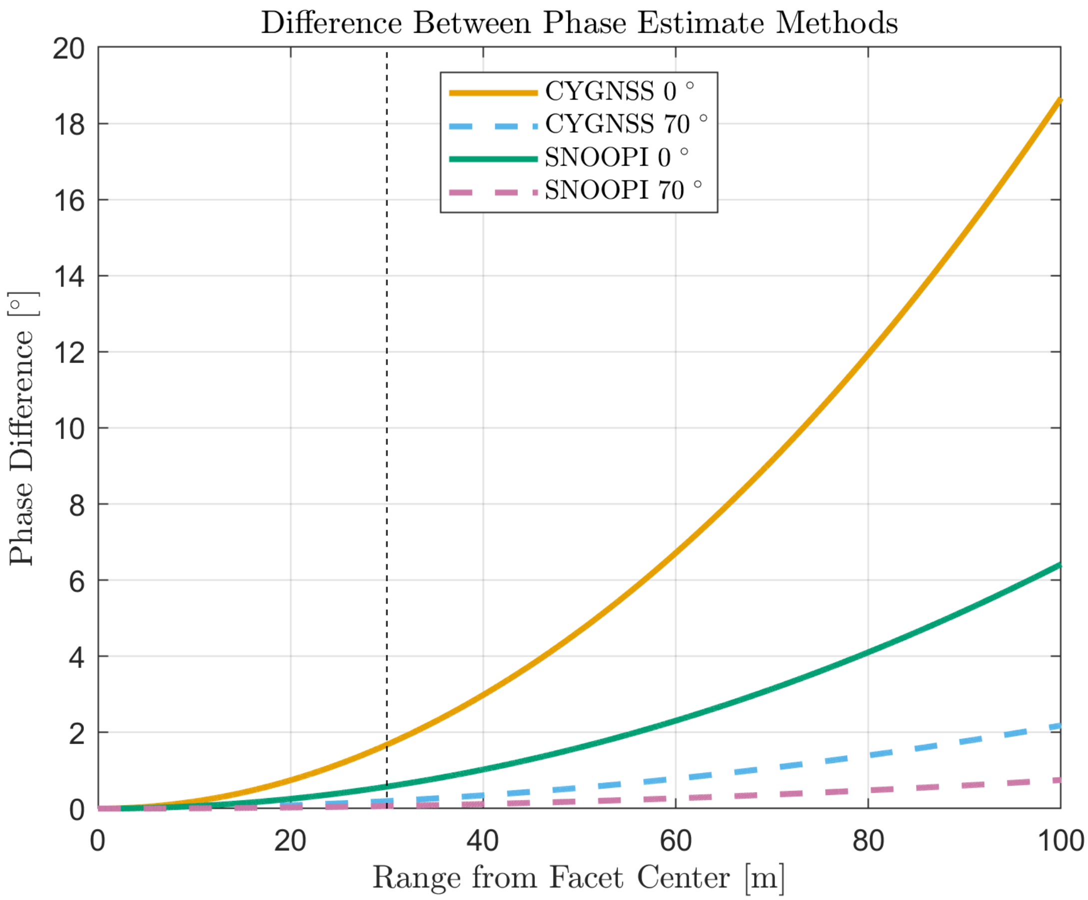

Figure 4.4

Difference between explicitly calculated phase and approximated phase over a facet as a function of range from facet center for two SoOp systems.

the range varies from the facet center at zero to a point 100 meters away. Solid lines represent values given 0° incidence and dashed lines within the legend represent values at 70° incidence. The black dotted line highlights the values near the 30-meter range mark, a distance common for current DEMs. As 100-meter resolution is another common DEM-resolution, the phase error is also calculated up to this point.

The results of Figure 4.4 indicate that specularly reflected values near 0° are more negatively effected by this range approximation than those closer to grazing angles. An expected increase in error is shown for increasing range from the facet center. We observe that for both pairs of incidence angles, the combined effect of changes in carrier frequency and orbital altitude result in SNOOPI being more resistant to these phase errors by a factor of ≈ 3 relative to CYGNSS.

In the context of land-surface scattering applications, it is worth noting the expected ranges of a perfectly flat facet on a given plane. The maximum range from the facet center to a point along a planar facet is ≈ 21 meters for a square 30-m facet and ≈ 70-m for a 100-meter facet. For these specific ranges, we note that the errors along these points for CYGNSS are $\approx 0.8°$ and $\approx 9.2°$ respectively as seein in Figure 4.4. These ranges can change depending on the topography over a facet, but provide a baseline for the maximum expected error for a planar surface. We posit that the range uncertainty of equation 4.22 can be deemed negligible where resolutions finer than DEM gridding is unavailable or considered unnecessary.

4.4.2 Surface Phase Integral, G_{k_a}

The effects of the surface phase integral G_{k_a} can provide valuable insight to understanding the formation of the electric field through equation 4.16. To illustrate this, we visualize the surface phase integral for sample facets over a very large area. The extent that should be considered for SoOp-R applications corresponds to the maximum delay considered during DDM generation. For this example, we consider an area of ±300 [km] based on possible delay considerations for DDM pixels far from the origin.

We visualize 4 different surfaces to understand the surface phase integral. These surfaces are (1) a perfectly flat surface, (2) a surface approximating Earth curvature based on the World Geological Survey 1984 (WGS84) ellipsoid centered along the equator, (3) a Gaussian-based surface with rms height of 50 m and correlation length of 5 km in x and y directions, and lastly (4) a combination of the WGS84 and Gaussian surfaces. An assumed incidence and outgoing angle of 20° is used. The magnitude of equation 4.15 in dB scale is shown using sample facets of size $L_x = L_y = 1$ [m] in Figure 4.5.figure

Figure 4.5(a) provides a reference image of the surface phase integral for comparison with the other 3 plots. We can see that for a facet size of 1m, the output varies slowly and only approaches 0 around 180 km from the specular point. As this is a function of the bistatic geometry with no impact from surface slopes, we verify that the transmitter's incident unit vector $i^{-}_{k_a}$ (located in the negative direction of the x-axis) moves more slowly than the receiver's unit vector. This results in a contortion of the image in the direction of the receiver. The use of 1 meter as a facet size effectively functions as a diffusing reradiating surface which ensures the output of equation 4.15 will be very near 1 for values within 100km of the specular point. The impact of larger facet sizes are illustrated later in Figure 4.7.

The impact of earth curvature is shown in Figure 4.5(b). As expected, the curvature causes G_{k_a} to vary more quickly, though not significantly. The impact of the Gaussian surface roughness can then be understood as coarsening the image of Figure 4.5(a) and (b). The Gaussian surface orients facets to either be aligned or misaligned with the bistatic geometry, ultimately resulting in what is largely an attenuated version of the images on which they are imposed.

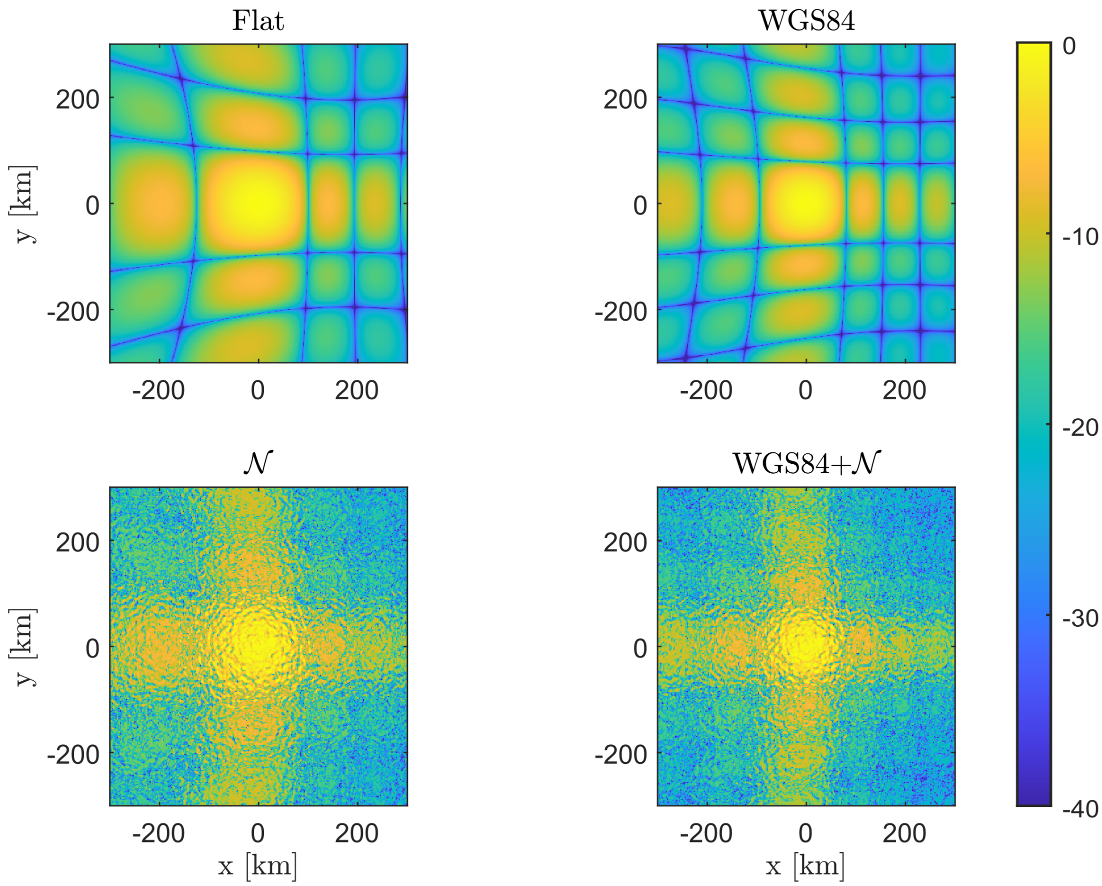

Figure 4.5

Surface radiation pattern over a $300km \times 300km$ surface. The normalized voltage reradiation pattern is shown over the surface for four types of surfaces: flat, WGS84 ellipsoid, Gaussian roughness, and WGS84 + Gaussian roughness

To understand the distribution of the surface phase integral more clearly, we now visualize the distribution of the x and y components of the bisector $\mathbf{w}$. For this visualization, we eliminate the impact of the surface gradients α and β by rotating the bisector $\mathbf{w}$ to be aligned with the local surface normal for each facet. This allows us to more directly use the rotated form of $\mathbf{w}$ within equation 4.15. The corresponding value of each sinc function in equation 4.15 are also visualized in Figure 4.6.

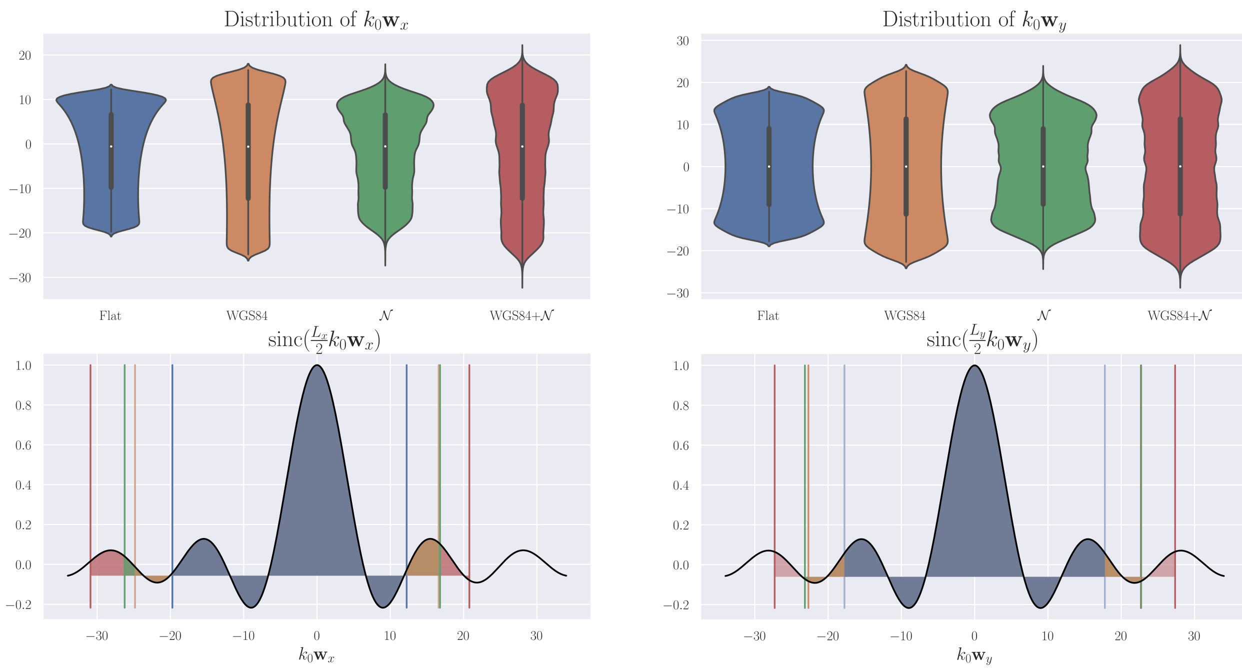

Figure 4.6

Violin plot depicting distribution of half-way vector terms contributing to the surface reradiation pattern of Figure 4.5. The sinc term defining the rectangular reradiation in either x- and y-directions are depicted in the lower plots.

When the bisector is aligned with the surface normal, the sinc terms will produce their maximum output of 1. We see, however, that for the x-components on a flat surface, the bisector is biased in the positive direction near the value of $k_0 w_x \approx 10$. This behavior is explained by the previous comments on the speed at which the incoming and outgoing vectors change over the surface, biasing the values to change more slowly in the direction of the transmitter.

When earth curvature is introduced, the resulting histogram is stretched as the bisector changes more rapidly and equally for all points along the surface. The Gaussian surface roughness then produces the expected effect of coarsening the shape of the histogram.

For the y-direction, the distribution of the points are more equally distributed in positive and negative directions. The biases seen for the flat image near ±10 can then be understood as corresponding to the areas near the corners of each image in Figure 4.6 which outnumber the number of points near the specular point. The effects of the WGS84 ellipsoid and Gaussian surfaces are the same as the effects in the x-direction.

The sinc terms of equation 4.15 are separated by contributions from the x and y directions and visualized in the bottom row of Figure 4.6. From this, we can visualize the impact that the bisector has for the resulting surface phase integral. While values near zero on the axis will the strongest radiation towards the receiver, the larger number of values towards the ends of the violin plot may result in non-negligible scattering from points distant to the specular point.

4.4.3 Surface Fields, u

Having visualized the surface phase integral, the impact of the surface fields within equation 4.10 is of interest within the context of changing bistatic geometry across a surface. For this simulation, a 50 ±50 km length is used in both x and y directions for the surface. A bistatic geometry based on the SNOOPI system is assumed with a homogenous dielectric across a planar surface. The incidence angle is assumed to be 20°. The magnitude of the surface fields is then provided by the left-most figure of Figure 4.7.

The left-most image shows the value of $\mathbf{u}$ for the surface assuming a homogeonus dielectric over a completely flat surface. The top row illustrates the resulting surface phase integral $G()$ and scattering parameter s_{hh} assuming square facets of 1×1 [m], and the bottom row shows the same values for 20×20 [m].

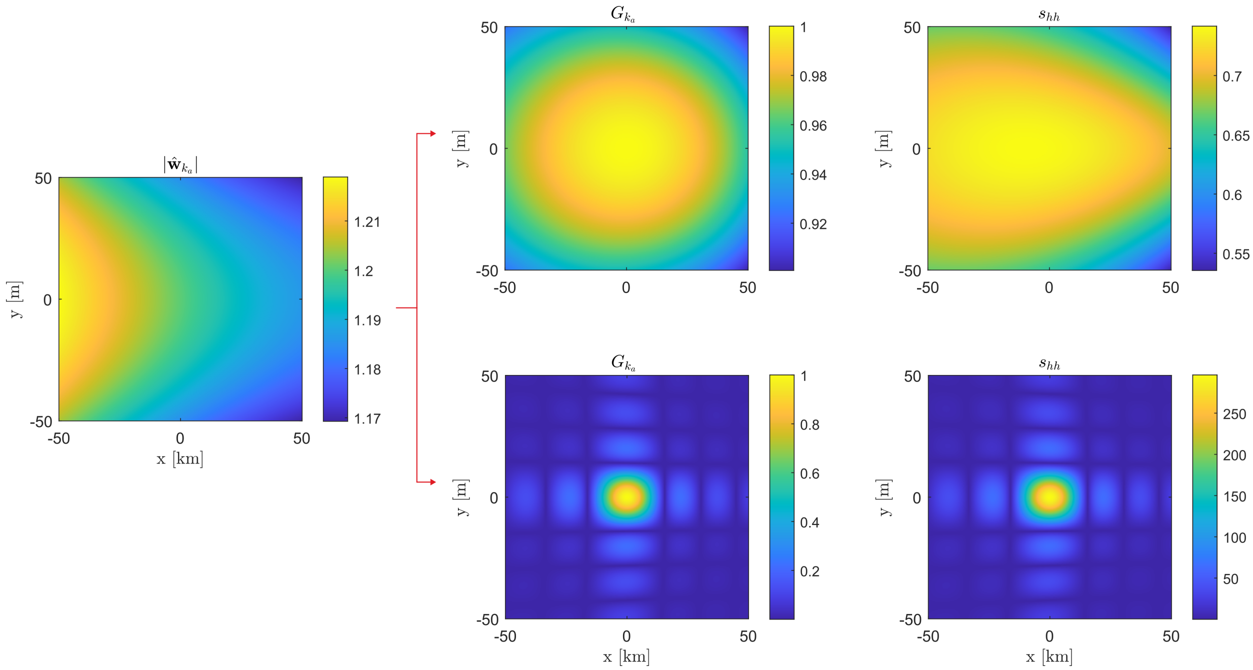

Figure 4.7

Effect of surface fields on resulting image. The leftmost image shows surface fields. The top row shows the following surface phase integral and scattering amplitudes using 1-meter facets while the bottom row shows the same for 20-meter facets.

For very large distances, the portion of the surface which receives the most of the incident field's energy are the facets whose surface normals $\hat{\mathbf{n}}_{k_a}$ are most aligned with the incident vector $\hat{\mathbf{i}}^-_{k_a}$. This results in an unintuitive result: for a flat surface, the facets which are nearest to the transmitter's zenith direction will receive the most incident energy. If the resulting amplitude of equation 4.9 changes more slowly than the dot product of $\hat{\mathbf{n}}_{k_a} \cdot \hat{\mathbf{i}}^-_{k_a}$ in equation 4.7, values near but not at the specular point can produce a slightly higher radar cross section. For the top row of Figure 4.7, the values show that the use of facets of length 1 will result in a slow varying surface phase integral which does not significantly attenuate the strong surface fields near the transmitter. However, the larger facet size along the bottom row does attenuate the signal and produces a resulting scattering amplitude which more strongly resembles the surface phase integral.

4.5 Insights of the Facet-Method-Based Kirchhoff Approximation for SoOp Land Scattering

This section evaluates the performance of the FM-KA and NFM for speed and accuracy. The metrics provided are not meant to be absolute but instead communicate the relative performances of the different models simulated. All reported simulation times are performed on a Dell Alienware x14 using a 2500MHz 12-core Intel i5-12500H central processing unit, 16 GB of LPDDR5 4800 MHz RAM, and a 500 GB M.2 solid state drive. No computations are performed on graphical processing units.

This section compares the FM-KA to the direct numerical integration of the KA (DI-KA) and ZV-GO. The DI-KA evaluates equation 4.1 numerically at fine-scale resolutions. The ZV-GO is taken from [135, eq. 34]. All comparisons are made by calculating the normalized bistatic radar cross-section (NBRCS) as evaluated in equation A.5. The NBRCS of the ZV-GO can be written as

$$\sigma_0 = \frac{\pi|\Gamma|^2|\mathbf{w}|}{w_z^4} P(-\frac{w_x}{w_z}, -\frac{w_y}{w_z}) \tag{4.28}$$

where Γ is the surface reflection coefficient, $|\mathbf{w}|$ is the magnitude of the vector $\mathbf{w}$, and $P()$ represents an arbitrary PDF of the surface slopes but is evaluated as an isotropic, zero-mean Gaussian for this problem.

4.5.1 Impact of Facet Size Relative to Direct Integration Method

Having evaluated the general behavior of the FM-KA, we now examine the accuracy and efficiency of the model under several conditions. The size of a facet given by L_{x,k_a} and L_{y,k_a}

is the primary factor that establishes the speed and memory savings over directly integrating the Stratton-Chu integral in equation 4.1. We begin this analysis on speed and accuracy tradeoffs by noting the change in accuracy for the NBRCS of a 30-meter parent facet with varying facet sizes used by the the child facets.

This simulation calculates the NBRCS of 3 different groups of Gaussian-distributed, Gaussian-correlated surfaces. These surfaces each use an RMS height of 1-meter and correlation lengths of 30, 15, and 7.5 meters. Each surface is generated at a 1-mm discretization level and is then downsampled based on the length of a square, child facet size. The NBRCS of the DI-KA evaluated at 1-mm discretization is then used as the truth value for determining the root-mean square error (RMSE) of the different child facet lengths. This process is then averaged over 50 different simulations for each family of surfaces and carried out for both L-band and P-band signals at 1575 and 370 MHz respectively. This simulation accounts for scattering in the specular direction with incidence and scattering angle aligned on a 20° ray.

Figure 4.8 displays the logarithmic RMSE of the NBRCS calculated from 50 randomly generated surfaces. L-band simulations are indicated by solid lines, and P-band simulations are indicated by dashed lines. The different surface types are indicated by color. Example profile XZ-plane elevation views are provided to illustrate the types of surfaces generated.

Coarser resolutions will result in faster computation time and are thus desired. For all surfaces, a simulation of less than 10 centimeters can be seen as reasonably converging to a solution. However, the interpretation of facet sizes above 50 centimeters is of more interest for relaxing computational costs. For these cases, P-band surfaces exhibit a lower RMSE than L-band simulations. This can be reasonably understood as the wavelength of L-band signals will cause the sinc terms of equation

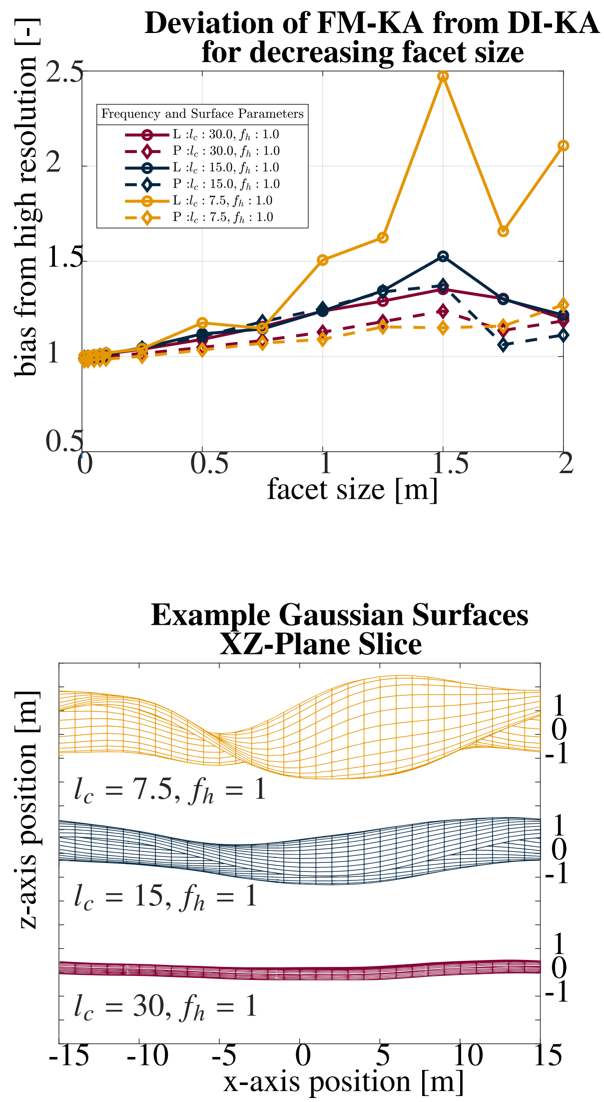

Figure 4.8

Deviation of facet method from direct integration averaged over 50 Gaussian surfaces. Results show HH-polarization centered around 20° incidence, 20° scattering angle. Colors indicate Gaussian surface parameters and line type indicates frequency.

4.15 to more rapidly approach its limit as a delta function for increasing facet size. Since the P-band wavelength and facet size are of similar sizes, the shown facet sizes behave more similarly to a diffusing, isotropic surface reradiation pattern. A facet size of 1-meter is shown to exhibit an RMSE of 3dB or less for all P-band surfaces as well as the smoothest option for L-band.

The results show that a common facet size will have very different impacts on the simulation performance when taking the DI-KA as a true reference. Other simulations not visualized in this paper confirm that increasing the surface roughness will increase RMSE and decreasing surface roughness will decrease RMSE for all simulations provided.

4.5.2 Speed, Time, and Accuracy of the Facet Method

To further illustrate the accuracy and performance of FM-based calculations, we now simulate 50 Gaussian surfaces for a DEM-sized patch. For this simulation, we follow the previous dielectric characteristics and CYGNSS-based geometry. For each randomly generated surface, we assume a 30-meter, square surface with 15-centimeter RMS height and a correlation length of 5 meters across x and y axes.

We simulate the FM at both 0.5- and 1-meter resolutions and compare them to simulations of the DI-KA at 2-cm resolution and the ZV-GO which does not require an input surface for calculations. The NBRCS of each surface is calculated for scattering angles between $\pm 30°$ about a local specular scattering direction of $20°$ at a fixed azimuth angle of $0°$. The results of this simulation are shown in Figure 4.9.

The simulations of both forms of the FM show general agreement with both the ZV-GO and DI-KA. As this is shown on logarithmic scale, the differences between the DI-KA and FM solutions become less noticeable for larger NBRCS.

Of particular interest are the differences in computation time and memory between these different calculations. These results are shown in Table 4.5.2.

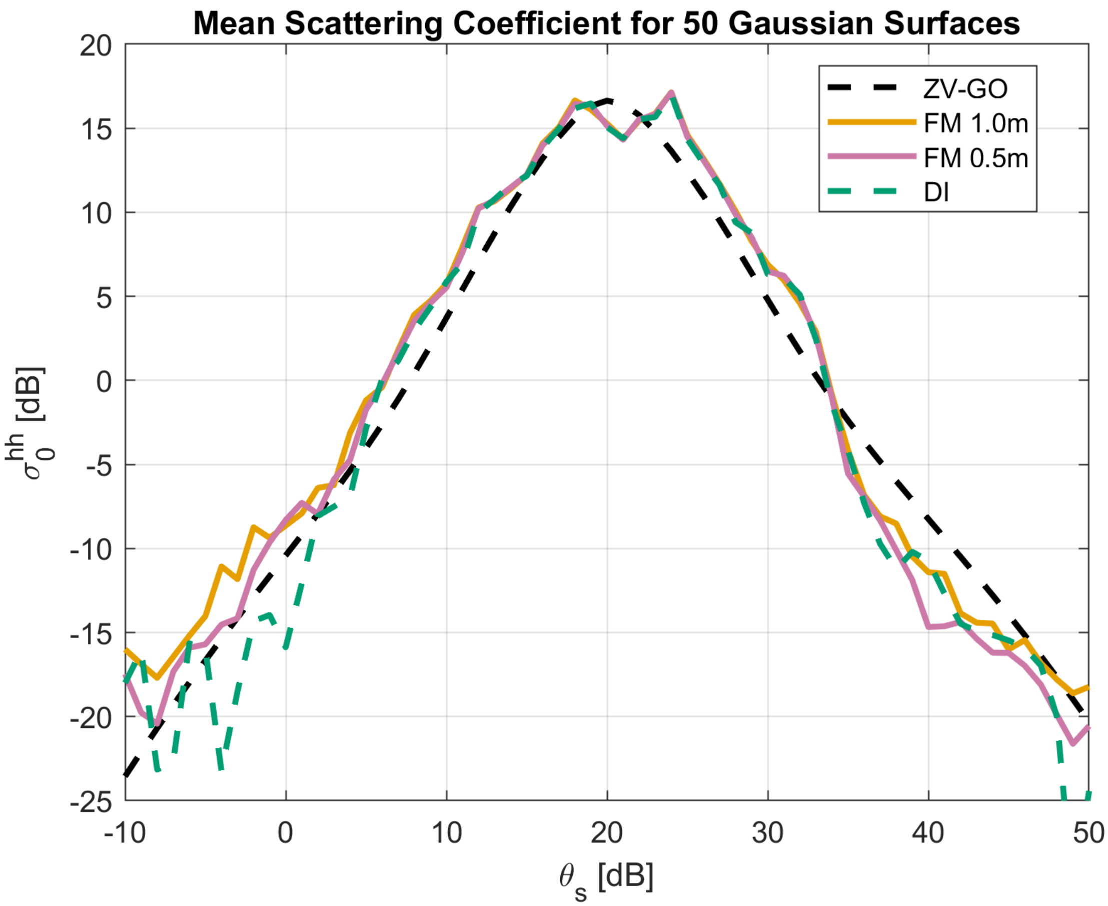

Figure 4.9

Average response of 50 Gaussian generated, Gaussian-correlated surfaces. The square surface length is 30 meters with 5-meter correlation length and 15-centimeter RMS height.

As Table 4.5.2 is only intended to show relative differences and not the specific coding implementation of these methods used in this paper, the RAM used by the input variables to each KA implementation is shown. As the ZV-GO is statistical in nature, its inputs are all scalar terms and can be considered negligible. However, the remaining calculations each make use variables describing the three-dimensional Cartesian surface, incident and scattering vector parameters to the center of the surface, and a scalar term describing a homogenous surface dielectric. Intermediate products such as surface gradients are not accounted in this RAM estimate.

The time reported in Table 4.5.2 reports the total time to calculate 61 different NBRCS as a function of scattering angle for 50 surfaces. The instant time reported is then the time needed to calculate the NBRCS for a single 30-meter facet described by its resolution and the resulting $N \times N$ matrix also reported in Table 4.5.2. The simulation used MATLAB R2021a, and while no parallel processing was specified, it is understood that the MATLAB compiler optimizes some operations given available resources.

These results show, as expected, that the FM-based solutions provide a reasonable intermediate speed and RAM consumption between the statistics-based geometrical optics (GO) and the brute-force DI-KA methods. Paired with the previous results, we conclude that FM-based solutions are reasonable under the correct radius-of-curvature limitations for the system.

Table 4.2

Simulation performance for 60 scattering angles over 50 randomly generated, square Gaussian surfaces of length 30 meters

	GO	**FM**		**DI**
Resolution [cm]	[-]	100	50	2
Surface Size [N x N]	[-]	31	61	1501
Instant Time [ms]	0.026	0.930	2.242	1108.170
Total Time [s]	0.08	2.845	6.859	3391
Input RAM [kB]	0.08	23	89	54072

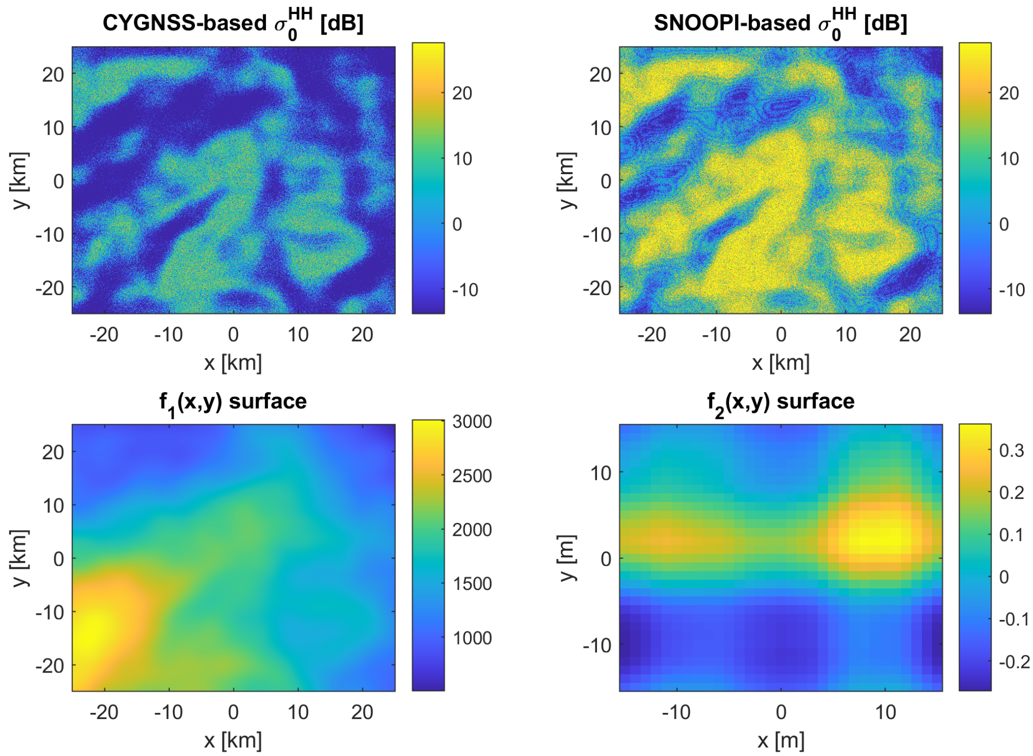

Figure 4.10

Response of CYGNSS- and SNOOPI-based simulations over large topographical areas. The $f_1(x, y)$ surface assumes Perlin noise and the child facets each use Gaussian noise as of 1-meter rms height and 30-meter correlation length.

4.5.3 Large-scale simulation

Similar to the previous simulation, we now compare the time and memory performance of the NFM as shown in Figure 4.2. This, however, compares the results of HH-polarized NBRCS over Earth-like terrain. The $f_1(x, y)$ surface assumes a slow-varying Perlin gradient noise surface superimposed on an ellipsoid mimicking the WGS84 ellipsoid centered at the equator across a 50-km area. Each child facet assumes a 1-meter rms height and a 30-meter correlation length.

The simulations show similar images for both the CYGNSS- and SNOOPI-based simulations. The SNOOPI-based simulations show an overall higher NBRCS with more visible coherent patterns across the surface. This is due to the impact of the facet sizes as discussed in Figure 4.5. Because of this, the CYGNSS image features darker areas that are essentially shadowed by the sinc functions.

The computation times are shown in Table 4.5.2. At a 30-meter equal-area projection resolution using double arrays, the size of the $f_1(x, y)$ surface is roughly 70 MB while each child surface uses only a few kilobytes. When processing on a laptop, the MATLAB compiler will default to a run time of 2614 seconds or roughly 44 minutes. However, since this surface is easily parallelizable, using 12 CPU workers on a 12-core CPU brings the computation time down to 504 seconds. The moderately low time and memory usage of this algorithm allows for the coherent imaging of surfaces on standard, modern computing equipment.

For reference, if the surface was truly continuous and at a 1-meter resolution, the, 3D Cartesian surface using doubles would occupy 55.8 GB in memory, making these surfaces difficult to simulate on current, commercial hardware. The segmenting process achievable by NFMs is thus tractable for modern, low-cost computing resources.

Table 4.3

Simulation performance for NBRCS calculation of Figure 4.10.

	Value	**Units**
f_1 **res**	30	[-]
f_1 **size [NxN]**	1669	[-]
f_1 **RAM**	66.85	[MB]
f_2 **res**	1	[-]
f_2 **size [NxN]**	101	[-]
f_2 **RAM**	23.06	[kB]
Time (Default)	2613.926	[s]
Time (12 Cores)	504	[s]

4.6 Discussion

From these simulations, we observe that the NFM is a tractable method for determining land surface scattering. The NFM of Figure 4.2 is specifically designed for the requirements of SoOp simulations which can require scattering over very large areas. The use of parent and child facets is a tool designed to investigate the uncertainty between the current, publicly available 30-meter DEM datasets and physical simulations.

Without the use of windowing functions, the segmenting process of the NFM cannot be called a continuous surface. Many papers explicitly define the surface as

$$f(x, y) = f_1(x, y) + f_2(x, y) + \dots f_N(x, y)$$

Assuming that the surface is truly continuous, this means that the total memory allocated for the surface $f(x, y)$ is determined by the smallest facet size. While this does produce continuous surface for integration, the impact on memory is quite severe as discussed in Table 4.5.2 and is not easily, if at all, performable on consumer-grade computers. The nesting of parent and child facets into smaller grids is, therefore, the primary benefit of this method. The generation of child facets at run-time naturally means that the surfaces generated by the NFM are not continuous. While this is true, we note that the general FM by definition makes use of parallelograms which can overlap and intersect with one another similar and functions as a Riemann sum. We therefore contend that the concern of a non-continuous surface should only be considered in the presence of sufficient surface elevation data such that sub-DEM surfaces need not be generated. We further note that the use of child surfaces is used in order to mitigate the DEM surface from exclusively functioning as a series of large, planar, specularly scattering surfaces.

4.7 Conclusion

The repurposing of satellite signals as remote sensing transmitters, the defining characteristic of SoOp remote sensing, presents unique challenges for modeling and measuring signals. An increase in transmitter system uncertainty and more robust modeling signal processing are some of the trade-offs for not incurring the SWaP demands of designing a mission-specific transmitter. Because SoOp creates new opportunities to sense key geophysical variables for climate and hydrological analysis, developing a variety of statistical, numerical, and analytical tools for SoOp is essential for meeting the modeling demands of global Earth surface systems.

This paper presents a NFM which modifies the FM-KA to allow flexible modeling of earth surfaces. This method possesses the following beneficial features

1. speed and memory efficient computations capable of simulating scattered electric fields at spaceborne SoOp-scales on consumer-grade computers
2. PDF-independent surface characterization for DEM and intermediate-scale surfaces
3. local surface roughness characterization which follows the gradient of a DEM

The NFM uses a series of parent and child facets to determine the local electric field on parallelogram that is scattered towards a receiver. The electric field is communicated between the parent and child facet coordinate systems through rotation of the local incident and scattering unit vectors. This NFM makes use of the parallel-ray approximation to further simplify the calculation of the scattered electric field. Its phase approximation validity range with respect to the Euclidean distance to the child facet center for CYGNSS and SNOOPI systems is shown in Figure 4.4.

The FM-KA can be compactly segmented into features which describe the surface fields on a facet and surface reradiation pattern towards the receiver through the surface phase integral. The distribution of the surface phase integral over simple surfaces is shown in Figures 4.5 and 4.6, and the impact of the surface fields is shown in Figure 4.7. These figures illustrate that angle bisector and facet size are critical for interpreting the total received field through this method.

The influence of the facet size is further studied in Figure 4.8 through comparison with the DI-KA at both L- and P-band for different Gaussian surfaces. The results show that the FM displays strong agreement with the DI-KA. Simulations at 1-meter resolution are shown to have strong agreement with both the DI-KA and ZV-GO in Figure 4.9.

Tables 4.3 shows the speed and memory performance of the FM-KA and NFM. The FM-KA is found to be an efficient numerical method lying between the two extremes of the ZV-GO and DI-KA.

Finally, Table 4.5.2 shows the speed and memory performance of the CYGNSS- and SNOOPI-based simulations shown in Figure 4.10. The results of Table 4.5.2 show that the NBRCS of the images produced in Figure 4.10 can be produced in roughly 45 minutes using MATLAB's default processing and roughly 8 minutes when using parallel cpu processing. Moreover, the variables used to describe the surface are on the order of several MB as the intermediate-scale surfaces need only be generated at runtime. This is in contrast to methods which preallocate the entire surface which would require several GBs of data to describe the surface and intermediate calculation parameters. The NFM is shown to be tractable numerical method for consumer-grade computers.

CHAPTER V

DESIGN OF A SPACEBORNE, END-TO-END SCOBI MODEL

This section describes an end-to-end modeling and simulation (M&S) framework for signals of opportunity (SoOp) land scattering which will be used to pursue future research and design concepts. It is a modification of the original SoOp coherent bistatic scattering model (SCoBi) framework to include large-scale scattering over Earth's surface.

5.1 Abstract

The multilayer SCoBi extension and the nested facet method (NFM) concept are merged alongside the SCoBi vegetation module to create an end-to-end model for SoOp-based land-scattering applications. The model is composed of five components: a manager module for connecting user inputs and simulation outputs, (2) a geometry module for communicating between several coordinate reference system (CRS), (3) a data-mapping module for decision making at spatial resolutions lower than the available input data, (4) a scattering module which uses the NFM and vegetation modules of SCoBi to describe land scattering, and (5) a delay-Doppler map (DDM) module to describe the measurement observed by a DDM instrument. Each section describes both the governing equations and programming of the end-to-end model for each module.

5.2 Introduction

Having introduced the NFM and multilayer soil moisture (SM) profile modeling, we now combine the established techniques of [7, 11] alongside the vegetation modeling of [65] to create a comprehensive end-to-end modeling framework for SoOp simulations from space. The model is composed of the following modules visualized in Figure 5.1:

1. Manager module
2. Geometry model
3. Data mapping module
4. Scattering module
5. DDM module

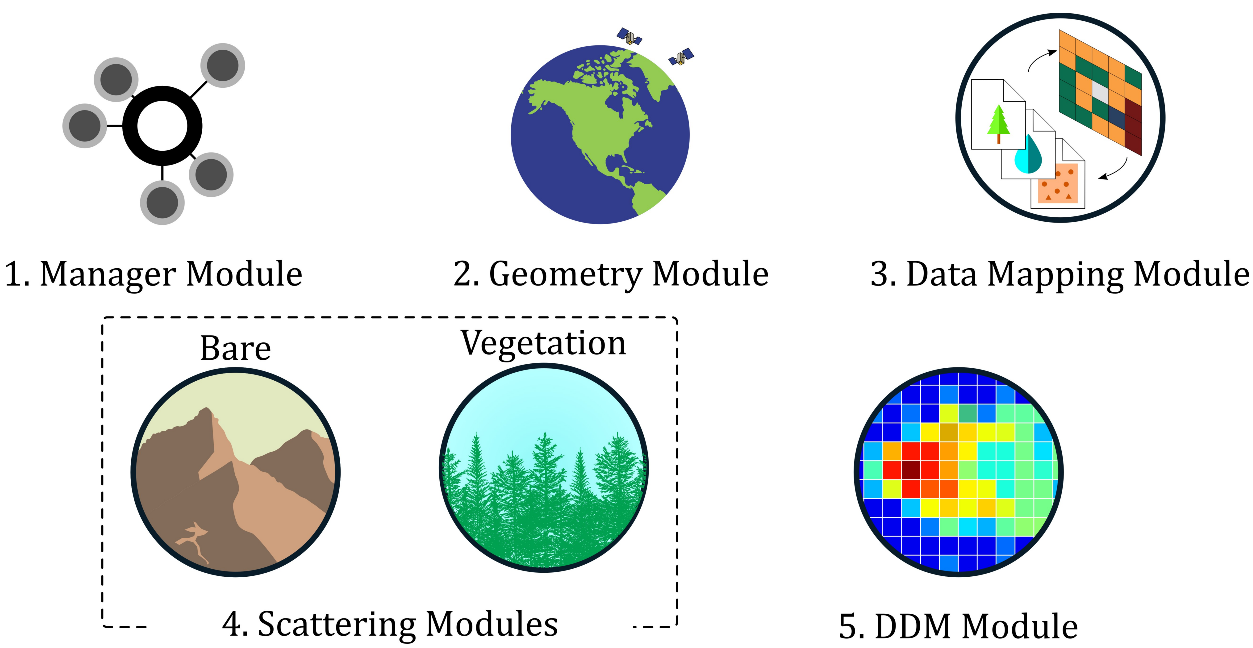

Figure 5.1

SCoBi model overview

5.2.1 Motivation for Model Design

Perhaps the most difficult question for an end-to-end model is that of effectively using imperfect data products of different and generally insufficient spatial resolutions for global applications. If meter-level spatial resolution is demanded, how do we assign variables that change spatially and temporally such as SM, vegetation structure, and the intermediate roughness scales of Figure 4.2?

Naturally, there is no single answer. A semi-empirical approach for assigning SM that works perfectly in, for example, Western Idaho may not be optimal for West Java. Such behavior is demonstrated in [70] where training several hundred machine learning models to estimate SM in as many distinct regions performs better than training one machine learning model to estimate SM globally. Additionally, there are many types of variable assignment approaches: choosing constant values, functional mapping, assignment by probability distribution function (PDF), and machine learning models. These are all reasonable options depending on the available data and time given for a problem.

Motivated by this, one of the primary factors in designing this end-to-end model is the desire to maintain flexibility in the assignment of unknown variables. The overall design of Figure 5.1 is intended to be flexible for variable user data as well as variable computation power.

5.3 Problem Overview

A DDM instrument typically produces measurements in the range-Doppler domain using a matched filter correlation process. Such DDM instruments use a fixed number of correlators placed at specific time delay and Doppler offsets to create a DDM image at a resolution tailored for a specific remote sensing mission. For example, the ocean-sensing Cyclone Global Navigation

Satellite System (CYGNSS) uses an array of 128 × 20 delay-Doppler correlators [102] while the land-sensing SoOp P-band Investigation (SNOOPI) instrument's 370 MHz imager uses a 200 × 3 delay-Doppler correlator array [49]. The delay values will change very slowly over a surface due to plane-wave expansion under the large distances of the transmitter and receiver. Fully simulating a large DDM will require significant processing over large surface areas. However, the slow-varying nature of the waves can be advantageously used for more efficient simulations.

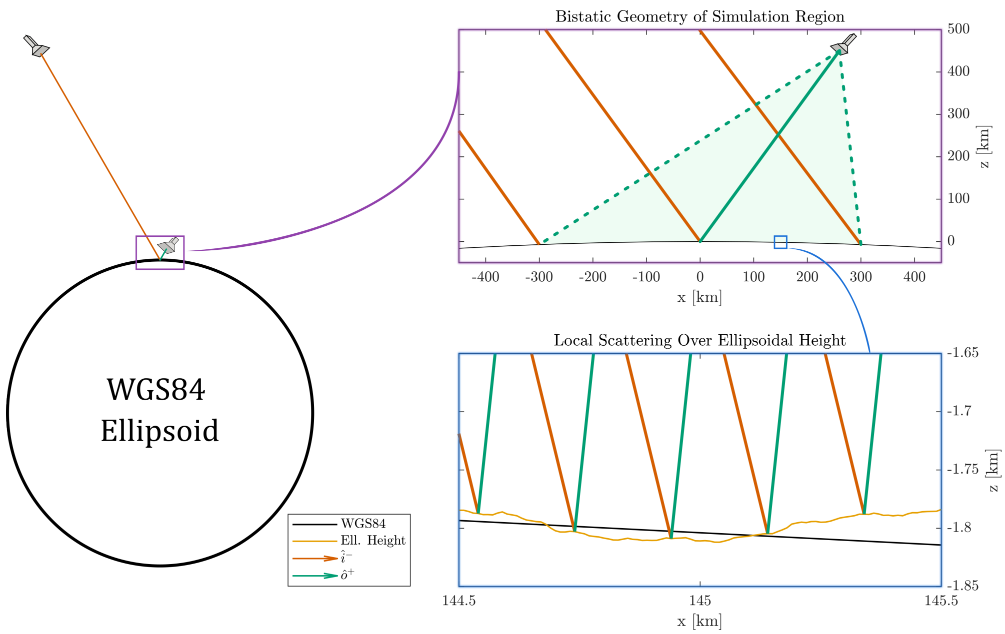

Figure 5.2

Overview of bistatic geometry. (Left) The specular-scattering geometry over the World Geological Survey 1984 (WGS84)-ellipsoid. (Upper right) An arbitrary simulation size of ±300km over the ellipsoid. (Lower right) The local scattering geometry of a 1-km area's ellipsoidal-height-based surface.

An overview of the general bistatic problem from space is visualized in Figure 5.2. The left image shows the general bistatic geometry of the specularly reflected signal over the World

Geological Survey 1984 (WGS84) ellipsoid. The transmitter emits an orange signal which reflects at the specular point. The specular ray towards the receiver is shown in green. The receiver position and WGS84 ellipsoid are to scale with the receiver placed at low-earth orbit at a 30° specular reflection. However, the transmitter's position is half that of the Global Positioning System (GPS) constellation's medium-earth orbit for visualization purposes. A simulation region is highlighted in purple and expanded in the upper-right figure.

An example simulation region is shown in the upper-right portion of Figure 5.2. A ±300-km simulation area is chosen for the 30° scattering geometry. At this scale, the curvature of the WGS84 ellipsoid can be seen over the simulation region. The bistatic geometry is shown for the transmitter and receiver at the specular point as well as the points furthest and closest to the transmitter. While the transmitter's rays are visually similar, the rays representing the field scattered towards the receiver deviate significantly from the geometry at the specular point. This shows the need to account for earth curvature and the changing geometry of the scattered field. A local scattering geometry is highlighted by the blue box and expanded in the lower-right image.

The lower-right image shows the local scattering geometry of a ±0.5km area. In addition to the WGS84 ellipsoid, the ellipsoidal height is superimposed over the surface and shows the true scattering geometry of towards the receiver. At this scale, the scattered fields shown in green remain nearly parallel to one another despite the changes in surface geometry. This local homogeneity of incident and scattered waves provides the basis for the subsequent model derivations.

5.3.1 Governing Equations

Equation 5.1 defines the overall mechanism of a locally scattered field observed by a receiver, and each module works to describe each component. Each variable listed below has an understood subscript of k_1. That is to say, each piece of the equation applies to an individual facet along the Digital Elevation Map (DEM).

$$\underline{b} = K\frac{\exp(ik_0(r_{tk_1} + r_{k_1r}))}{r_{tk_1}r_{k_1r}}\underline{\underline{g}}_r(\hat{\mathbf{o}}^{+})\underline{\underline{u}}_{k_1\rightarrow r}(\hat{\mathbf{o}}^{+})\underline{\underline{s}}(\hat{\mathbf{o}}^{+},\hat{\mathbf{i}}^{-})\underline{\underline{u}}_{t\rightarrow k_1}(\hat{\mathbf{i}}^{-})\underline{\underline{g}}_t(\hat{\mathbf{i}}^{-})\underline{e}_t \tag{5.1}$$

The received field represented as a network scattering parameter of units $\frac{V/m}{\sqrt{Z}}$ is denoted by $\underline{b}$. The 2×1 unit vector $\underline{e}_t$ describes the nominal polarization of the transmitter. The transmitter and receiver antenna's normalized antenna pattern is described using $\underline{\underline{g}}_t$ and $\underline{\underline{g}}_r$. The polarization rotation matrix $\underline{\underline{u}}_{t\rightarrow k_1}$ describes the polarization rotation from the transmitter's antenna polarization CRS to the local DEM facet k_1. The polarization rotation matrix $\underline{\underline{u}}_{k_1\rightarrow r}$ orients the polarization from the DEM CRS to the receiver antenna's polarization CRS. The local scattering matrix is then computed for either ground or vegetation as $\underline{\underline{s}}$. The range terms r_{tk_1} describe the range from the transmitter to facet center k_1, and r_{k_1r} describes the range from facet center to receiver. The term K describes the transmitted power terms as

$$K = i\frac{\lambda_0}{4\pi}\sqrt{P_tG_{0t}G_{0r}} \tag{5.2}$$

where i is the complex number $\sqrt{-1}$, λ_0 is the wavelength in the transmitted medium, P_t is the transmitted power, G_{0t} is the maximum transmitter gain, and G_{0r} is the maximum receiver gain. Please note that the equations of this chapter use an understood time factor of $\exp(-i\omega t)$ which is referenced by clockwise rotation about the complex plane. Chapter IV uses an understood, counter-clockwise-referenced time factor of $\exp(j\omega t)$. Although i and j both represent the value $\sqrt{-1}$, careful substitution of the expression $j = -i$ can be used for communication between methods with differing time factor references.

Many components of the end-to-end model define the scattering matrix for a given DEM facet. Given that this describes scattering over very large earth surface areas, a significant amount of user input is required. In the following sections, we describe the modules of Figure 5.1 and their purpose in fulfilling equation 5.1.

5.4 Manager Module

The manager module is responsible for collecting user input and the branching of subsequent operations. As this is a generalized SoOp model, there is a great deal of system- and frequency-dependent considerations for any given simulation.

If an input is not provided, then a default value is generally asserted as done in other models such as [93]. The following input options are available:

- Hierarchical Data Format version 5 (HDF5) output storage location
- Class-based decision support system (DSS)s for soil, vegetation, and intermediate roughness descriptions
- Options for automatic calculation of scattering region, shadowing of facets exceeding a given delay value,
- Antenna gain pattern descriptions
- Data source locations for DSSs
- DEM resolution scaling
- System (e.g., Technology Demonstration Satellite-1 (TDS-1), CYGNSS, SNOOPI, etc.) or custom descriptions for frequency, polarization, and DDM processing
- Optional scattering methods (e.g., direct surface integration as opposed to NFM)

- Options for calculation methods (single-core, parallel CPU, and GPU processing as of now)

This module makes minimal use of global variables. It primarily serves as a communication method between the input and output of the DSSs but occasionally interacts with other modules to provide computational branching. For example, this module informs following calculations on CPU resources and whether or not they can be used.

The manager module makes prominent use of HDF5 format for storing output data. This is done in order to share output data easily between programming languages and operating systems while allowing for data compression of N-dimensional data.

5.5 Geometry Model

The primary function of this module is to provide communication between different CRS. The total coordinate systems used here are

- The earth-centered, earth-fixed (ECEF) CRS
- The East-North-Up (ENU) CRS with origin at the specular-point
- The gridded DEM CRS
- The local CRS for facet k_1
- The transmit and receive antenna CRS

Following standard data products such as Soil Moisture Active/Passive (SMAP) and TDS-1, the end-to-end module begins in an ECEF CRS. If necessary, calculation of the specular point is performed in this CRS. The ECEF CRS is then converted to an ENU CRS centered on the specular point. A grid is then created along the line formed by the transmitter, receiver, and specular point projected onto the XY plane. The ENU CRS is then rotated about the up unit vector to align with this grid. The model is then capable of determining the CRS rotation between specific elements of the system such as any given facet or the receiver observation direction. The importance of these three CRS rotations is visualized in Figure 5.3 where each CRS is shown to play a distinct role in defining the simulation region. These roles can be summarized as using the ECEF for the general bistatic geometry definition, the ENU CRS for initialization of the simulation region, and the grid CRS for defining specific facets under simulation.

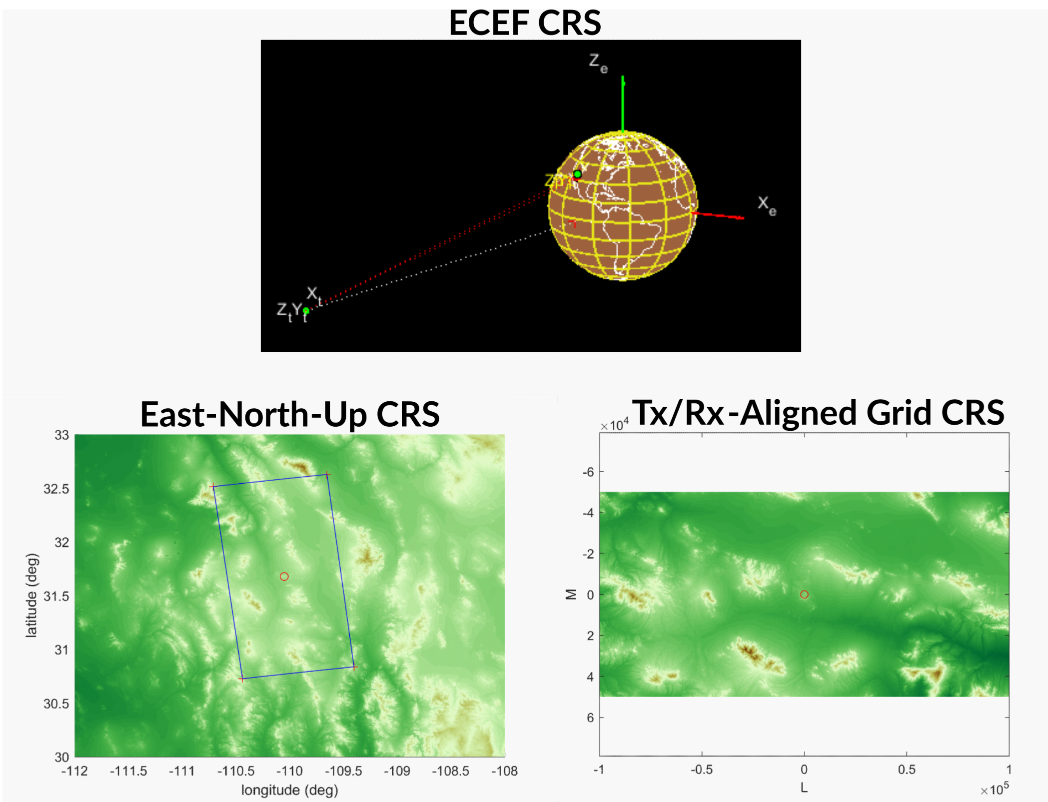

Figure 5.3

CRS transformation between ECEF, ENU, and Grid systems. The specular point is used to determine the simulation region size, and the grid region is then determined. This example shows a rectangular simulation region used to validate the module.

Additionally, the geometry module performs several important tasks. These include

- CRS rotations for all elements within the simulation grid
- Specular point determination (if necessary)
- DEM sampling for simulation scene
- Antenna body rotations

We summarize the workflow below:

5.5.1 Specular Point Determination

Given the scenario where the specular point is not provided as an input, this module makes use of the specular point function provided in [51]. Typically, the specular point is defined as the position in which the path range is minimized for a planar surface. For an ellipsoid surface, the specular point is determined through a gradient descent method over the WGS84 ellipsoid.

5.5.2 Simulation Grid Determination

For SoOp applications involving DDMs, the number of surface elements is generally decided by the desired delay values. We assume that the desired maximum delay is the sum of the maximum delay bin of the DDM and the chip length in seconds. Thus, the number of delay bins is highly influential in the computation time of a simulation. Due to the influence of topography, there is likely no analytical method that can perfectly estimate the size of the DDM over the Earth geoid. However, we can make reasonable approximations following the method of [33]. We can approximate the semi-major iso-delay line over a planar surface as

$$a = \frac{\sqrt{2\tau c H \cos\theta_i}}{\cos^2\theta_i} \tag{5.3}$$

where τ is the maximum desired delay in seconds, H is the receiver altitude over the surface, and θ_i is the local incidence angle.

By using the semi-major iso-delay radius a, we can safely estimate the size of the region for a planar or ellipsoid surface. We note that the path delay along the edge of the simulation region will increase more quickly over an ellipsoid compared to a planar surface which will cause this method to over-estimate the simulation region size. On the other hand, the effect of topography can vary significantly which will cause this method to either over or under estimate. In summary, a perfect description of the simulation region size will require trial and error based on the influence of topography. Due to this ambiguity, the user is provided the option to force a fixed rectangular simulation region size as an input.

5.5.3 Surface Grid CRS

We now define the grid CRS which will house the equal-area projection of the surface $f_1(x, y)$. Assuming the transmitter, receiver, and specular point are well known in an ENU CRS, it is convenient to define a CRS where the transmitter, receiver, and specular point are aligned. We determine the unit vector between the transmitter and receiver as

$$\hat{\mathbf{u}}_{TR} = \frac{\mathbf{r}_{rx} - \mathbf{r}_{tx}}{|\mathbf{r}_{rx} - \mathbf{r}_{tx}|} \tag{5.4}$$

We now determine the simple rotation between the ENU CRS and a grid CRS which aligns the transmitter, receiver, and specular point as

$$R_{\text{enu}\to\text{grid}} = \begin{bmatrix} \cos\theta_g & -\sin\theta_g & 0 \\ \sin\theta_g & \cos\theta_g & 0 \\ 0 & 0 & 1 \end{bmatrix} \tag{5.5}$$

where $\theta_{\text{grid}} = \arccos(\hat{\mathbf{u}}_{TR} \cdot \hat{\mathbf{x}}_{\text{enu}})$.

Note that this rarely results in perfect alignment with the specular point, transmitter, and receiver. Since the specular point is considered the origin of the ENU CRS, its value will remain the origin in the new CRS. If desired, the transmitter and receiver can be forced into alignment such that the transmitter is aligned along the negative x-axis without a y-component and the receiver is aligned along the positive x-axis with no y-component. Additionally, the error in specular point calculation by any method results in unavoidable errors when comparing DDMs to measurements. It should, however, not significantly affect the calculation of the received field.

5.5.4 Ellipsoidal Height

The ellipsoid surface is created by accounting for the total deviation from the reference ellipsoid. DEMs are typically provided with respect to the Earth Gravitational Model 1996 (EGM96) geoid, and the EGM96 geoid is provided with respect to the WGS84 ellipsoid. Assuming that the WGS84 is centered on the specular point, the total surface height is defined as

$$f_1(x_{\text{lon}}, y_{\text{lat}}) = f_{\text{WGS84}}(x_{\text{lon}}, y_{\text{lat}}) + f_{\text{EGM96}}(x_{\text{lon}}, y_{\text{lat}}) + f_{\text{DEM}}(x_{\text{lon}}, y_{\text{lat}}) \tag{5.6}$$

where the subscripts indicate that the surface is defined with respect to latitude and longitude values. To convert from the ellipsoid to meters, the (x, y) pairs are converted by calculating the great circle track distance. The relationship between the different surfaces is depicted in Figure 5.4.

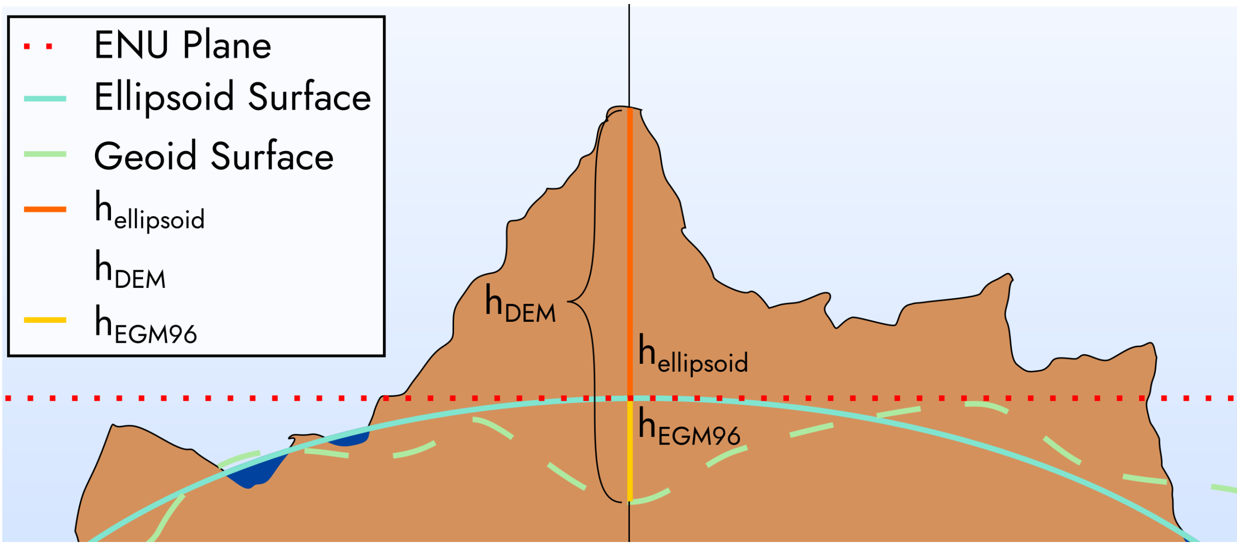

Figure 5.4

Earth surface model relationships

Additionally, the resolution of the ellipsoid varies with respect to the provided latitude and longitude values. To circumvent this, the end-to-end model performs linear interpolation of the surface in order to create a true equal-area projection. While directly interpolating values below the DEM resolution is performable, it is not recommended.

5.5.5 Antenna Body Rotation

In order to properly define the received polarization of the field, knowledge of the antenna's orientation is necessary. Given the propagation direction, the linear polarization ports can be arbitrarily defined. Similar to the ENU CRS, we can define several local tangent plane CRS for an antenna and its spacecraft to properly define the received field with correct polarization changes. We adopt two CRS for this system: a CRS for the spacecraft and another for the antenna. The spacecraft is a local-vertical, local-horizontal (LVLH) CRS defined with respect to the Earth center and the spacecraft velocity direction. It is nominally defined with respect to an ECEF CRS. The antenna CRS can either be defined with respect to a known position along the spacecraft or by aligning it with the ENU tangent plane at the specular point. A spacecraft LVLH CRS and ENU-plane-aligned antenna CRS are depicted in Figure 5.5.

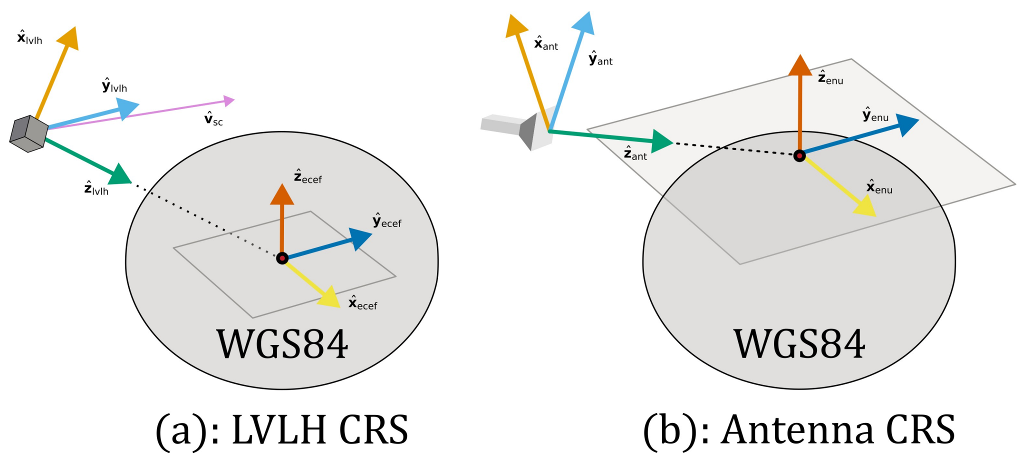

Figure 5.5

(a) The spacecraft LVLH CRS. The spacecraft unit velocity $\hat{\mathbf{v}}_{\text{sc}}$ and earth center define the CRS. (b) An example antenna CRS. The specular point and ENU plane define the CRS.

Following a similar but distinct approach to [83, Section 4.4], we define the spacecraft LVLH CRS with unit velocity $\hat{\mathbf{v}}_{\text{sc}}$ as

$$\hat{\mathbf{z}}_{\text{lvlh}} = \frac{\mathbf{r}_{\text{earth center}} - \mathbf{r}_{\text{sc}}}{|\mathbf{r}_{\text{earth center}} - \mathbf{r}_{\text{sc}}|} \tag{5.7a}$$

$$\hat{\mathbf{y}}_{\text{lvlh}} = \frac{\hat{\mathbf{z}}_{\text{lvlh}} \times \hat{\mathbf{v}}_{\text{sc}}}{|\hat{\mathbf{z}}_{\text{lvlh}} \times \hat{\mathbf{v}}_{\text{sc}}|} \tag{5.7b}$$

$$\hat{\mathbf{x}}_{\text{lvlh}} = \frac{\hat{\mathbf{y}}_{\text{lvlh}} \times \hat{\mathbf{z}}_{\text{lvlh}}}{|\hat{\mathbf{y}}_{\text{lvlh}} \times \hat{\mathbf{z}}_{\text{lvlh}}|} \tag{5.7c}$$

where $\mathbf{r}_{\text{earth center}}$ is the earth center in a given CRS $\mathbf{r}_{\text{sc}}$ is the position of a spacecraft, and $\hat{\mathbf{v}}_{\text{sc}}$ is the unit velocity of the same spacecraft. We evaluate these vectors in the ENU CRS. The rotation matrix from the ENU CRS to the spacecraft CRS is then readily found by

$$R_{\text{enu}\to\text{lvlh}} = \begin{bmatrix} \hat{\mathbf{x}}_{\text{lvlh}} & \hat{\mathbf{y}}_{\text{lvlh}} & \hat{\mathbf{z}}_{\text{lvlh}} \end{bmatrix}^{\mathsf{T}} \tag{5.8}$$

A similar process can be performed for the case where the antenna position of the spacecraft is well-defined. As an example, the CYGNSS spacecraft features two antennas which are oriented roughly 30° from the spacecraft's nadir direction.

$$R_{\text{enu}\to\text{ant}} = R_{\text{body}\to\text{ant}} R_{\text{lvlh}\to\text{body}} R_{\text{enu}\to\text{lvlh}} \tag{5.9}$$

where

$R_{\text{enu}\to\text{lvlh}}$ converts the CRS from ENU to LVLH

$R_{\text{lvlh}\to\text{body}}$ rotates the CRS from LVLH to align $\hat{\mathbf{x}}_{\text{lvlh}}$ and $\hat{\mathbf{y}}_{\text{lvlh}}$ through a 90° rotation about the $\hat{\mathbf{z}}_{\text{lvlh}}$ axis

$R_{\text{body}\to\text{ant}}$ aligns the $\hat{\mathbf{z}}$ of the body CRS with the antenna pointing direction using quaternions

This rotation matrix can then be evaluated for both the grid and local CRS. These rotations are visualized in Figure 5.6.

Thus, the antenna CRS can be defined with respect to the spacecraft's estimated orientation when the position of the antenna along the spacecraft is known. For arbitrary simulation scenarios where the antenna position is unknown, we define an antenna CRS wherein the propagation

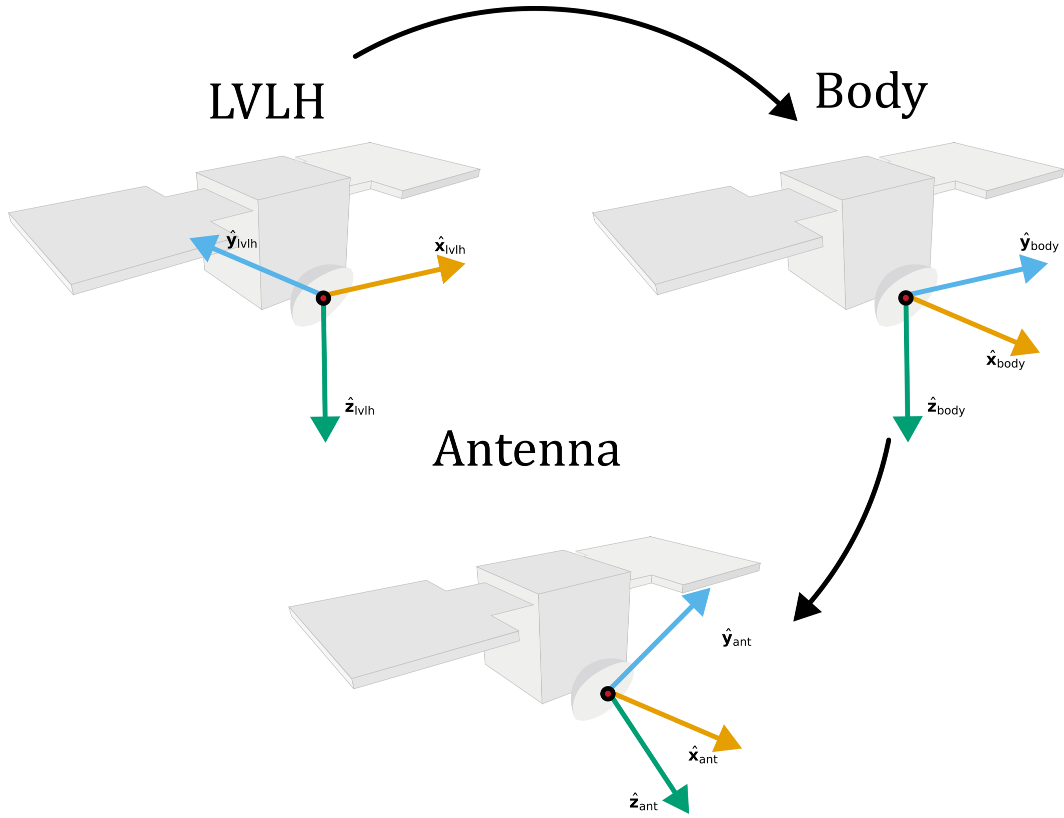

Figure 5.6

Rotations from the spacecraft's LVLH CRS to the body and antenna CRS.

direction is aligned with the specular point and the horizontal polarization component along the $\hat{\mathbf{y}}$ direction is parallel with the XY plane at the specular point in an ENU CRS. In this case, we can create

$$\hat{\mathbf{z}}_{\mathrm{rx}} = \frac{\mathbf{r}_{\mathrm{sp}} - \mathbf{r}_{\mathrm{rx}}}{\left|\mathbf{r}_{\mathrm{sp}} - \mathbf{r}_{\mathrm{rx}}\right|} \tag{5.10a}$$

$$\hat{\mathbf{y}}_{\mathrm{rx}} = \frac{\hat{\mathbf{z}}_{\mathrm{grid}} \times \hat{\mathbf{z}}_{\mathrm{rx}}}{\left|\hat{\mathbf{z}}_{\mathrm{grid}} \times \hat{\mathbf{z}}_{\mathrm{rx}}\right|} \tag{5.10b}$$

$$\hat{\mathbf{x}}_{\mathrm{rx}} = \hat{\mathbf{y}}_{\mathrm{rx}} \times \hat{\mathbf{z}}_{\mathrm{rx}} \tag{5.10c}$$

The conversion from the grid CRS to the receiver CRS would here be defined as

$$R_{\text{grid}\to\text{rx}} = \begin{bmatrix} \hat{\mathbf{x}}_{\text{rx}} & \hat{\mathbf{y}}_{\text{rx}} & \hat{\mathbf{z}}_{\text{rx}} \end{bmatrix}^{\mathsf{T}} \tag{5.11}$$

5.5.6 Local Vectors

Because this section discusses communication between the grid CRS and the local CRS of individual facets k_1, we will temporarily make use of the subscript k_1 to help define the CRS rotations. Assuming the grid CRS, we can define the incoming and outgoing vectors and other relevant variables for calculating scattering using the NFM. For any arbitrary CRS, we define the incoming and outgoing vectors as

$$\hat{\mathbf{i}}^{-}_{k_1} = \frac{\mathbf{r}_{k_1} - \mathbf{r}_{\text{tx}}}{\left|\mathbf{r}_{k_1} - \mathbf{r}_{\text{tx}}\right|} \tag{5.12a}$$

$$\hat{\mathbf{o}}^{+}_{k_1} = \frac{\mathbf{r}_{\text{rx}} - \mathbf{r}_{k_1}}{\left|\mathbf{r}_{\text{rx}} - \mathbf{r}_{k_1}\right|} \tag{5.12b}$$

where the the subscripts of the position vector $\mathbf{r}$ indicate the transmitter (tx), receiver (rx), and the facet (k_1) positions in a specified CRS.

Assuming the grid CRS, each position along the ellipsoidal surface height is used to calculate a local facet. The local facet approximates the area of the region it rests upon whereas methods such as triangular meshing will perfectly align with the provided surface information. Assuming an equal-area projection, the local surface gradients along x- and y-directions are calculated as

$$\alpha_{k_1} = \frac{\partial}{\partial x} f_1(x_{k_1}, y_{k_1}) \tag{5.13a}$$

$$\beta_{k_1} = \frac{\partial}{\partial y} f_1(x_{k_1}, y_{k_1}) \tag{5.13b}$$

The local surface normal is calculated following [54, Chapter 11]

$$\hat{\mathbf{n}}_{k_1} = \frac{\begin{bmatrix} -\alpha_{k_1} & -\beta_{k_1} & 1 \end{bmatrix}^\mathsf{T}}{\sqrt{\alpha_{k_1}^2 + \beta_{k_1}^2 + 1}} \tag{5.14}$$

The local x and y unit vectors can then be calculated as

$$\hat{\mathbf{x}}_{k_1} = \frac{\begin{bmatrix} 1 & 0 & \alpha_{k_1} \end{bmatrix}^\mathsf{T}}{\sqrt{1 + \alpha_{k_1}^2}} \tag{5.15a}$$

$$\hat{\mathbf{y}}_{k_1} = \frac{\begin{bmatrix} 0 & 1 & \beta_{k_1} \end{bmatrix}^\mathsf{T}}{\sqrt{1 + \beta_{k_1}^2}} \tag{5.15b}$$

The rotation from the grid CRS to the local frame is then

$$R_{\text{grid}\to k_1} = \begin{bmatrix} \hat{\mathbf{x}}_{k_1} & \hat{\mathbf{y}}_{k_1} & \hat{\mathbf{n}}_{k_1} \end{bmatrix}^\mathsf{T} \tag{5.16}$$

The calculation of the local incidence and scattering angles is CRS independent if the unit vectors represent the same object. We can define the arbitrary angles between two CRS denoted A and B as

$$\theta = \arccos(\hat{\mathbf{z}}_A \cdot \hat{\mathbf{z}}_B) \tag{5.17a}$$

$$\phi = \arctan(\frac{\hat{\mathbf{y}}_A \cdot \hat{\mathbf{y}}_B}{\hat{\mathbf{x}}_A \cdot \hat{\mathbf{x}}_B}) \tag{5.17b}$$

The local incidence angles are, therefore, calculated assuming CRS A is the grid CRS and CRS B are the facet unit vectors given by $\hat{\mathbf{x}}_{k_1}$, $\hat{\mathbf{y}}_{k_1}$, and $\hat{\mathbf{z}}_{k_1}$ which are written with respect to the grid CRS.

5.5.7 Gravitational Offset

In some applications, it is helpful to know the direction of gravity. For example, plants tend to feature geotropism which is the growth of the plant towards or away from the direction of gravity. As subsequent operations are defined relative to a local facet with no ECEF information available, calculation of the gravitational off-axis angle should be performed in this module.

Assuming that gravity is oriented towards the earth center, we define the gravitational unit vector for a given facet as

$$\hat{\mathbf{g}} = \frac{\mathbf{r}_{\text{earth center}} - \mathbf{r}_{k_1}}{\left|\mathbf{r}_{\text{earth center}} - \mathbf{r}_{k_1}\right|} \tag{5.18}$$

We can then define the local gravitational off axis angle for a given facet as

$$\theta_g = \arccos(-\hat{\mathbf{g}} \cdot \ \hat{\mathbf{n}}_{k_1}) \tag{5.19}$$

5.6 Data Mapping Module

We will briefly explain the motivation for using class-based data mapping, or DSSs, in order to describe data. Let us consider an arbitrary problem of mapping a subset of data S from the total data space X onto a prediction space Y using a function $f(S)$. Suppose further that there were N

total dataspaces from $[X_1, X_2, \cdots, X_N]$ where a subset from each dataspace could result in a more accurate prediction value. Given that validating the prediction space is difficult, there is no single solution to this problem. This is depicted in an arbitrary format in Figure 5.7.

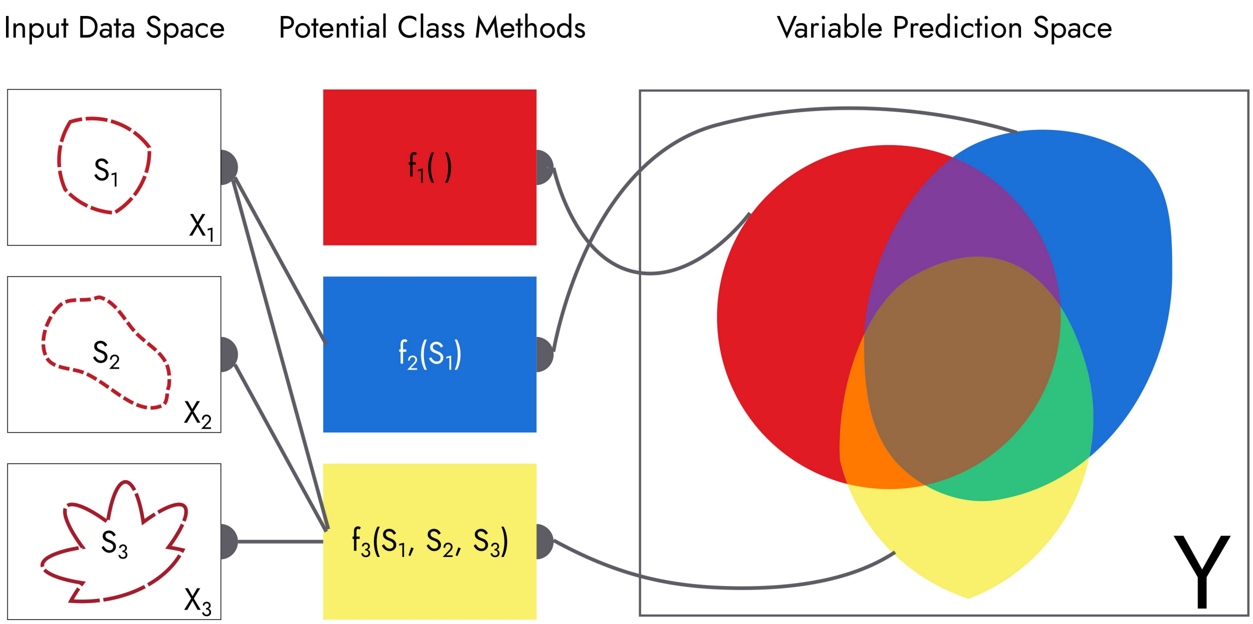

Figure 5.7

Data mapping concept for an arbitrary case. The output space Y is color-coded to show where the prediction space of the three different prediction methods will overlap.

Three different variable spaces and three different prediction classes are depicted in Figure 5.7. The subsets of the total dataspace are depicted in the left column. The function mapping for the three different methods are color-coded to visualize overlap in the image on the right. Note that the different methods do not use the same inputs. For example, the function $f_1()$ takes no input, and its output can be considered a random mapping over the dataspace Y. The other methods take different numbers of inputs and predict values for different portions of the dataspace.

To make this abstract concept more tangible, let us consider the prediction of the complex dielectric constant for soil. Generally, dielectric functions are either purely empirical or semi-empirical and are, thus, at risk of being biased by the measurement location or system noise. In Figure 5.8, the three variables depicted are soil moisture m_v, soil clay ratio s_c, and soil sand ratio s_s. Three different methods are used to estimate the complex soil dielectric in the right image. Some functions, such as the Mironov model [78], only require the soil clay ratio in their prediction of the complex dielectric. Note that this visualization does not represent any specific bound on the prediction space of soil dielectric and is only used for illustrating the concept of using multiple classes for variable prediction.

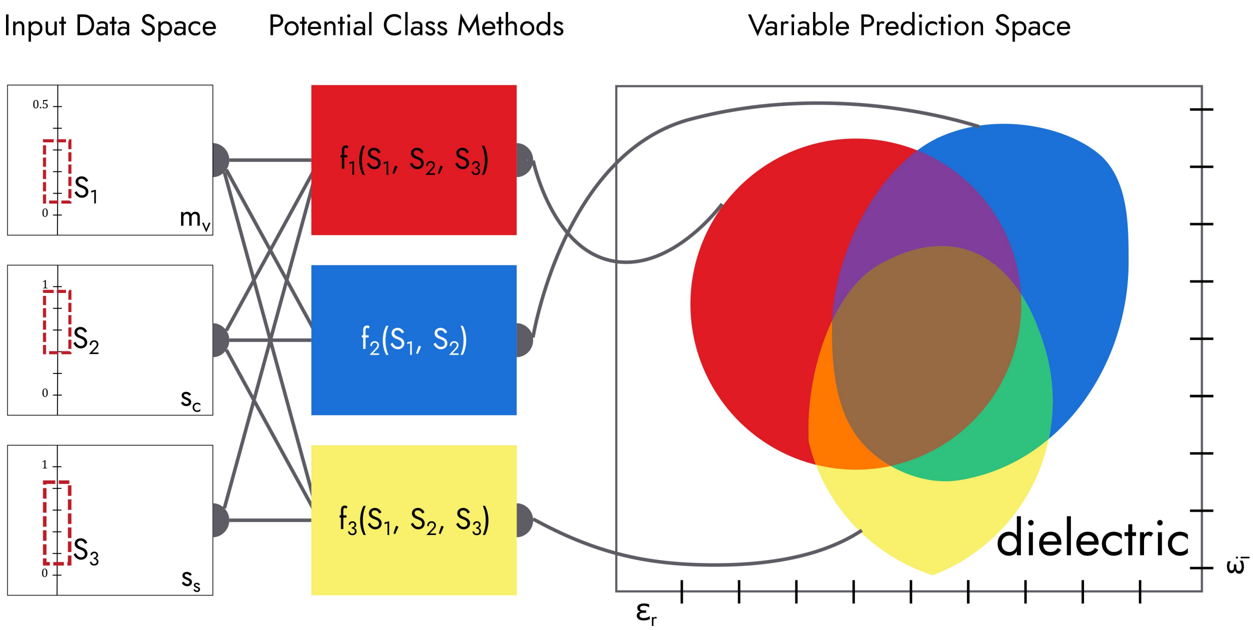

Figure 5.8

Data mapping concept using the example of soil dielectric. Three different methods are shown which map soil moisture m_v, soil clay fraction s_c, and soil sand fraction s_s to a complex dielectric constant. Overlapping prediction spaces are color coded.

The benefit of this can be summarized as follows: the SCoBi model is capable of assigning different DSS classification models to determine unknown variables such as vegetation structure, microwave soil parameters, and intermediate surface roughness. Each model can be fed the same number of inputs in determining their respective values, but not all of the function maps will require data. This style of programming allows for quick interchanging of variable predicting DSS.

The datasets which this model collects and uses are summarized.

5.6.1 Datasets and Workflows

While the user can define their own DSS and even provide their own datasets by using this module, the current baseline for this model calculates many different values in order to build the scattering matrix calculated in the following section.

Generally, if the size of the facet described by the DEM surface in $f_1(x, y)$ is more coarse than the resolution of the dataset provided, the dataset is then interpolated for each facet. For example, if a water body mask is applied at 10-meter resolution for a 30-meter resolution facet, a resulting 3×3 matrix of water body values is used. At present, the mode of this matrix is used to represent the entire matrix.

Water body masking is performed using the European Commission Joint Research Centre Global Waterbody (JRC GWB) dataset [89]. This dataset is provided at 0.00025° resolution or approximately 30-meter resolution. This information can nominally be used to describe the presence of inland water bodies.

Soil texture information is provided through the Soil Grids dataset [97]. The soil texture information is a machine-learning data product that is rendered at 250-meter resolution. There are many data products for this set across a large portion of the soil profile. In this model, we determine the soil texture in the upper portion of the profile and assume it is constant for any given simulation.

Other information is left to the user to provide. For example, given the high spatiotemporal variability, the user is expected to provide their own datasets for SM mapping. While we note that this could be done, for example, through a lookup table for a dataset such as SMAP, most validation journal papers assume a constant SM value for a very large region in the assumption that the change in topography will provide the expected shape of the resultant DDM.

This module constructs an object which operates on each DEM facet: an object for soil parameters, an object for intermediate roughness, and an object for vegetation. For the soil parameters, the class can be constructed in any way as long as the effective dielectric of the soil is returned. For the intermediate roughness, an arbitrary number of inputs can be provided assuming that a 3D, Cartesian surface is generated. For the vegetation class, a description of the vegetation parameters should be generated which aligns with the definitions of vegetation provided in [40, 65].

5.7 Scattering Module

The scattering module is responsible for realizing the linearly polarized scattering matrix used in equation 5.1. It is designed to compute the scattering matrix with efficiency given the size of the problem.

Using the output of the manager module, the scattering module chooses to evaluate both bare and vegetated scattering matrices using either CPU or GPU resources. The manager module, having determined the number of available CPU cores, can evaluate the scattering matrices for each facet in parallel.

5.7.1 Bare

The implementation for bare surfaces are thoroughly detailed in Chapter IV. To briefly summarize, child surfaces of intermediate roughness scale $f_2(x, y)$ are generated over a parent surface $f_1(x, y)$. The scattering is calculated according to a 3-scale NFM where the microwave roughness scale $f_3(x, y)$ is calculated using the attenuated field observed by the physical optics solution to a Gaussian distributed microwave roughness. Methods for using geometrical optics (GO) and direct numerical integration of the KA (DI-KA) are available, but have not been made parallelizable as of yet.

5.7.2 Vegetation

The vegetation scattering assumed by the spaceborne model is a simplified variant of what is found in [65]. Much like the surface scattering module, this calculation is simplified by means of the parallel ray approximation. In the scenario where transmitter or receiver are near the scatterer, the image method can be used to quickly determine attenuation along the path of least time. However, when the transmitter and receiver are of sufficient distance, each scatterer within the medium will have approximately identical incoming and outgoing vectors. Additionally, the unit vectors of the image media (e.g., [65, Figure 4]) will be near identical aside from a reversed z-axis direction. In summary, the use of an image media is made unnecessary.

The scattering amplitude matrix is computed for four scattering mechanisms. The shorthand for these contributions are noted by the letters dd, dr, rd, and rr. Following standard microwave theory notation, the 1st subscripts indicate the receiving port and the second subscript indicates a transmitted port. A character of d indicates that the signal travels directly to or from a scatterer. A character of r indicates that the signal is reflected by the ground surface on its travel to or from the scatterer. The four scattering mechanisms correspond to (1.) single bounce contributions (dd), (2.) double bounce contributions (dr and rd), and (3.) triple bounce contributions (rr). The scattering matrix for each element is then calculated for a given scatterer type α and scatterer instance n as

$$\underline{\underline{s}}_{\alpha,n}^{dd}(\hat{\mathbf{o}}^{+}, \hat{\mathbf{i}}^{-}) = \underline{\underline{t}}(\hat{\mathbf{o}}^{+}) \cdot \underline{\underline{f}}_{\alpha}(\hat{\mathbf{o}}_{\alpha}^{+}, \hat{\mathbf{i}}_{\alpha}^{-}; \beta_{\alpha,n}) \cdot \underline{\underline{t}}(\hat{\mathbf{i}}^{-}) \tag{5.20a}$$

$$\underline{\underline{s}}_{\alpha,n}^{dr}(\hat{\mathbf{o}}^{+}, \hat{\mathbf{i}}^{+}) = \underline{\underline{t}}(\hat{\mathbf{o}}^{+}) \cdot \underline{\underline{f}}_{\alpha}(\hat{\mathbf{o}}_{\alpha}^{+}, \hat{\mathbf{i}}_{\alpha}^{+}; \beta_{\alpha,n}) \cdot \underline{\underline{r}}_{g}(\hat{\mathbf{i}}^{+}) \cdot \underline{\underline{t}}(\hat{\mathbf{i}}^{+}) \tag{5.20b}$$

$$\underline{\underline{s}}_{\alpha,n}^{rd}(\hat{\mathbf{o}}^{-}, \hat{\mathbf{i}}^{-}) = \underline{\underline{t}}(\hat{\mathbf{o}}^{-}) \cdot \underline{\underline{r}}_{g}(\hat{\mathbf{o}}^{-}) \cdot \underline{\underline{f}}_{\alpha}(\hat{\mathbf{o}}_{\alpha}^{-}, \hat{\mathbf{i}}_{\alpha}^{-}; \beta_{\alpha,n}) \cdot \underline{\underline{t}}(\hat{\mathbf{i}}^{-}) \tag{5.20c}$$

$$\underline{\underline{s}}_{\alpha,n}^{rr}(\hat{\mathbf{o}}^{-}, \hat{\mathbf{i}}^{+}) = \underline{\underline{t}}(\hat{\mathbf{o}}^{-}) \cdot \underline{\underline{r}}_{g}(\hat{\mathbf{o}}^{-}) \cdot \underline{\underline{f}}_{\alpha}(\hat{\mathbf{o}}_{\alpha}^{-}, \hat{\mathbf{i}}_{\alpha}^{+}; \beta_{\alpha,n}) \cdot \underline{\underline{r}}_{g}(\hat{\mathbf{i}}^{+}) \cdot \underline{\underline{t}}(\hat{\mathbf{i}}^{+}) \tag{5.20d}$$

where $\underline{\underline{t}}$ indicates the attenuating vegetation medium given by [65, equation 8.a], and the ground reflection matrix is given by [65, equation 9.a]. The scattering amplitude matrix $\underline{\underline{f}}_{\alpha}$ is calculated for the given particle type α. Currently, this is programmed to be the scattering of simple geometries such as dielectric cylinders [104] and discs [71]. These functions were previously open-sourced in [40]. The four scattering mechanisms of equation 5.20 and the incoming and outgoing unit vectors are depicted in Figure 5.9

The model does not currently perform Monte Carlo averaging to determine an incoherent expression. We maintain phase information within this medium by incorporating the phase factor of equation 4.22 as

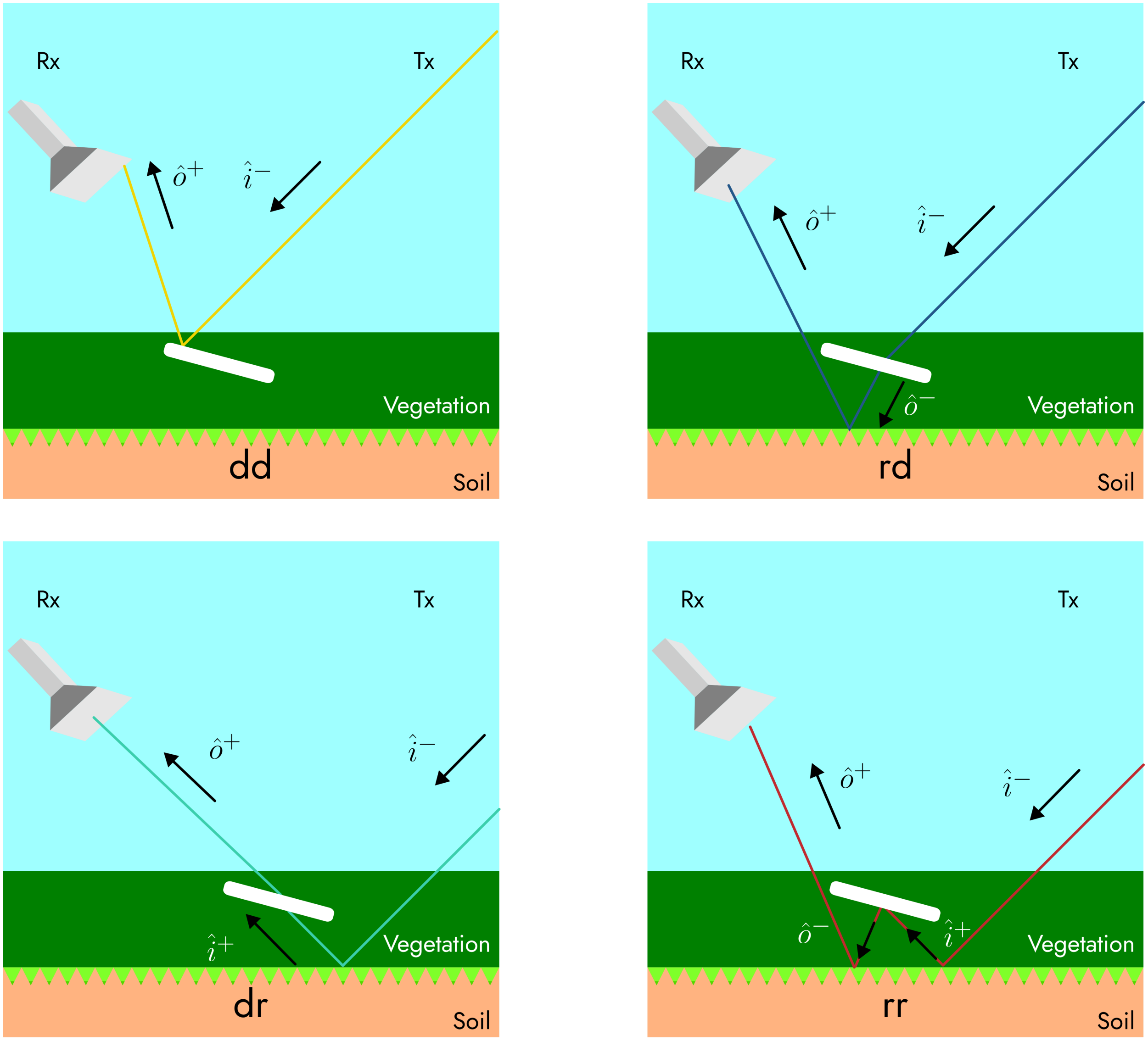

Figure 5.9

Scattering mechanisms found in the vegetation module representing single, double, and triple bounce mechanisms with respect to ground reflections.

$$\omega_{\alpha,n} = \exp\left(ik_0(\hat{\mathbf{i}}^- \cdot \mathbf{r}_{\alpha,n} - \hat{\mathbf{o}}^+ \cdot \mathbf{r}_{\alpha,n})\right) \tag{5.21}$$

where $\mathbf{r}$ is the range from the center of the facet CRS to the particle

Because the incoming and outgoing vectors are considered constant for each particle within the medium, the incoherent expression in [65, equation 12] can be simplified to estimate a scattering matrix for an entire forest scene. This can be expressed as

$$\underline{\underline{s}}^{\text{veg}}(\hat{\mathbf{o}}^{+}, \hat{\mathbf{i}}^{-}) = \sum_{\alpha} \sum_{n=1}^{N_\alpha} \left[\underline{\underline{s}}^{dd}_{\alpha,n} + \underline{\underline{s}}^{dr}_{\alpha,n} + \underline{\underline{s}}^{dd}_{\alpha,n} + \underline{\underline{s}}^{rr}_{\alpha,n} \right] \omega_{\alpha,n} \tag{5.22}$$

This expression can then be inserted into equation 5.1 to determine coherent signal scattering. Given the large area simulated in SoOp applications, the number of facets is presently considered sufficiently randomized.

5.7.3 Practical Considerations

While we are capable of determining scattering from any given number of particles, simulation studies observe that the primary contribution of dielectric discs for SoOp wavelengths generally contributes to the signal attenuation of the transmissivity matrices found in equation 5.20. As such, leaves are considered in the Foldy-Lax approximation of the transmissivity matrix (see [65, equation 8.b]), but they are not factored into the scattering mechanisms.

Given the large number of unknowns, validation of the modified vegetation module's system response requires careful consideration. This will likely be the topic of a future publication as strategies for understanding the impact of vegetation distribution at SoOp scales merits investigation.

5.8 DDM Module

The DDM produced by this module is evaluated using the cross-correlation approximation of [136, equation 22] under the assumption that the approximations used by GPS hold true for any given SoOp system. This process is effectively a matched filtering process which accounts for both time delays and Doppler offsets. The process is well defined by [56, equation 2.3 - 2.11] and is as summarized as follows. Let us loosely define the signal measured by the DDM instrument using [135, equation 16].

$$w(t', f') = \frac{A}{T_c} \int_0^{T_i} c(t-\tau)c(t-t')exp(-i2\pi(f + f_D - f')t)dt' + n_w \tag{5.23}$$

where

A is the amplitude of the received signal

T_c is the coherent integration time in seconds

$c(t-\tau)$ is the measured signal code at time t with propagation offset τ

$c(t-t')$ is the code replica at time t with the DDM instrument's time offset t'

f is the carrier frequency

f_D is the Doppler of the measured signal

f' is the DDM instruments test Doppler

This formulation assumes that the transmitted signal consists of a carrier frequency delivering a message, multiplied by a chip sequence, and buried in additive thermal noise. We assume that the chip sequence of the signal is significantly shorter than the data message such that the data message can be considered constant for the coherent integration time of the cross-correlation process. If we assume that the chip correlation process is time invariant and is primarily a function of the delay offset, we can remove it from the integration process by determining its expectation. This leaves the evaluation of the exponential term. Thus,

$$w(t', f') = A \langle c(t-\tau)c(t-t') \rangle \frac{1}{T_c} \int_0^{T_c} exp(-i2\pi(f + f_D - f')t)dt' + n_w \tag{5.24}$$

We then approximate the expectation of the cross-correlation at time-lag $\tau = 0$ as a triangle function where

$$\Lambda(t-t') = \langle c(t)c(t-t')\rangle = \begin{cases} 1 - \dfrac{|t-t'|}{\tau_c} & |\dfrac{|t-t'|}{\tau_c}| < 1 \\ 0 & |\dfrac{|t-t'|}{\tau_c}| \geq 1 \end{cases} \tag{5.25}$$

where τ_c is the chip rate of the code sequence. The exponential of the integration period can then be evaluated as

$$\begin{aligned} S(f_D - f') &= \frac{1}{T_c}\int_0^{T_c} \exp(-i2\pi(f + f_D - f')t)dt' \\ &= \operatorname{sinc}(\pi T_c(f_D - f'))\exp(-\pi i T_c(f_D - f')) \end{aligned} \tag{5.26}$$

The total integration period is then approximated by

$$w(t', f') = A\Lambda(t-t')S(f_D - f') + n_w \tag{5.27}$$

Which finally provides the ambiguity function as

$$\chi(t-t', f_D - f') = \Lambda(t-t')S(f_D - f') \tag{5.28}$$

We note that this function can be considered coherent under this formulation. The DDM is evaluated in SCoBi by assuming that the amplitude of the signal A is equal to the simulated 2×1 received field $\underline{b}$. This yields

$$w(t', f') = \underline{b}_{k_1}\Lambda(t-t')S(f_D - f') + n_w \tag{5.29}$$

The complex DDM is then constructed by summing the total, coherent field for each delay (t') and Doppler (f') value within the DDM instrument's correlators after weighting with the ambiguity function χ. A complex DDM pixel is thus given by

$$\underline{b}(t - t', f_D - f') = \sum_{k_1=1}^{N_{k_1}} \underline{b}_{k_1} \chi(t - t', f_D - f') \tag{5.30}$$

It is common to eliminate the coherency of the DDM by averaging the signal over an incoherent integration time T_i. The number of DDMs collected over the incoherent integration time is given by the integer N_{DDMs}:

$$N_{\text{DDMs}} = \left\lfloor \frac{T_i}{T_{\text{coh}}} \right\rfloor \tag{5.31}$$

where the brackets indicate a flooring function. With this, the average power of the incoherently averaged DDMs can be computed as

$$\underline{P}(t - t', f_D - f') = \frac{1}{N_{\text{DDMs}}} \sum_{n=1}^{N_{\text{DDMs}}} \sum_{k_1=1}^{N_{k_1}} |\underline{b}_{k_1} \otimes \underline{b}^*_{k_1}| |\chi(t - t', f_D - f')|^2 \tag{5.32}$$

where $\otimes$ makes use of the Kronecker product, resulting in a 4×1 matrix of power values.

This form is readily converted into an effective normalized bistatic radar cross-section (NBRCS) value as

$$\underline{\sigma}^0(t - t', f_D - f') = \frac{1}{N_{\text{DDMs}}} \sum_{n=1}^{N_{\text{DDMs}}} \sum_{k_1=1}^{N_{k_1}} \underline{\sigma}_{0,k_1} |\chi(t - t', f_D - f')|^2 \tag{5.33}$$

where

$$\underline{\sigma}^0_{k_1} = \frac{4\pi r^2_{tk_1} r^2_{k_1 r}}{|K|^2 A_{k_1}} |b_{k_1} \otimes b^*_{k_1}| \tag{5.34}$$

where A_{k_1} is the area of facet k_1. Upon completion of this module, the manager module collects the desired output variable and stores them within an HDF5 file.

5.9 Conclusion

A summary of an end-to-end model is presented. Each module works together to describe land scattering from complex terrain. The end-to-end model is capable of simulating arbitrary SoOp systems or inherit parameters directly from current systems. The earth surface is generated about the specular point along the line connecting the transmitter, receiver, and specular point across the WGS84 ellipsoid. Once relevant bistatic geometry information is collected, global datasets are used to construct DSS objects which will assign SM, intermediate roughness scales, and vegetation structures at scales below the DEM spatial resolution. A simplified form of the SCoBi vegetation module is used to determine vegetation scattering while the NFM of Chapter IV is used to determine scattering over bare surfaces. A complex DDM is then calculated for the surface with an optional incoherent DDM output.

The model is currently undergoing validation with intention to open source the modules to the wider community. Once validation has been completed, the model is intended to explore concepts such as the variability of bistatic radar cross-section (BRCS) and DDMs to increasingly complex terrain. Additionally, the potential of root-zone soil moisture (RZSM) retrieval for SNOOPI-based configurations is of great interest. Comparisons of the model with available DDMs over bare and vegetated terrains are to be explored. Documentation which more completely describes the user-interface of the model will be published upon open sourcing.

CHAPTER VI

CONCLUSION AND DISCUSSION

6.1 Summary of Contributions

Some of this dissertation's relevant literature contributions can be summarized as follows:

1. An open-sourced multilayer, multifrequency tool kit for root-zone soil moisture (RZSM) remote sensing with signals of opportunity (SoOp).
2. A study on optimal SoOp configurations for RZSM retrieval
3. A generalized nested facet method (NFM) framework for multifrequency SoOp modeling of topography
4. A coherent model for spaceborne SoOp scattering capable of complex delay-Doppler map (DDM) generation

We expound on these points below.

In chapter II, we develop a multilayer model for RZSM analysis with several SoOp sources. Globally available ultra high frequency (UHF) signals provided by SoOp present an exciting opportunity to better sense variables such as soil moisture due to UHF signal's longer wavelengths and larger penetration depth. General claims about RZSM sensing capabilities revolve around the penetration depth estimation provided in [119, equation 4.12b] and equation 2.6. This chapter provides a thorough exploration of the change in the reflection coefficient with varying single- and multi-layer soil moisture profiles. A multilayer penetration depth applicable for oblique angles is evaluated and has been open-sourced.

Given the information from Chapter II, the expected retrieval performance is evaluated by the Cramer-Rao lower bound (CRLB) in Chapter III. Given five SoOp sources available between 137 and 2338 MHz, each combination of frequencies is evaluated for its minimum variance unbiased estimator over a simple two-layer profile given different depth configurations and soil moisture values. It is found that a pairing of one frequency above L-band and another at P-band or lower generally results in the optimal estimator for a given soil moisture profile combination.

As the previous chapters dealt with evaluating retrieval conditions for a small, localized area, Chapter IV develops an NFM based on the Kirchhoff approximation (KA) solution to the Stratton-Chu equation. This solution discretizes a surface into several parallelograms that determine scattering towards a receiver as the product of the total surface fields on a facet and its surface phase integral which functions as a reradiation pattern for the surface. As observed by [26, Figure 4.7], the reradiation produced by this surface phase integral is similar to a finite conducting plane struck by a plane wave. The NFM is found to be computationally tractable for SoOp applications and scalable to optimally compute scattering for any surface within the validity region of the KA.

With each component described, Chapter V describes a complete model for describing scattering using the NFM. The earth surface is modeled using a Digital Elevation Map (DEM) and the World Geological Survey 1984 (WGS84) geoid to determine the ellipsoidal height for a given area around a specular point. The NFM from the previous chapter is used to determine scattering over non-vegetated regions, and a simplified form of the vegetation model presented in [65] is used for scattering from vegetation canopies. Each module operates under a parallel-ray approximation for a local surface, and the total field is determined by polarization rotation and alignment with the transmitter and receiver antenna patterns. Class-based decision making is used to determine the intermediate surface roughness, dielectric, surface water body content, and vegetation.

This dissertation pursues the improvement of SoOp modeling in order to develop stronger SoOp remote sensing retrieval products and to better design future SoOp data collections, experiments, and missions. Naturally, there are many areas available for future exploration. The next and final section highlights further improvements that could be made to this modeling framework in order to improve remote sensing capabilities.

6.2 Future Work

The modeling framework presented is designed for simple integration with additional modules. As SoOp has many divisions of research, additional modules should strive to explore new components of SoOp remote sensing and investigate current questions on the applicability of SoOp retrievals. Here, we summarize our intended future additions to the SoOp coherent bistatic scattering model (SCoBi) model for ground and spaceborne remote sensing applications.

6.2.1 Surface Modeling

Modeling up to to this point has been represented by plane waves over slow-varying surfaces. There is a need in the hydrologic sciences to estimate water content in mountainous terrains due to the dependence of many areas on snowmelt and the impact of surface runoff. As the acquisition of sub-meter resolution DEM data continues, modeling tools have the opportunity to meet science demands. The inclusion of methods such as small-perturbation method and the advanced integral equation method could prove highly beneficial for ground and airborne simulations for areas of significant surface roughness [123].

6.2.2 Vegetation

The current SCoBi implementation makes use of the distorted-Borne approximation to estimate scattering from a uniformly distributed set of simplified scatterers. These layer-based scatterers are designed to determine the average response of a vegetation medium through Monte Carlo simulations of random scattering positions and are not fit to simulate specific scattering geometries. Adding flexibility for specific, fixed vegetation structures could prove useful. Different interpretations of vegetation realism are depicted in Figure 6.1.

Figure 6.1(a) represents a simple tree structure in the analogue world. All subsequent images are modeling represents of this image. A brute force method could consist of a dielectric meshing approach as seen in Figure 6.1(b). In this approach, either a surface mesh or a three-dimensional voxel representation of the scattering geometry can be used to determine scattering by numerical Maxwell solutions, method of moments, or other alternatives. Alternatively, simplifying the geometry of a vegetation canopy would produce significantly more efficient scattering amplitude calculations. Figure 6.1(c) simplifies (b) by representing the vegetation structure with dielectric cylinders and discs. An attenuating medium (represented by the green cloud surrounding tree) acts upon coherent and incoherent signals. The current ground-based formulation of SCoBi is depicted in Figure 6.1(d) where the geometry is broken into multiple dielectric layers corresponding to statistically significant scatterer regions. A scatterer density then determines random, uniform distribution of scatters throughout the medium to arrive at the solutions presented in [65]. Figure 6.1 (e) represents the proposed implementation for the spaceborne model. In this formulation, the contributions of leaves are excluded from the scattering solution but are incorporated into the

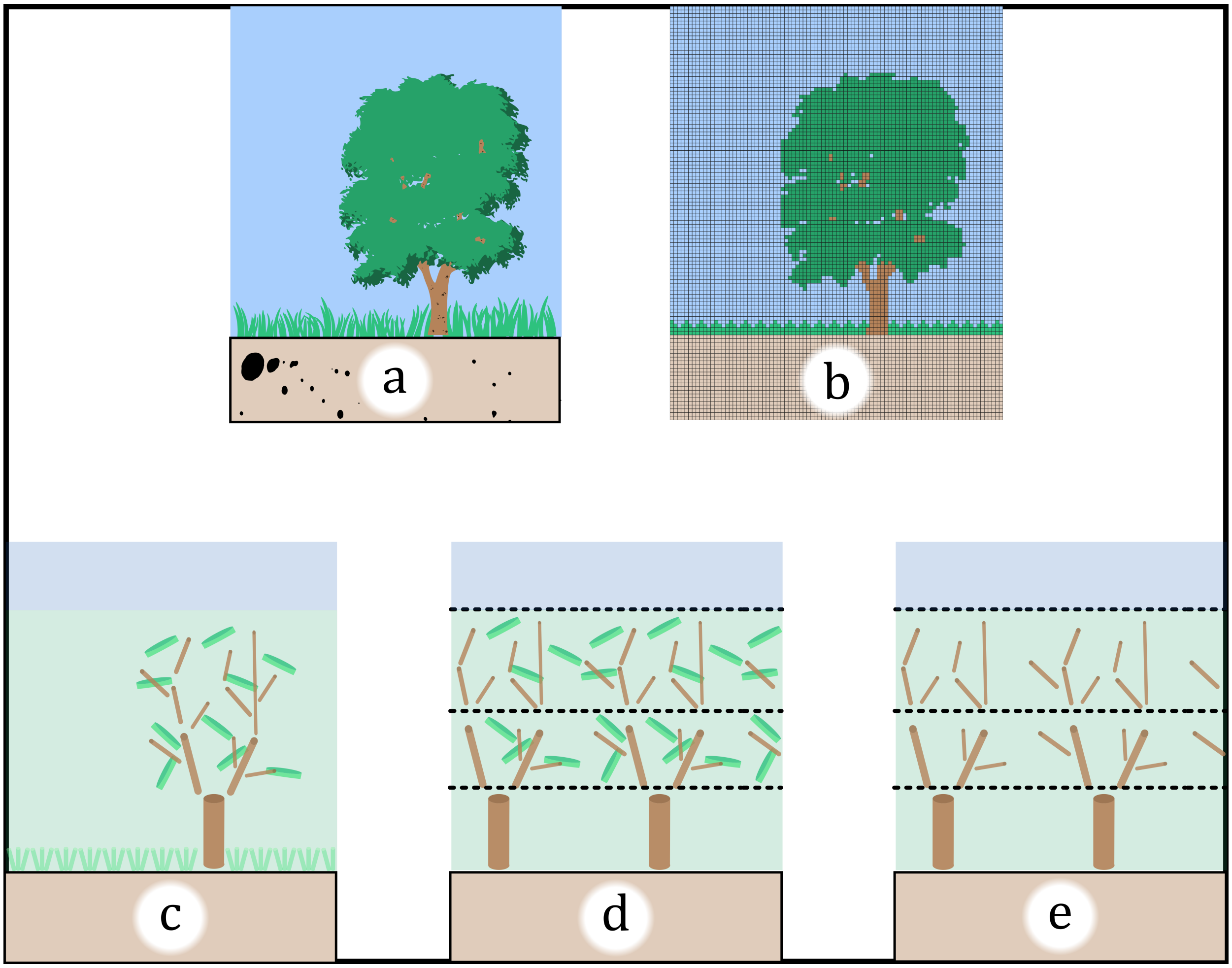

Figure 6.1

Different tree representations for electromagnetic modeling. (a) analogue / real world, (b) dielectric meshing for intensive numerical solutions, (c) simple geometric representation of scatterers in attenuating medium, (d) uniformly distributed scatterers in discrete multilayer structure, (e) disc-less scatterers in attenuated medium

effective vegetation medium as the primary effect of leaves on SoOp wavelengths is generally attenuation.

6.2.3 Other Modules

6.2.3.1 Ionosphere Effects

Ionospheric scattering and polarization rotation is stronger at UHF than L-band [127]. As P-band signals operate in a very active portion of the RF spectrum, modeling losses for P-band signals is important to assess noise contributions. The addition of an ionospheric module [80] to SCoBi could prove highly beneficial for P-band simulations. We note that because the ionosphere varies across space and time, this module will require either space and time as inputs or an assumed ”average” ionospheric effect for arbitrary simulations.

6.2.3.2 Additional Surface Models

The current SCoBi modules account for contributions from bare soil and vegetated areas. Several natural surfaces are currently left unaccounted. Of primary interest are the impacts of (1) water bodies, (2) wetlands, (3) snow, and (4) permafrost.

With respect to water bodies, we intend to build a module that will account for water-body scattering. The current spaceborne module determines the if a given facet is dominantly occupied by determining the facet’s surface water fraction through the European Commission Joint Research Centre Global Waterbody (JRC GWB). Our initial formulation assumes that the waterbody does not contribute any scattering by assuming that the specularly scattered signal is not aligned with the receiver. This could be easily corrected by using the facet’s halfway vector (equation 4.8) to determine if the facet is within a quasi-specular reflection regime. The reflecting facet would then use a dielectric representation of a surface waterbody. The inclusion of surface waterbody roughness would be beyond the scope of spaceborne simulations and would, therefore, be considered flat as a first approximation. As the facet size would be quite large for DEM resolutions (e.g., 30-meters total), the surface reradiation pattern will likely serve as a delta function for most frequencies and, therefore, reject most signals that are not specularly aligned. In a similar effort, the impact of partially wet topography is of great interest for wetland-based SoOp applications [81]. A volume fraction model for dielectric (e.g., [119, equation 4.73]) or for the total scattering coefficient [69, equation 1] could be used to estimate coherent and incoherent scattering respectively.

SoOp scattering over snow is of great interest for remote sensing applications [106]. The addition of a snow dielectric model is rather trivial. Additionally, the limited variability of relative permittivity (e.g., approximately $\varepsilon\prime \in [1, 3]$) will cause limited change in scattering. The primary complexity of SoOp snow modeling will likely be the provision of a consistent phase reference in order to estimate snow water equivalent through phase unwrapping techniques. The inclusion of permafrost simulations, however, will likely require careful modeling due to the variability of the relative permittivity as well as the position of active and frozen soil layers [20].

6.2.4 Open-Sourcing

The model presented in this dissertation is intended for open-sourcing in the near future. We will determine an appropriate open-source copyright while adhering to the respective copyright of any open-source model constituents used. The greatest difficulty lies in providing general access to large datasets. For ease of use, we may create programs that collect data from web servers for the users. Additionally, the model may be ported away from a proprietary programming language for more accessible user base.

REFERENCES

[1] "FCC Online Table of Frequency Allocations,", Jul 2022.

[2] M. M. Al-Khaldi, J. T. Johnson, A. J. O'Brien, A. Balenzano, and F. Mattia, "Time-series retrieval of soil moisture using CYGNSS," *IEEE Transactions on Geoscience and Remote Sensing*, vol. 57, no. 7, 2019, pp. 4322–4331.

[3] E. Babaeian, M. Sadeghi, S. B. Jones, C. Montzka, H. Vereecken, and M. Tuller, *Ground, proximal, and satellite remote sensing of soil moisture*, 2019.

[4] Board and Space Studies and National Academies of Sciences, Engineering, and Medicine, *Thriving on Our Changing Planet*, National Academies Press, Washington, D.C., Dec 2018.

[5] J. Boisvert, Q. Gwyn, B. Brisco, D. Major, and R. Brown, "Evaluation of soil moisture estimation techniques and microwave penetration depth for radar applications," *Canadian journal of remote sensing*, vol. 21, no. 2, 1995, pp. 110–123.

[6] M. Born and E. Wolf, *Principles of optics: electromagnetic theory of propagation, interference and diffraction of light*, Elsevier, 2013.

[7] D. Boyd and M. Kurum, "A Nested Facet Method of the Kirchhoff Approximation for Large-Scale Land Scattering," 2023.

[8] D. Boyd, M. Kurum, O. Eroglu, A. C. Gurbuz, J. L. Garrison, B. R. Nold, M. A. Vega, J. R. Piepmeier, and R. Bindlish, "SCoBi Multilayer: A Signals of Opportunity Reflectometry Model for Multilayer Dielectric Reflections," *Remote Sensing*, vol. 12, no. 21, 2020, pp. 1–25.

[9] D. R. Boyd, A. C. Gurbuz, M. Kurum, J. L. Garrison, B. R. Nold, J. R. Piepmeier, M. Vega, and R. Bindlish, "Cramer–rao lower bound for soop-r-based root-zone soil moisture remote sensing," *IEEE journal of selected topics in applied earth observations and remote sensing*, vol. 13, 2020, pp. 6101–6114.

[10] D. R. Boyd, M. Kurum, O. Eroglu, A. C. Gurbuz, J. Garrison, B. Nold, J. Piepmeier, M. Vega, and R. Bindlish, "Investigation of Root-Zone Soil Moisture Profile Sensitivity to Multiple Signals of Opportunity Sources," *Proc. 2019 Usn. Natl. Radio Sci. Meet.*, Boulder, Colorado, 2019, p. 170.

[11] D. R. Boyd, M. Kurum, O. Eroglu, A. C. Gurbuz, J. L. Garrison, B. Nold, J. Piepmeier, M. S. Vega, and R. Bindlish, "SCoBi Multilayer: a signals of opportunity reflectometry model for multilayer dielectric reflections," *Remote Sensing*, vol. 13, 2020, pp. 6101–6114, in review.

[12] K. L. Brodie, B. L. Bruder, R. K. Slocum, and N. J. Spore, "Simultaneous Mapping of Coastal Topography and Bathymetry From a Lightweight Multicamera UAS," *IEEE Transactions on Geoscience and Remote Sensing*, vol. 57, no. 9, sep 2019, pp. 6844–6864.

[13] L. Bruckler, H. Witono, and P. Stengel, "Near surface soil moisture estimation from microwave measurements," *Remote Sensing of Environment*, vol. 26, no. 2, 1988, pp. 101–121.

[14] J. D. Campbell, R. Akbar, A. Bringer, D. Comite, L. Dente, S. T. Gleason, L. Guerriero, E. Hodges, J. T. Johnson, S.-B. Kim, et al., "Intercomparison of electromagnetic scattering models for delay-Doppler maps along a CYGNSS land track with topography," *IEEE Transactions on Geoscience and Remote Sensing*, vol. 60, 2022, pp. 1–13.

[15] J. D. Campbell, A. Melebari, and M. Moghaddam, "Modeling the Effects of Topography on Delay-Doppler Maps," *IEEE Journal of Selected Topics in Applied Earth Observations and Remote Sensing*, vol. 13, 2020, pp. 1740–1751.

[16] A. Camps, H. Park, Y. Kang, J. Barbosa, J. Bandeiras, P. Vieira, A. Friaças, and S. D'Addio, "SAIRPS: A generic simulator for evaluation of synthetic aperture interferometric radiometers," *2013 IEEE International Geoscience and Remote Sensing Symposium-IGARSS*. IEEE, 2013, pp. 1936–1939.

[17] J. M. Carreiras, S. Quegan, T. Le Toan, D. H. T. Minh, S. S. Saatchi, N. Carvalhais, M. Reichstein, and K. Scipal, "Coverage of high biomass forests by the ESA BIOMASS mission under defense restrictions," *Remote Sensing of Environment*, vol. 196, 2017, pp. 154–162.

[18] I. Champion and R. Faivre, "Sensitivity of the radar signal to soil moisture: variation with incidence angle, frequency, and polarization," *IEEE Trans. Geosci. Remote Sens.*, vol. 35, no. 3, 1997, pp. 781–783.

[19] E. Chapin, A. Chau, J. Chen, B. Heavey, S. Hensley, Y. Lou, R. Machuzak, and M. Moghaddam, "AirMOSS: An airborne P-band SAR to measure root-zone soil moisture," *IEEE Natl. Radar Conf. - Proc.*, 2012, pp. 0693–0698.

[20] R. H. Chen, A. Tabatabaeenejad, and M. Moghaddam, "Analysis of permafrost active layer soil heterogeneity in support of radar retrievals," *IGARSS 2018-2018 IEEE International Geoscience and Remote Sensing Symposium*. IEEE, 2018, pp. 8559–8562.

[21] C. Chew and E. Small, "Description of the UCAR/CU Soil Moisture Product," *Remote Sensing*, vol. 12, no. 10, 2020, p. 1558.

[22] C. Chew, E. Small, and H. Huelsing, "Flooding and inundation maps using interpolated CYGNSS reflectivity observations," *Remote Sensing of Environment*, vol. 293, 2023, p. 113598.

[23] C. C. Chew and E. E. Small, "Soil Moisture Sensing Using Spaceborne GNSS Reflections: Comparison of CYGNSS Reflectivity to SMAP Soil Moisture," *Geophys. Res. Lett.*, vol. 45, no. 9, 2018, pp. 4049–4057.

[24] C. C. Chew, E. E. Small, K. M. Larson, and V. U. Zavorotny, "Effects of near-surface soil moisture on GPS SNR data: Development of a retrieval algorithm for soil moisture," *IEEE Trans. Geosci. Remote Sens.*, vol. 52, no. 1, 2014, pp. 537–543.

[25] B. Choudhury, T. J. Schmugge, A. Chang, and R. Newton, "Effect of surface roughness on the microwave emission from soils," *Journal of Geophysical Research: Oceans*, vol. 84, no. C9, 1979, pp. 5699–5706.

[26] M. P. Clarizia, *Investigating the Effect of Ocean Waves on GNSS-R Microwave Remote Sensing Measurements*, doctoral dissertation, University of Southampton, 2012.

[27] M. P. Clarizia, C. Gommenginger, M. Di Bisceglie, C. Galdi, and M. A. Srokosz, "Simulation of L-band bistatic returns from the ocean surface: A facet approach with application to ocean GNSS reflectometry," *IEEE Transactions on Geoscience and Remote Sensing*, vol. 50, no. 3, 2011, pp. 960–971.

[28] M. P. Clarizia, N. Pierdicca, F. Costantini, and N. Floury, "Analysis of CYGNSS data for soil moisture retrieval," *IEEE J. Sel. Top. Appl. Earth Obs. Remote Sens.*, vol. 12, no. 7, 2019, pp. 2227–2235.

[29] I. Cobelo, K. B. Machado, A. C. M. David, P. Carvalho, M. E. Ferreira, and J. C. Nabout, "Unmanned aerial vehicles and low-cost sensor as tools for monitoring freshwater chlorophyll-a in mesocosms with different trophic state," *International Journal of Environmental Science and Technology*, jul 2022.

[30] D. Comite and N. Pierdicca, "Bistatic radar systems at large baselines for ocean observation," *IEEE Transactions on Geoscience and Remote Sensing*, vol. 56, no. 3, 2017, pp. 1816–1828.

[31] D. Comite, F. Ticconi, L. Dente, L. Guerriero, and N. Pierdicca, "Bistatic coherent scattering from rough soils with application to GNSS reflectometry," *IEEE Transactions on Geoscience and Remote Sensing*, vol. 58, no. 1, 2019, pp. 612–625.

[32] D. Comite, F. Ticconi, L. Dente, L. Guerriero, and N. Pierdicca, "Bistatic coherent scattering from rough soils with application to GNSS reflectometry," *IEEE Transactions on Geoscience and Remote Sensing*, vol. 58, no. 1, 2020, pp. 1–14.

[33] L. Dente, L. Guerriero, D. Comite, and N. Pierdicca, "Space-Borne GNSS-R Signal over a Complex Topography: Modeling and Validation," *IEEE J. Sel. Top. Appl. Earth Obs. Remote Sens.*, vol. 13, 2020, pp. 1218–1233.

[34] L. Dente, L. Guerriero, D. Comite, and N. Pierdicca, "Space-Borne GNSS-R Signal Over a Complex Topography: Modeling and Validation," *IEEE Journal of Selected Topics in Applied Earth Observations and Remote Sensing*, vol. 13, 2020, pp. 1218–1233.

[35] M. C. Dobson, F. F. Ulaby, M. T. Hallikainen, and M. A. El-Rayes, "Microwave dielectric behavior of wet soil - Part II: Dielectric mixing models," *IEEE Trans. Geosci. Remote Sens.*, vol. 23, no. 1, 1985, pp. 35–46.

[36] M. C. Dobson, F. T. Ulaby, M. T. Hallikainen, and M. A. El-Rayes, "Microwave dielectric behavior of wet soil-Part II: Dielectric mixing models," *IEEE Transactions on geoscience and remote sensing*, , no. 1, 1985, pp. 35–46.

[37] X. Duan and M. Moghaddam, "Bistatic vector 3-D scattering from layered rough surfaces using stabilized extended boundary condition method," *IEEE Trans. Geosci. Remote Sens.*, vol. 51, no. 5, 2013, pp. 2722–2733.

[38] O. Eroglu, D. R. Boyd, and M. Kurum, "SCoBi: a free, open-source, SoOp coherent bistatic scattering simulator framework," *Geosci. Remote Sens. Symp.*, 2018, pp. 1–12.

[39] O. Eroglu, D. R. Boyd, and M. Kurum, "SCoBi User's Manual,", 2018.

[40] O. Eroglu, D. R. Boyd, and M. Kurum, "The Signals of Opportunity Coherent Bistatic Scattering Simulator: A Free, Open Source Simulator Framework," *IEEE Geosci. Remote Sens. Mag.*, 2020.

[41] O. Eroglu, M. Kurum, and J. Ball, "Response of GNSS-R on Dynamic Vegetated Terrain Conditions," *IEEE J. Sel. Top. Appl. Earth Obs. Remote Sens.*, vol. 12, no. 5, may 2019, pp. 1599–1611.

[42] O. Eroglu, M. Kurum, D. Boyd, and A. C. Gurbuz, "High Spatio-Temporal Resolution CYGNSS Soil Moisture Estimates Using Artificial Neural Networks," *Remote Sens.*, vol. 11, no. 19, 2019, p. 2272.

[43] G. Franceschetti and D. Riccio, *Scattering, natural surfaces, and fractals*, Elsevier, 2006.

[44] J. Garrison, Y. C. Lin, B. Nold, J. R. Piepmeier, M. A. Vega, M. Fritts, C. F. Toit, and J. Knuble, "Remote sensing of soil moisture using P-band signals of opportunity (SoOp): Initial results," *Int. Geosci. Remote Sens. Symp.*, 2017, pp. 4158–4161.

[45] J. Garrison, J. Piepmeier, R. Shah, M. Vega, D. Spencer, R. Banting, C. Firman, B. Nold, K. Larsen, and R. Bindlish, "SNOOPI: A Technology Validation Mission for P-band Reflectometry using Signals of Opportunity," *IGARSS 2019-2019 IEEE International Geoscience and Remote Sensing Symposium*. IEEE, 2019, pp. 5082–5085.

[46] J. L. Garrison, S. J. Katzberg, and C. T. Howell, "Detection of ocean reflected GPS signals: theory and experiment," *Conf. Proc. - IEEE Southeast Con*, 1997, pp. 290–294.

[47] J. L. Garrison, M. Kurum, B. Nold, J. Piepmeier, M. A. Vega, R. Bindlish, G. Pignotti, and W. Lafayette, "Remote Sensing of Root-Zone Soil Moisture Using I- and P-band Signals of Opportunity: Instrument Validation Studies," *Int. Geosci. Remote Sens. Symp.*, Valencia, 2018, pp. 8305–8308.

[48] J. L. Garrison, J. Piepmeier, R. Shah, M. A. Vega, and D. A. Spencer, "SNOOPI : A Technology Validation Mission for P-band Reflectometry using Signals of Opportunity," *IGARSS 2019 - 2019 IEEE Int. Geosci. Remote Sens. Symp.*, , no. 1, 2019, pp. 5082–5085.

[49] J. L. Garrison, R. Shah, B. Nold, J. R. Mansell, M. A. Vega, J. C. Raymond, R. Bindlish, M. Kurum, J. Piepmeier, S. Kim, et al., "SNOOPI: Demonstrating P-band reflectometry from orbit," *2021 IEEE International Geoscience and Remote Sensing Symposium IGARSS*. IEEE, 2021, pp. 164–167.

[50] C. Gerekos, A. Tamponi, L. Carrer, D. Castelletti, M. Santoni, and L. Bruzzone, "A coherent multilayer simulator of radargrams acquired by radar sounder instruments," *IEEE Transactions on Geoscience and Remote Sensing*, vol. 56, no. 12, 2018, pp. 7388–7404.

[51] S. Gleason, *Remote sensing of ocean, ice and land surfaces using bistatically scattered GNSS signals from low earth orbit*, doctoral dissertation, 2006.

[52] W. Gu, H. Xu, and L. Tsang, "A numerical kirchhoff simulator for GNSS-R land applications," *Progress in Electromagnetics Research*, vol. 164, no. March, 2019, pp. 119–133.

[53] W. Gu, H. Xu, and L. Tsang, "A numerical kirchhoff simulator for GNSS-R land applications," *Progress in electromagnetics research*, vol. 164, 2019, pp. 119–133.

[54] B. K. Horn and R. W. Sjoberg, "Calculating the reflectance map," *Applied optics*, vol. 18, no. 11, 1979, pp. 1770–1779.

[55] D. W. Hosmer Jr, S. Lemeshow, and R. X. Sturdivant, *Applied logistic regression*, vol. 398, John Wiley & Sons, 2013.

[56] P. Jales, *Spaceborne Receiver Design for Scatterometric GNSS Reflectometry*, doctoral dissertation, 2012.

[57] J. T. Johnson, K. F. Warnick, and P. Xu, "On the geometrical optics (Hagfors' Law) and physical optics approximations for scattering from exponentially correlated surfaces," *IEEE Transactions on Geoscience and Remote Sensing*, vol. 45, no. 8, 2007, pp. 2619–2629.

[58] S. M. Kay, *Fundamentals of Statistical Signal Processing: Estimation Theory*, Prentice Hall PTR, Upper Saddle River, 1993.

[59] A. J. Kerr, *Theoretical performance bounds for the estimation of target parameters from electromagnetic induction data*, doctoral dissertation, Georgia Institute of Technology, 2020.

[60] S. Kim, J. Garrison, and M. Kurum, "Retrieval of Subsurface Soil Moisture and Vegetation Water Content from Multi-frequency SoOp-Reflectometry: Sensitivity Analysis," 2023.

[61] J. Knuble, J. Piepmeier, M. Deshpande, C. D. Toit, J. Garrison, Y. C. Lin, G. Stienne, S. Katzberg, and G. Alikakos, "Airborne P-band Signal of Opportunity (SoOP) demonstrator instrument; Status update," *2016 IEEE Int. Geosci. Remote Sens. Symp.*, 2016, pp. 5638–5641.

[62] A. Komanduru, "Remote sensing of snow using bistatic radar reflectometry," *Open Access Theses*, 2016.

[63] A. G. Konings, D. Entekhabi, M. Moghaddam, and S. S. Saatchi, "The Effect of a Variable Soil Moisture Profile on P-band Backscatter Estimation," *IEEE Trans. Geosci. Remote Sens.*, vol. 52, no. 10, 2014, pp. 6315–6325.

[64] C. H. Kuo and M. Moghaddam, "Electromagnetic scattering from multilayer rough surfaces with arbitrary dielectric profiles for remote sensing of subsurface soil moisture," *IEEE Antennas Propag. Soc. AP-S Int. Symp.*, vol. 45, no. 2, 2007, pp. 4797–4800.

[65] M. Kurum, M. Deshpande, A. T. Joseph, P. E. O'Neill, R. H. Lang, and O. Eroglu, "SCoBi-Veg: A generalized bistatic scattering model of reflectometry from vegetation for signals of opportunity applications," *IEEE Transactions on Geoscience and Remote Sensing*, vol. 57, no. 2, 2018, pp. 1049–1068.

[66] M. Kurum, M. M. Farhad, and D. Boyd, "GNSS TRANSMISSOMETRY (GNSS-T): MODELING PROPAGATION OF GNSS SIGNALS THROUGH FOREST CANOPY," *IGARSS 2022-2022 IEEE International Geoscience and Remote Sensing Symposium*. IEEE, 2022, pp. 4695–4698.

[67] M. Kurum, R. H. Lang, P. E. O'Neill, A. T. Joseph, M. Cosh, and T. Jackson, "Forest canopy effects on the estimation of soil moisture at L-band," *Int. Geosci. Remote Sens. Symp.*, vol. 1, no. 1, 2008, pp. I–33–I–36.

[68] R. H. Lang and J. S. Sighu, "Electromagnetic backscattering from a layer of vegetation: A discrete approach," *IEEE Transactions on Geoscience and Remote Sensing*, , no. 1, 1983, pp. 62–71.

[69] M. Lavalle, M. Morris, R. Shah, C. Zuffada, S. V. Nghiem, C. Chew, and V. U. Zavorotny, "Bistatic scattering modeling for dynamic mapping of tropical wetlands with CYGNSS," *IGARSS 2018-2018 IEEE International Geoscience and Remote Sensing Symposium*. IEEE, 2018, pp. 239–242.

[70] F. Lei, V. Senyurek, M. Kurum, A. C. Gurbuz, D. Boyd, R. Moorhead, W. T. Crow, and O. Eroglu, "Quasi-global machine learning-based soil moisture estimates at high spatio-temporal scales using CYGNSS and SMAP observations," *Remote Sensing of Environment*, vol. 276, 2022, p. 113041.

[71] D. LeVine, R. Meneghini, R. Lang, and S. Seker, "Scattering from arbitrarily oriented dielectric disks in the physical optics regime," *JOSA*, vol. 73, no. 10, 1983, pp. 1255–1262.

[72] M. Martín-Neira, S. D'Addio, C. Buck, N. Floury, and R. Prieto-Cerdeira, "The PARIS ocean altimeter in-orbit demonstrator," *IEEE Trans. Geosci. Remote Sens.*, vol. 49, no. 6 PART 2, 2011, pp. 2209–2237.

[73] D. Masters, T. M. Duly, S. Esterhuizen, V. G. Irisov, P. Jales, V. A. Nguyen, O. Nogués-Correig, L. Tan, T. Yuasa, and M. J. Angling, "Status and accomplishments of the Spire Earth observing nanosatellite constellation," 2020.

[74] A. Melebari, J. D. Campbell, E. Hodges, and M. Moghaddam, "Improved Geometric Optics with Topography (IGOT) Model for GNSS-R Delay-Doppler Maps Using Three-Scale Surface Roughness," *Remote Sensing*, vol. 15, no. 7, 2023, p. 1880.

[75] A. Mialon, P. Richaume, D. Leroux, S. Bircher, A. A. Bitar, T. Pellarin, J. P. Wigneron, and Y. H. Kerr, "Comparison of Dobson and Mironov dielectric models in the SMOS soil moisture retrieval algorithm," *IEEE Trans. Geosci. Remote Sens.*, vol. 53, no. 6, 2015, pp. 3084–3094.

[76] J. Miller, J. Wehle, A. Gerace, M. Montanar, and R. Kremens, "Low Cost UAS Radiometer for Landsat Land Surface Temperature Verification," *2019 IEEE Systems and Technologies for Remote Sensing Applications Through Unmanned Aerial Systems (STRATUS)*. feb 2019, pp. 1–4, IEEE.

[77] V. L. Mironov, R. D. De Roo, and I. V. Savin, "Temperature-dependable microwave dielectric model for an arctic soil," *IEEE Trans. Geosci. Remote Sens.*, vol. 48, no. 6, 2010, pp. 2544–2556.

[78] V. L. Mironov and S. V. Fomin, "Temperature and Mineralogy Dependable Model for Microwave Dielectric Spectra of Moist Soils," *PIERS Online*, vol. 5, no. 5, 2009, pp. 411–415.

[79] J. Mouginot, A. Pommerol, P. Beck, W. Kofman, and S. M. Clifford, "Dielectric map of the Martian northern hemisphere and the nature of plain filling materials," *Geophysical Research Letters*, vol. 39, no. 2, 2012, pp. 1–5.

[80] B. Nava, P. Coisson, and S. Radicella, "A new version of the NeQuick ionosphere electron density model," *Journal of atmospheric and solar-terrestrial physics*, vol. 70, no. 15, 2008, pp. 1856–1862.

[81] S. V. Nghiem, C. Zuffada, R. Shah, C. Chew, S. T. Lowe, A. J. Mannucci, E. Cardellach, G. R. Brakenridge, G. Geller, and A. Rosenqvist, "Wetland monitoring with global navigation satellite system reflectometry," *Earth and Space Science*, vol. 4, no. 1, 2017, pp. 16–39.

[82] J. F. Nouvel, A. Herique, W. Kofman, and A. Safaeinili, "Radar signal simulation: Surface modeling with the Facet Method," *Radio Science*, vol. 39, no. 1, 2004, pp. 162–177.

[83] A. O'Brien, "End-to-End Simulator Technical Memo," 2014.

[84] J. D. Oetting and T. Jen, "The Mobile User Objective System," vol. 30, no. 2, 2012, pp. 103–112.

[85] Y. Oh, "Radar measurement of soil moisture: From professor Fawwaz Ulaby's pioneering works in the early 1970s to its current status," *Int. Geosci. Remote Sens. Symp.*, 2012, pp. 1258–1261.

[86] S. Orfanidis, *Waves and Antennas Electromagnetic*, 2 edition, New Jersey, 2016.

[87] H. Park, A. Camps, J. Castellvi, and J. Muro, "Generic performance simulator of spaceborne GNSS-reflectometer for land applications," *IEEE Journal of Selected Topics in Applied Earth Observations and Remote Sensing*, vol. 13, 2020, pp. 3179–3191.

[88] H. Park, A. Camps, J. Castellvi, and J. Muro, "Generic Performance Simulator of Spaceborne GNSS-Reflectometer for Land Applications," *IEEE J. Sel. Top. Appl. Earth Obs. Remote Sens.*, vol. 13, 2020, pp. 3179–3191.

[89] J.-F. Pekel, A. Cottam, N. Gorelick, and A. S. Belward, "High-resolution mapping of global surface water and its long-term changes," *Nature*, vol. 540, no. 7633, 2016, pp. 418–422.

[90] N. R. Peplinski, F. T. Ulaby, and M. C. Dobson, "Dielectric properties of soils in the 0.3-1.3-GHz range," *IEEE Trans. Geosci. Remote Sens.*, vol. 33, no. 6, 1995, p. 1340.

[91] N. R. Peplinski, F. T. Ulaby, and M. C. Dobson, "Dielectric properties of soils in the 0.3-1.3-GHz range," *IEEE transactions on Geoscience and Remote sensing*, vol. 33, no. 3, 1995, pp. 803–807.

[92] K. Perlin, "Improving noise," *Proceedings of the 29th annual conference on Computer graphics and interactive techniques*, 2002, pp. 681–682.

[93] G. Picard, M. Sandells, and H. Löwe, "SMRT: An active–passive microwave radiative transfer model for snow with multiple microstructure and scattering formulations (v1. 0)," *Geoscientific Model Development*, vol. 11, no. 7, 2018, pp. 2763–2788.

[94] N. Pierdicca, L. Guerriero, A. Egido, S. Paloscia, and N. Floury, "Exploiting GNSS signals for soil moisture and vegetation biomass retrieval," *Int. Geosci. Remote Sens. Symp.* 2015, pp. 5119–5122, IEEE.

[95] N. Pierdicca, L. Guerriero, R. Giusto, M. Brogioni, and A. Egido, "SAVERS: A simulator of GNSS reflections from bare and vegetated soils," *IEEE Trans. Geosci. Remote Sens.*, vol. 52, no. 10, 2014, pp. 6542–6554.

[96] N. Pierdicca, L. Pulvirenti, F. Ticconi, and M. Brogioni, "Radar bistatic configurations for soil moisture retrieval: A simulation study," *IEEE Trans. Geosci. Remote Sens.*, vol. 46, no. 10, 2008, pp. 3252–3264.

[97] L. Poggio, L. M. De Sousa, N. H. Batjes, G. Heuvelink, B. Kempen, E. Ribeiro, and D. Rossiter, “SoilGrids 2.0: producing soil information for the globe with quantified spatial uncertainty,” *Soil*, vol. 7, no. 1, 2021, pp. 217–240.

[98] K. S. Rao, G. Chandra, and P. V. Narasimha Rao, “Study on penetration depth and its dependence on frequency, soil moisture, texture and temperature in the context of microwave remote sensing,” *Journal of the Indian Society of Remote Sensing*, vol. 16, no. 2, 1988, pp. 7–19.

[99] R. H. Reichle, J. V. Ardizzone, G.-K. Kim, R. A. Lucchesi, E. B. Smith, and B. H. Weiss, “Soil Moisture Active Passive (SMAP) mission level 4 surface and root zone soil moisture (L4_SM) product specification document,” 2022.

[100] B. Ren, J. Zhu, L. Tsang, and H. Xu, “Analytical Kirchhoff solutions (AKS) and numerical Kirchhoff approach (NKA) for first-principle calculations of coherent waves and incoherent waves at P band and L band in signals of opportunity (SoOP),” *Progress In Electromagnetics Research*, vol. 171, 2021, pp. 35–73.

[101] M. A. Ribot, C. Botteron, and P. A. Farine, “Derivation of the Cramér-Rao bound in the GNSS-reflectometry context for static, ground-based receivers in scenarios with coherent reflection,” *Sensors (Switzerland)*, vol. 16, no. 12, 2016, pp. 18–25.

[102] C. S. Ruf, S. Gleason, Z. Jelenak, S. Katzberg, A. Ridley, R. Rose, J. Scherrer, and V. Zavorotny, “The CYGNSS nanosatellite constellation hurricane mission,” *Int. Geosci. Remote Sens. Symp.*, , no. July, 2012, pp. 214–216.

[103] M. Sadeghi, A. Tabatabaeenejad, M. Tuller, M. Moghaddam, and S. B. Jones, “Advancing NASA’s AirMOSS P-band Radar Root-zone Soil Moisture Retrieval Algorithm via Incorporation of Richards’ Equation,” *Remote Sens.*, vol. 9, no. 1, 2017.

[104] S. Seker and A. Schneider, “Electromagnetic scattering from a dielectric cylinder of finite length,” *IEEE Transactions on Antennas and Propagation*, vol. 36, no. 2, 1988, pp. 303–307.

[105] V. Senyurek, F. Lei, D. Boyd, M. Kurum, A. C. Gurbuz, and R. Moorhead, “Machine Learning-Based CYGNSS Soil Moisture Estimates over ISMN sites in CONUS,” *Remote Sensing*, vol. 12, no. 7, 2020, p. 1168.

[106] R. Shah, X. Xu, S. Yueh, C. S. Chae, K. Elder, B. Starr, and Y. Kim, “Remote sensing of snow water equivalent using P-band coherent reflection,” *IEEE Geoscience and Remote Sensing Letters*, vol. 14, no. 3, 2017, pp. 309–313.

[107] S. Silver, *Microwave antenna theory and design*, Number 19. Iet, 1984.

[108] W. M. Steedly and R. L. Moses, “The Cramer-Rao Bound for pole and amplitude coefficient estimates of damped exponential signals in noise,” *IEEE Trans. Signal Process.*, vol. 41, no. 3, 1993, pp. 1305–1318.

[109] A. Tabatabaeenejad, M. Burgin, X. Duan, and M. Moghaddam, "P-band radar retrieval of subsurface soil moisture profile as a second-order polynomial: First AirMOSS results," *IEEE Trans. Geosci. Remote Sens.*, vol. 53, no. 2, 2015, pp. 645–658.

[110] A. Tabatabaeenejad, X. Duan, and M. Moghaddam, "Coherent scattering of electromagnetic waves from two-layer rough surfaces within the kirchhoff regime," *IEEE Trans. Geosci. Remote Sens.*, vol. 51, no. 7, 2013, pp. 3943–3953.

[111] D. R. Thompson, T. M. Elfouhaily, and J. L. Garrison, "An improved geometrical optics model for bistatic GPS scattering from the ocean surface," *IEEE Transactions on Geoscience and Remote Sensing*, vol. 43, no. 12, 2005, pp. 2810–2821.

[112] I. Tolstoy and C. Clay, "Ocean acoustics: An evaluation," *Reviews of Geophysics*, vol. 4, no. 1, 1966, pp. 33–40.

[113] L. Tsang and J. A. Kong, *Scattering of electromagnetic waves: advanced topics*, John Wiley & Sons, 2004.

[114] L. Tsang, T.-H. Liao, R. Gao, H. Xu, W. Gu, and J. Zhu, "Theory of microwave remote sensing of vegetation effects, soop and rough soil surface backscattering," *Remote Sensing*, vol. 14, no. 15, 2022, p. 3640.

[115] J. Tye, P. Jales, M. Unwin, and C. Underwood, "The first application of stare processing to retrieve mean square slope using the SGR-ReSI GNSS-R experiment on TDS-1," *IEEE J. Sel. Top. Appl. Earth Obs. Remote Sens.*, vol. 9, no. 10, 2016, pp. 4669–4677.

[116] F. Ulaby, R. Moore, and A. Fung, *Microwave Remote Sensing: Microwave remote sensing fundamentals and radiometry*, Artech House remote sensing library. Artech House, 1981.

[117] F. Ulaby, R. Moore, and A. Fung, "Microwave remote sensing: Active and passive. Volume 2-Radar remote sensing and surface scattering and emission theory," 1982.

[118] F. T. Ulaby, "Radar Measurement of Soil Moisture Content," *IEEE Trans. Antennas Propag.*, vol. 11, no. 2, 1974, pp. 257–265.

[119] F. T. Ulaby and D. G. Long, *Microwave Radar and Radiometric Remote Sensing*, 1st edition, University of Michigan Press, Ann Arbor, 2014.

[120] M. J. Unwin, N. Pierdicca, E. Cardellach, K. Rautiainen, G. Foti, P. Blunt, L. Guerriero, E. Santi, and M. Tossaint, "An introduction to the HydroGNSS GNSS reflectometry remote sensing mission," *IEEE Journal of Selected Topics in Applied Earth Observations and Remote Sensing*, vol. 14, 2021, pp. 6987–6999.

[121] J. R. Wang and T. J. Schmugge, "An empirical model for the complex dielectric permittivity of soils as a function of water content," *IEEE Trans. Geosci. Remote Sens.*, vol. GE-18, no. 4, 1980, pp. 288–295.

[122] W. Wasylkiwskyj, "Response of an antenna to arbitrary incident fields," *2005 IEEE Antennas and Propagation Society International Symposium*. IEEE, 2005, vol. 3, pp. 39–42.

[123] T.-D. Wu, K.-S. Chen, J. Shi, H.-W. Lee, and A. K. Fung, "A study of an AIEM model for bistatic scattering from randomly rough surfaces," *IEEE Transactions on Geoscience and Remote Sensing*, vol. 46, no. 9, 2008, pp. 2584–2598.

[124] X. Wu, A. Calabia, J. Xu, W. Bai, and P. Guo, "Forest canopy scattering properties with signal of opportunity reflectometry: theoretical simulations," *Geoscience Letters*, vol. 8, 2021, pp. 1–15.

[125] H. Xu, J. Zhu, L. Tsang, and S. B. Kim, "A fine scale partially coherent patch model including topographical effects for gnss-r ddm simulations," *Progress in Electromagnetics Research*, vol. 170, no. February, 2021, pp. 97–128.

[126] H. Xu, J. Zhu, L. Tsang, and S. B. Kim, "A Fine Scale Partially Coherent Patch Model including Topographical Effects for GNSS-R DDM Simulations.," *Progress in electromagnetics research*, vol. 170, 2021.

[127] Z. Xu and K.-S. Chen, "Numerical Study of the Spatiotemporally-Varying Background Ionospheric Effects on P-Band Satellite SAR Imaging," *IEEE Access*, vol. 8, 2020, pp. 123182–123199.

[128] Q. Yan, W. Huang, S. Jin, and Y. Jia, "Pan-tropical soil moisture mapping based on a three-layer model from CYGNSS GNSS-R data," *Remote Sensing of Environment*, vol. 247, 2020, p. 111944.

[129] S. Yayong, M. Jianwei, P. Jie, H. Shifeng, Y. Kun, Z. Peng, and Z. He, "Preliminary Applicability Analysis of Soil Dielectric Constant Model of the Different Soil Texture Condition," *Int. Geosci. Remote Sens. Symp.*, 2019, pp. 7148–7151.

[130] S. Yueh, R. Shah, X. Xu, K. Elder, and B. Starr, "Experimental Demonstration of Soil Moisture Remote Sensing Using P-Band Satellite Signals of Opportunity," *IEEE Geosci. Remote Sens. Lett.*, 2019, pp. 1–5.

[131] S. H. Yueh, R. Shah, X. Xu, B. Stiles, and X. Bosch-Lluis, "A satellite synthetic aperture radar concept using P-band signals of opportunity," *IEEE Journal of Selected Topics in Applied Earth Observations and Remote Sensing*, vol. 14, 2021, pp. 2796–2816.

[132] S. H. Yueh, X. Xu, R. Shah, S. Margulis, and K. Elder, "P-Band signals of opportunity for remote sensing of root zone soil moisture," *IGARSS 2018 - 2018 IEEE Int. Geosci. Remote Sens. Symp.* Jul 2018, pp. 1403–1406, IEEE.

[133] V. U. Zavorotny, S. Gleason, E. Cardellach, and A. Camps, "Tutorial on remote sensing using GNSS bistatic radar of opportunity," *Geosci. Remote Sens. Mag. IEEE*, vol. 2, no. 4, 2014, pp. 8–45.

[134] V. U. Zavorotny and A. G. Voronovich, "Scattering of GPS signals from the ocean with wind remote sensing application," *IEEE Transactions on Geoscience and Remote Sensing*, vol. 38, no. 2 II, 2000, pp. 951–964.

[135] V. U. Zavorotny and A. G. Voronovich, "Scattering of GPS signals from the ocean with wind remote sensing application," *IEEE Transactions on Geoscience and Remote Sensing*, vol. 38, no. 2, 2000, pp. 951–964.

[136] V. U. Zavorotny and A. G. Voronovich, "Scattering of GPS signals from the ocean with wind remote sensing application," *IEEE Trans. Geosci. Remote. Sens.*, vol. 38, 2000, pp. 951–964.

[137] M. Zribi, A. Gorrab, N. Baghdadi, Z. Lili-Chabaane, and B. Mougenot, "Influence of radar frequency on the relationship between bare surface soil moisture vertical profile and radar backscatter," *IEEE Geosci. Remote Sens. Lett.*, vol. 11, no. 4, 2014, pp. 848–852.

[138] M. Zribi, M. Sahnoun, R. Dusséaux, S. Afifi, N. Baghdadi, and A. Ben Hamida, "Analysis of P band radar signal potential to retrieve soil moisture profile," *2nd International Conference on Advanced Technologies for Signal and Image Processing, ATSIP 2016*, vol. 1, no. 4, 2016, pp. 591–595.

APPENDIX A

SUPPLEMENTARY INFORMATION FOR THE NESTED FACET METHOD FORMULATION

A.1 Conversion of Electric Field to Scattering Matrix

The solution to facet-method-based KA (FM-KA) can be cast into a scattering matrix. We will follow the convention of [119, eq 5.12] with the exception that all modifications to the field caused by free-space travel are placed in the constant $\mathcal{K}_{k_a}$. This is done in order to pair with the notation of [65]. In other words, we will assume

$$\begin{bmatrix} E^o_{\mathrm{v}} \\ E^o_{\mathrm{h}} \end{bmatrix} = \mathcal{K}_{k_a} \underline{\underline{S}} \begin{bmatrix} E^i_{\mathrm{v}} \\ E^i_{\mathrm{h}} \end{bmatrix} \tag{A.1}$$

where E^i_{v} and E^i_{h} form a unitary Jones vector to be scaled by the amplitude and phase values of $\mathcal{K}_{k_a}$.

Let us take the general solution of equation 4.16 while making the modification that the component describing the amplitude and phase of the surface is taken out of the equation. That is to say, let us create a constant C

$$C_{k_a,q} = \mathbf{E}_{k_a,q} / \mathcal{K}_{k_a} \tag{A.2}$$

We can express the scattering matrix then as

$$\underline{\underline{S}}_{\,k_a} = \begin{bmatrix} \hat{\mathbf{v}}_{k_a,o} \cdot \mathbf{C}_{k_a,\mathrm{v}} & \hat{\mathbf{v}}_{k_a,o} \cdot \mathbf{C}_{k_a,\mathrm{h}} \\ \hat{\mathbf{h}}_{k_a,o} \cdot \mathbf{C}_{k_a,\mathrm{v}} & \hat{\mathbf{h}}_{k_a,o} \cdot \mathbf{C}_{k_a,\mathrm{h}} \end{bmatrix} \tag{A.3}$$

which can be rewritten as

$$\underline{\underline{S}}_{\,k_a} = \begin{bmatrix} S_{\mathrm{vv}} & S_{\mathrm{vh}} \\ S_{\mathrm{hv}} & S_{\mathrm{hh}} \end{bmatrix} \tag{A.4}$$

and allowing us to create the form of equation A.1

$$\begin{bmatrix} E_{\mathrm{v}}^{o} \\ E_{\mathrm{h}}^{o} \end{bmatrix} = \mathcal{K}_{k_a} \underline{\underline{S}}_{k_a} \begin{bmatrix} E_{\mathrm{v}}^{i} \\ E_{\mathrm{h}}^{i} \end{bmatrix}$$

Thus placing the FM-KA in a form that is usable in network-scattering-parameter-based formulations as seen in [65]. To allow for the facet nesting in equation 4.23, the phase factor of equation 4.22 can be included in the formulation of $C_{k_a,q}$ assuming proper definitions of the ranges with respect to any facet nesting. Finally, we can express the normalized bistatic radar cross-section (NBRCS) as

$$\sigma_0^{pq} = \frac{4\pi}{A} \left| S_{pq} \right|^2 \tag{A.5}$$

where A represents the area of the scatterer or another normalizing reference area. All simulations used in this paper use the area given by equation 4.14.